

**Quantum Limited Optical Phase Detection
in a High Power Suspended Interferometer**

by

Brian Thomas Lantz

Submitted to the Department of Physics in partial
fulfillment of the requirements for the degree of

Doctor of Philosophy

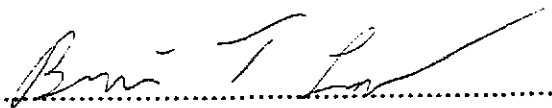
at the

MASSACHUSETTS INSTITUTE OF TECHNOLOGY

February, 1999

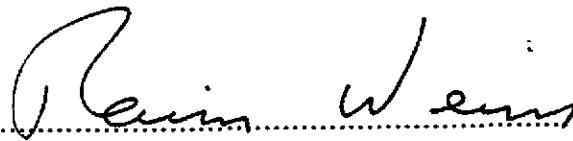
© Massachusetts Institute of Technology, 1999. All Rights Reserved.

Author



Department of Physics
February, 1999

Certified by



Rainer Weiss
Department of Physics
Thesis Supervisor

Accepted by

Thomas J. Greytak
Professor, Associate Department Head for Education
Department of Physics

Quantum Limited Optical Phase Detection in a High Power Suspended Interferometer

by

Brian Lantz

Submitted to the Department of Physics in February 1999,
in partial fulfillment of the requirements for the degree of
Doctor of Philosophy

Abstract

The LIGO project (Laser Interferometer Gravitational-Wave Observatory) is currently engaged in the construction of a new observatory to measure gravitational radiation from astrophysical sources. The first generation of interferometric gravitational wave antennas is scheduled to come on-line in 2001. With an initial noise level of 3×10^{-23} strain/ $\sqrt{\text{Hz}}$ at frequencies around 200Hz, these antennas represent the most sensitive instruments ever constructed for the detection of gravitational radiation. To achieve the required sensitivity, the antennas are configured as recycled Michelson Interferometers with Fabry-Perot cavities in the Michelson arms.

One of the fundamental limits associated with an instrument of this type is the ability to detect differential phase shifts between the beams returning to the beamsplitter from the Fabry-Perot arm cavities. To achieve the planned sensitivity to gravitational radiation, this detection should be limited only by photon counting statistics ("shot noise") at a level of 8×10^{-11} radians/ $\sqrt{\text{Hz}}$ between 150Hz and 10kHz.

The goal of this work is to develop and demonstrate the techniques which are necessary to achieve this optical phase sensitivity. A prototype recycled Michelson interferometer was constructed which reached an optical phase sensitivity of 12×10^{-11} radians/ $\sqrt{\text{Hz}}$ above 600 Hz.

This thesis describes the methods used to achieve this optical phase sensitivity, and details the lessons learned from operating the prototype instrument. We pay particular attention to interferometric control of suspended optics, laser frequency control, and thermal lensing.

Thesis Supervisor: Rainer Weiss
Title: Professor of Physics

Acknowledgments

To Rai, who talked with me one Saturday morning and set me off in a new direction.

To Peter Fritschel, whose quiet brilliance made this experiment possible.

To Gaby, who must be the best lab partner one could hope for.

To Partha and Haisheng, who worked tirelessly to make this project a success.

To Nergis and Daniel, for a damn fine wavefront sensor which worked on the first day!

To Jim, Rich, and Rick, who gave us the Prestabilized Laser. Either it ran like a champ, or Rich would fly to Boston and fix it.

To the LIGO team, for the technical support, guidance, and friendship which made this experiment a success. You will change the world, good luck!

To Jen, the love of my life and the light of my heart, my constant companion, even when I was writing my thesis.

“In the first experiment one of the principal difficulties encountered . . . was its extreme sensitiveness to vibration. This was so great that it was impossible to see the interference fringes except at brief intervals when working in the city, even at two o’clock in the morning.”

-Albert Michelson, [Michelson 1887]

(Describing the first interferometer he used to attempt to detect the luminiferous ether.)

Table of Contents

| | <u>page</u> |
|--|-------------|
| List of Figures | 11 |
| Chapter 1: Importance of Optical Phase Sensitivity to Interferometric Gravitational Wave Antennas | 13 |
| 1.1: Introduction | 13 |
| 1.2: Gravitational Waves | 13 |
| 1.3: Sources of Gravitational Waves | 15 |
| 1.4: The LIGO detector | 17 |
| Chapter 2: Interferometer Configuration and Sensitivity Limits | 21 |
| 2.1: Michelson Interferometer Sensitivity and Schnupp Modulation | 21 |
| 2.2: Power Recycling Cavity | 26 |
| 2.3: Useful Expressions | 30 |
| 2.4: Noise | 31 |
| 2.5: Sensitivity limit for modulation readout scheme with optical losses | 35 |
| Chapter 3: Description of the Experiment | 39 |
| 3.1: Configuration of the Interferometer | 39 |
| 3.2: The Differential Mode and the Detection of Optical Phase | 40 |
| 3.3: The Common Mode and the Importance of Frequency Noise | 43 |
| 3.3.1: Coupling of Frequency Noise into Phase Noise | 43 |
| 3.3.2: The Prestabilized Laser | 43 |
| 3.3.3: Cavity Common Mode Control, the Second Stage of Frequency Control .. | 46 |
| 3.4: Wavefront Sensing and Control of the Suspended Interferometer | 52 |
| 3.5: Environmental Isolation of the Interferometer Optics | 55 |
| 3.5.1: Interferometer Optics | 56 |
| 3.5.2: Parasitic Interferometry | 61 |
| Chapter 4: Thermal Lensing of the Beamsplitter | 69 |
| 4.1: Measuring the Thermal Distortions | 69 |
| 4.2: Modeling of the Thermal Lens | 72 |
| 4.2.1: Thermal Lens parameters | 72 |
| 4.2.2: Propagation Model | 75 |
| Chapter 5: Phase Sensitivity and Phase Noise | 83 |
| 5.1: Measurement of the Optical Phase Sensitivity | 83 |
| 5.2: Result of the Measurement | 83 |
| 5.2.1: Shot Noise Limited Regime | 84 |
| 5.3: Spectral Features | 87 |
| 5.3.1: Thermal Motion of Magnetic Actuator Fins | 88 |
| 5.3.2: Calibration peak at 2kHz | 89 |
| 5.3.3: Motion of Optics on Input Table | 89 |
| 5.3.4: Violin Modes of Suspension Wires | 90 |
| 5.3.5: Power Line Noise | 90 |
| 5.4: Low Frequency Noise | 90 |
| 5.4.1: Electronic Noise | 90 |
| 5.4.2: Thermal Noise | 93 |

| | |
|---|-----|
| 5.4.3: Beam Jitter | 97 |
| 5.4.4: Input Power Fluctuations | 105 |
| Chapter 6: Conclusions | 109 |
| 6.1: Improvements in Optical Phase Measurements | 109 |
| 6.2: Improvements from the Spectrum of the Argon Laser Experiment | 111 |
| 6.3: Limiting Noise for this Experiment | 111 |
| 6.4: Concluding Remarks | 115 |
| References | 117 |

List of Figures

| | <u>page</u> |
|---|-------------|
| Figure 1.1: The effect of a passing gravitational wave on an object. | 15 |
| Figure 1.2: Basic optical configuration of LIGO. | 18 |
| Figure 1.3: LIGO noise curve. | 20 |
| Figure 2.1: Schematic view of recycled Michelson interferometer with frontal modulation. | 21 |
| Figure 2.2: Schematic view of an asymmetric Michelson interferometer. | 22 |
| Figure 2.3: Fields within a Fabry-Perot cavity | 26 |
| Figure 2.4: Field Eigenstates described by equations 2.40 through 2.42. | 32 |
| Figure 2.5: Plot of $(N_2 \pm \Delta N_2) / N$ vs. differential phase for $N=400$ | 34 |
| Figure 3.1: Optical Configuration of the Phase Noise Interferometer. | 39 |
| Figure 3.2: Overview of the experimental layout. | 41 |
| Figure 3.3: Open loop gain of differential Michelson interferometer control loop. | 42 |
| Figure 3.4: Schematic drawing of the Prestabilized Laser. | 44 |
| Figure 3.5: Open loop gain of the Prestabilized Laser | 45 |
| Figure 3.6: Frequency noise of the Prestabilized Laser | 46 |
| Figure 3.7: Common mode servo control. | 47 |
| Figure 3.8: Servo paths for common mode servo. | 49 |
| Figure 3.9: Open loop gain of the second stage of frequency control. | 50 |
| Figure 3.10: Suppression of frequency noise by the common mode loop. | 51 |
| Figure 3.11: Frequency noise of laser light in the power recycling cavity. | 52 |
| Figure 3.12: Alignment of quadrant diode for wavefront sensor measurement. | 53 |
| Figure 3.13: Open loop gain of the differential angular alignment servo. | 54 |
| Figure 3.14: Detail of unity gain point for alignment control servo. | 55 |
| Figure 3.15: Environmental isolation of the experiment. | 56 |
| Figure 3.16: Closed loop gain for one foot of the Stacis™ system supporting the Michelson optics. | 57 |
| Figure 3.17: Seismic isolation stack. | 58 |
| Figure 3.18: Optic suspended by a single loop of wire. | 59 |
| Figure 3.19: OSEM detail. | 60 |
| Figure 3.20: Suspension wire attachment detail. | 61 |
| Figure 3.21: Electric fields of a parasitic interferometer. | 61 |
| Figure 3.22: Seismic isolation of the input optics table. | 63 |
| Figure 3.23: Horizontal motion of input optics table | 64 |
| Figure 3.24: Acoustic drive level at the output optics table, with and without anechoic enclosure. | 66 |
| Figure 4.1: Measured contrast loss of the beamsplitter as a function of incident power. | 71 |
| Figure 4.2: Schematic view of the heat flow from surface absorption of the beamsplitter. | 73 |

| | |
|---|-----|
| Figure 4.3: Thermal distortion of the beamsplitter for power absorbed at one surface. | 73 |
| Figure 4.4: Thermal distortion of the beamsplitter caused by bulk absorption. | 74 |
| Figure 4.5: Diagram listing the steps of the beam propagation model. | 75 |
| Figure 4.6: Measured contrast loss and predicted contrast loss with 47 ppm/cm bulk absorption. | 76 |
| Figure 4.7: Modeled intensity distribution of the dark fringe. | 77 |
| Figure 4.8: Image of dark port beam with 5 watts of circulating power in the interferometer. | 79 |
| Figure 4.9: Dark port image with 21 watts of circulating power. | 79 |
| Figure 4.10: Dark port Image with 36 watts of circulating power. | 80 |
| Figure 4.11: Dark port Image with 57 watts of circulating power. | 80 |
| Figure 4.12: Dark port image with 98 watts of circulating power. | 81 |
| Figure 5.1: Schematic view of Michelson interferometer readout and control configuration. | 83 |
| Figure 5.2: Spectrum of the Phase Noise Interferometer. | 84 |
| Figure 5.3: Cavity Loss (L) and Cavity Matching parameter (M) calculation. | 86 |
| Figure 5.4: Narrow spectral features. | 88 |
| Figure 5.5: Drawing of an interferometer optic, showing the magnet-fin assemblies. | 89 |
| Figure 5.6: Impact of coil driver noise on the spectrum. | 91 |
| Figure 5.7: Impact of Michelson controller noise on the spectrum. | 92 |
| Figure 5.8: Total electronic noise. | 92 |
| Figure 5.9: Detail of spectrum showing the 3 peaks associated with fin resonances. | 95 |
| Figure 5.10: Impact of Thermal Motion on Spectrum. | 96 |
| Figure 5.11: Detail of figure 5.10, showing impact of thermal motion of violin modes. | 97 |
| Figure 5.12: Optical lengths and misalignments in the Michelson interferometer. | 98 |
| Figure 5.13: Residual differential misalignment of the Michelson arm mirrors. | 100 |
| Figure 5.14: Angular motion of input beam measured on the input optics table. | 101 |
| Figure 5.15: Geometry of the recycling cavity. | 101 |
| Figure 5.16: Impact of misalignments on phase noise spectrum. | 103 |
| Figure 5.17: Relative fluctuations of the power in the recycling cavity. | 107 |
| Figure 5.18: Impact of power fluctuations on phase noise spectrum. | 107 |
| Figure 6.1: Evolution of optical phase measurements. | 109 |
| Figure 6.2: Comparison of the phase noise spectra with the LIGO requirement. | 110 |
| Figure 6.3: Major noise sources in the measurement. | 112 |
| Figure 6.4: Major noise sources at low frequencies. | 113 |
| Figure 6.5: The residual phase noise in this measurement. | 114 |

Chapter 1

Importance of Optical Phase Sensitivity to Interferometric Gravitational Wave Antennas

1.1 Introduction

The Laser Interferometer Gravitational-Wave Observatory (LIGO) is now engaged in construction of a new observatory which will be able to measure gravitational radiation from astrophysical sources [Abramovici '92]. Gravitational radiation was first predicted by Einstein [Einstein '16], [Einstein '18], but, due to the extremely small influence of this radiation, it has never been directly observed.¹ The goal of this chapter is to introduce the reader to effects of gravitational radiation, explain briefly the method which LIGO will use to detect this radiation, and motivate this work by describing the importance of optical phase sensitivity to the LIGO detection scheme.

1.2 Gravitational Waves

Gravitational waves are traveling waves of the space-time metric, $g_{\mu\nu}$. Generated by accelerating masses, these gravitational field disturbances propagate at the speed of light, and provide the solution to Newton's problem of gravitational action at a distance. A gravitational plane wave creates a differential strain along the 2 space axes which are transverse to the direction of the waves's propagation. For any reasonable source of gravitational radiation, the perturbations of the metric by the passing gravitational wave are quite small, so we use the "linearized" theory (see, for example, [Schutz '90] or [Saulson '94]) and rewrite the metric $g_{\mu\nu}$ as

$$g_{\mu\nu} \approx \eta_{\mu\nu} + h_{\mu\nu} \quad |h_{\mu\nu}| \ll 1 \quad (1.1)$$

where $\eta_{\mu\nu}$ is the Minkowski metric (describing flat space), and $h_{\mu\nu}$ is the metric distortion due to the gravitational wave. In the weak-field limit, the Einstein equation for $h_{\mu\nu}$ can be written as a traveling wave equation,

1. However, indirect observations have been made by Hulse & Taylor [Hulse '75], [Taylor '82], [Taylor '89], who carefully studied the orbital decay of a neutron star binary system, and found the decay rate to be in excellent agreement with the energy lost to gravitational radiation.

$$\left(-\frac{1}{c^2} \frac{\partial^2}{\partial t^2} + \nabla^2 \right) h_{\mu\nu} = 0. \quad (1.2)$$

In a transverse-traceless gauge, we can write the solution for a wave traveling in the \hat{z} direction as

$$h_{\mu\nu} = \exp(ik_\alpha x^\alpha) \begin{bmatrix} 0 & 0 & 0 & 0 \\ 0 & h_+ & h_x & 0 \\ 0 & h_x & -h_+ & 0 \\ 0 & 0 & 0 & 0 \end{bmatrix}. \quad (1.3)$$

This represents two independent plane-wave solutions. The magnitude of the spatial components along h_{xx} and h_{yy} is h_+ , which is known as the “plus” polarization, and the magnitude along h_{xy} and h_{yx} is h_x , which is commonly called the “cross” polarization. Eqn. 1.3 means that each of the four non-zero components of $h_{\mu\nu}$ could be expressed as

$$h_{xx} = h_+ \cdot \sin(-\omega t + kz) \quad (1.4)$$

representing a metric perturbation traveling along \hat{z} at the speed of light, with frequency ω , and amplitude h_+ .

One way to understand the implication of a passing gravitational wave is to examine the change in proper distance between two objects as a wave passes by. With one object at the origin, and the second at $x = l$, $y = z = 0$, then the proper distance between them is

$$D_{\text{proper}} = \int \left| g_{\mu\nu} dx^\mu dx^\nu \right|^{\frac{1}{2}}. \quad (1.5)$$

This reduces to

$$D_{\text{proper}} = \int_0^l \sqrt{|g_{xx}|} dx \quad (1.6)$$

If h_+ is spatially uniform, changing slowly², and less than 1, then the proper distance is:

$$\begin{aligned} D_{\text{proper}} &\approx l \cdot \sqrt{\eta_{xx} + h_{xx}(x=0, t=0)} \\ &\approx l \cdot \left[1 + \frac{1}{2} h_+(x=0, t=0) \right] \end{aligned} \quad (1.7)$$

2. The measurement in LIGO will be conducted by light which is resonant in a 4km arm cavity, so the time fluctuations of $h_{\mu\nu}$ should be compared with the cavity storage time of 0.88 msec.

which means the distance between the two “freely-falling” objects changes as a gravitational wave passes by. According to eqn. 1.3, $h_{xx} = -h_{yy}$, so as distances along the \hat{x} axis are elongated, distances along \hat{y} will be compressed by the same ratio. It is important to realize that the proper distance is stretched by an amount which is proportional to the original distance and the gravitational wave amplitude, which is why the effect of gravitational radiation is usually described as producing a strain, i.e.

$$\frac{\delta l}{l} = \frac{1}{2}h_+ \quad (1.8)$$

There are only two independent components of $h_{\mu\nu}$, which are described as the two polarizations of gravitational waves. The amplitude of a plane wave in the “plus” polarization is captured by h_+ , which will differentially change the proper distances along \hat{x} and \hat{y} . The “cross” polarization is described by h_x , and results in a differential stretching which is rotated by 45° from the \hat{x} and \hat{y} axes. This effect on a ring of free masses is shown in figure 1.1.

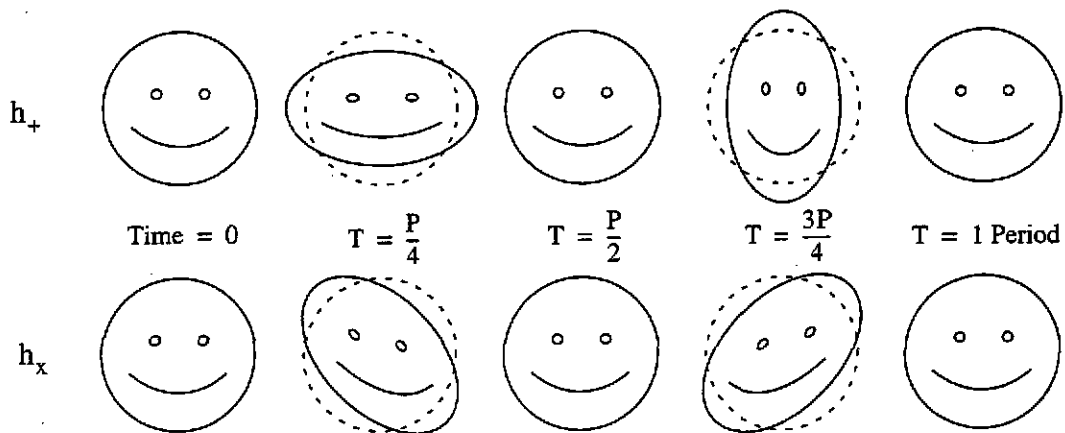


Figure 1.1: The effect of a passing gravitational wave on an object.

1.3 Sources of Gravitational Waves

The search for gravitational waves has so far been stymied by the fact that even the most powerful sources of gravitational radiation only produce tiny effects at the Earth. A typical source produces waves at the earth with a strain of $h \sim \frac{\ddot{Q}G}{Rc^4}$. Here, \ddot{Q} is the acceleration of the quadrupole moment of the source, G is the gravitational constant, R is the distance from the source, and c is the speed of light. The scaling factor, G/c^4 , is quite small, leading us to consider gravitational radiators on the order of a solar mass.

Many sources of gravitational waves are discussed as possible LIGO candidates, including coalescence of two compact objects (such as neutron stars or black holes), supernovas which generate non-spherical motion during the core collapse, and spinning neutron stars with non-axisymmetric mass distribution (see, for example, [Thorne '87]). The imminent completion of the LIGO interferometers and data from the new Rossi X-Ray Timing Explorer (RXTE) have generated a great deal of interest in variants to these standard sources, including new estimates of the number of neutron star-black hole binaries by Bethe and Brown [Bethe '98] and work by Lars Bildsten and others discussing various mechanisms by which neutron stars could convert the energy and angular momentum gained by accretion into gravitational radiation [Andersson '98], [Bildsten '98], [Owen '98].

The fiducial source of radiation for which one designs detectors is the burst of gravitational waves produced in the final minutes before the coalescence of inspiralling binary neutron stars. If two neutron stars of equal mass M are orbiting in the x - y plane at a distance $2r_0$ from each other with an orbital frequency of f_{orb} , then the amplitude of waves traveling along the \hat{z} axis is [Saulson '94]

$$h_{xx} = \frac{32\pi^2 G}{Rc^4} M r_0^2 f_{\text{orb}}^2 \cos(2 \cdot 2\pi f_{\text{orb}} t), \quad (1.9)$$

$$h_{xy} = -h_{xx}.$$

Newtonian mechanics suggests we can relate the radius and frequency by $f_{\text{orb}}^2 = GM/16\pi^2 r_0^3$, and the strain becomes

$$h_{xx} = \frac{2G^2 M^2}{Rc^4 r_0} = 1.1 \times 10^{-21} \left(\frac{M}{1.4M_\odot} \right)^2 \left(\frac{15 \text{ Mpc}}{R} \right) \left(\frac{f_{\text{orb}}}{400 \text{ Hz}} \right)^{\frac{2}{3}}. \quad (1.10)$$

This represents the strain produced by a pair of neutron stars ($M = 1.4M_\odot$) in the Virgo cluster ($R = 15 \text{ Mpc}$) in the last minute of their lives (when $f_{\text{orb}} \sim 400 \text{ Hz}$!). It is this level of strain which LIGO hopes to detect. Unfortunately, current estimates of the population of neutron star binaries indicate that we will need to observe an astrophysical volume which extends 200 Mpc from Earth to measure three such coalescence events each year ([Phinney '91] and [Narayan '91]).

Another burst source is the core collapse of a type II supernova. Several models of core collapse are described in [Thorne '87]. The current belief is that the core collapse will be only slightly aspheric. If bar ($m=2$) modes form in the spinning, collapsing core, they would emit gravitational radiation. These events might last about 30 cycles at 1000Hz, and could emit gravitational energy $\Delta E_{\text{GW}} \sim 3 \times 10^{-4} M_{\odot} c^2$. At a distance of 10Mpc, within which volume there are typically several type II supernovas each year, a core collapse which develops a bar instability could generate a characteristic strain at the Earth of $h_c \sim 5 \times 10^{-22}$.

There are several models for periodic sources, sources whose gravitational radiation signature changes very slowly with time. Many of these sources, like the Hulse-Taylor binary pair of neutron stars PSR1916+13, emit radiation at a frequency much to low to be seen with currently imagined Earth-bound instruments³. Some periodic sources have been suggested, however, which would be within the observational capabilities of the LIGO detectors. [Bildsten '98] has suggested, for example, that the accreting neutron star in Scorpius X-1 could be emitting gravitational waves at 500Hz, twice the neutron star rotation frequency. The amplitude could be as large as $h_c \approx 2.2 \times 10^{-26}$, which means it should be observable with a year or so of integrated observation time.

1.4 The LIGO detector

To detect a strain of the order 10^{-21} will be difficult, but several groups around the world are currently building observatories to meet that challenge. LIGO is building a pair of 4km baseline optical interferometers, one in Hanford, Washington, and one in Livingston Parish, Louisiana [Barish '97]. LIGO is also building a half length (2 km) interferometer in the vacuum system at the Hanford site. Virgo, an Italian-French collaboration, is building a 3km instrument near Pisa, Italy [Vinet '97]. GEO600 is a German-U.K. collaboration building an advanced 600 meter instrument in Hanover, Germany [Danzmann '97]. There is also active work ongoing at the TAMA project in Japan [Tsubono '97] and the ACIGA project in Australia [Blair '97].

Each of the LIGO instruments is configured as a power-recycled Michelson interferometer with Fabry-Perot arm cavities, as shown in figure 1.2. The Michelson interferome-

3. However, LISA, the proposed Laser Interferometer Space Antenna, could readily observe many low frequency sources within our galaxy [Folkner '98].

ter is well suited for the detection of gravitational waves, because it is sensitive to differential arm length changes.

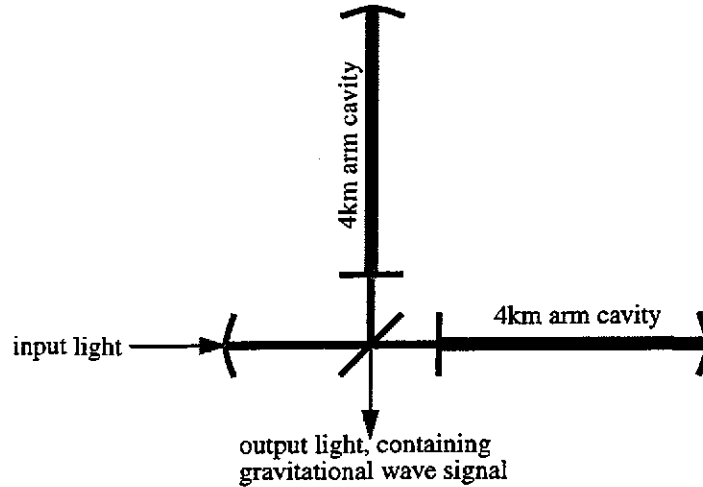


Figure 1.2: Basic optical configuration of LIGO.

This figure shows the recycling mirror, the beamsplitter, and the Fabry-Perot arm cavities. The line thickness indicates that there is more power circulating in the arm cavities than is circulating at the beamsplitter, and that there is more power at the beamsplitter than in the input beam.

If the mirrors are configured as free masses⁴ and the wave is incident on the interferometer from the correct direction, then the perpendicular arms will experience a differential strain as the space is distorted as shown in figure 1.1. In the direction of maximum sensitivity, for a wave polarized in the “plus” direction, one arm will see a strain of $+\frac{1}{2}h_+$ and the other arm will see a strain of $-\frac{1}{2}h_+$, so the differential strain $h = h_+$. As the wave passes through the interferometer, alternately expanding and compressing the arms, the differential phase shift of the two beams returning to the beamsplitter from the arms will oscillate at the gravitational wave frequency.

In effect, the interferometer arms are a transducer which converts gravitational wave strain into differential optical phase shifts. Since the waves are of low amplitude, the LIGO transducer must be extremely sensitive. The challenges to building a good detector fall into three broad areas:

1. Build a transducer which effectively converts gravitational wave strain into optical phase shift.
 2. Make the differential optical phase insensitive to other sources of noise.
 3. Make a very sensitive detection of the resulting differential optical phase.
-
4. The LIGO masses are suspended as pendula with a 1Hz fundamental frequency, which means they are essentially free in the measurement band, which ranges from 100Hz to 10kHz.

To meet the first challenge and make the LIGO interferometer more sensitive to gravitational waves, Fabry-Perot optical storage cavities are built into each arm of the LIGO detector, so the light effectively bounces back and forth in the arm many times before returning to the beamsplitter. By making the light beam traverse the arm length multiple times, the light accumulates extra phase shift. One can increase the optical phase shift for a given gravitational wave by increasing the arm cavity storage time, up to the point where the storage time is half the gravitational wave period, at which point further storage time offers no advantages.

The conversion of gravitational wave strain into differential phase shift is given by

$$\left| \frac{\delta\phi}{\delta h} \right| = \frac{8\pi\nu_1\tau_s}{\sqrt{1 + (4\pi f\tau_s)^2}} = \frac{6.2 \times 10^{12}}{\sqrt{1 + \left(\frac{f}{90\text{Hz}}\right)^2}} \text{ radians of phase shift per unit strain} \quad (1.11)$$

where ϕ is the optical phase shift, h is the gravitational wave amplitude, f is the gravitational wave frequency, $\nu_1 = 2.8 \times 10^{14}$ Hz is the laser frequency (the laser wavelength is 1.064 μm), and $\tau_s = 8.8 \times 10^{-4}$ sec. is the optical storage time of the arm cavity.

The second challenge is to be insensitive to other effects which might cause differential phase shifts, such as seismic motion and thermal motion which can drive the mirrors and change the arm length. This is why the arm cavities are each 4km long. As the arm length increases, one can maintain the optical storage time while decreasing the number of times the light bounces off of each end mirror, thereby reducing optical losses and minimizing sensitivity to motions of the optics caused by thermal noise and seismic noise.

The third challenge is to be as sensitive as possible to differential phase shifts at the beamsplitter. Even though the LIGO interferometers should be excellent transducers, a strain of 10^{-21} only results in a differential phase shift of 4×10^{-9} radians.

The optical phase sensitivity requirements for LIGO can be deduced from the target noise floor shown in figure 1.3 (from the LIGO Science Requirements Document [LIGO SRD '95]). Below 150Hz the noise floor is caused by random mirror motion which is driven by seismic and thermal noise. Above 150Hz, the noise floor is limited by the optical phase sensing limit set by photon counting statistics, colloquially known as "shot noise." This limit is determined from the gravitational strain to optical phase conversion efficiency

for LIGO (given by eqn. 1.11) times a shot noise limited optical phase sensitivity of 7×10^{-11} radians/ $\sqrt{\text{Hz}}$.

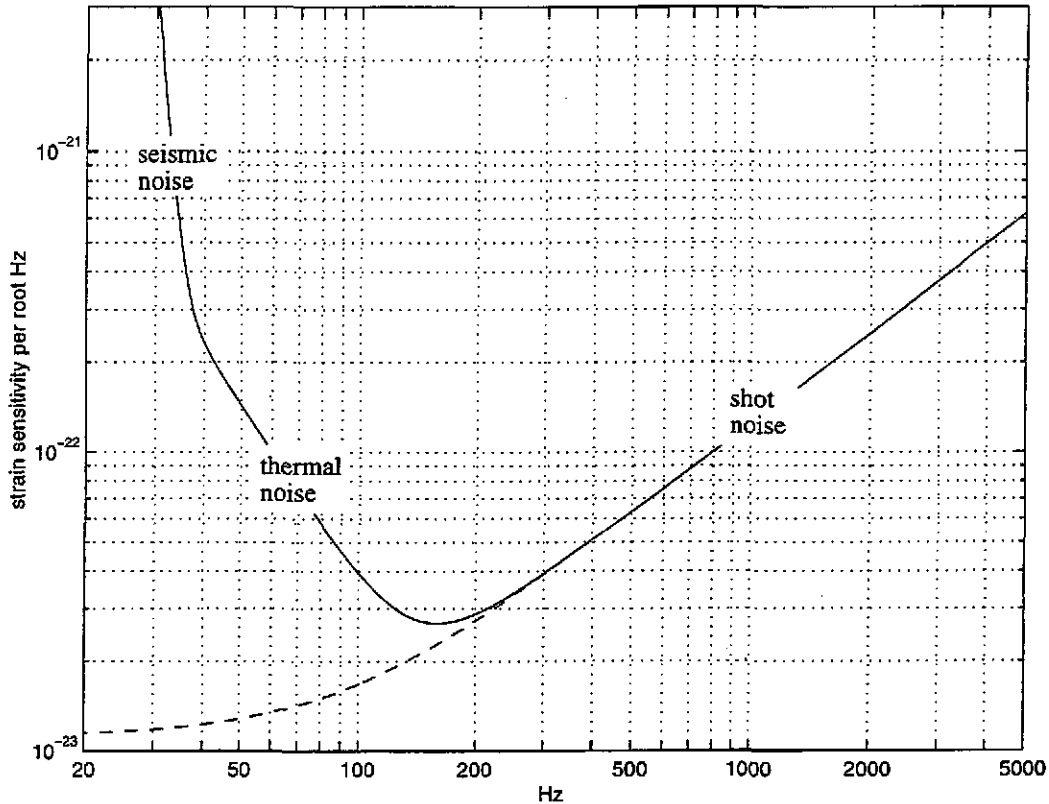


Figure 1.3: LIGO noise curve. The solid line is the total noise floor, and the dashed line is the shot noise limit contribution to that noise.

This level of phase sensitivity has never been demonstrated for this type of instrument. The detection of these small phase differences is the focus of this thesis.

In chapter 2, we show the basic optical configuration and readout scheme for our experiment, and describe the fundamental phase sensitivity for this type of interferometer. The ultimate limit of sensitivity is set by the statistics of photon arrival. We show that as the photon arrival rate increases, the signal to noise ratio improves as $1/\sqrt{\text{Optical power}}$.

The Phase Noise Interferometer (PNI) is described in chapter 3, along with the steps taken to control the instrument and reduce the noise at the output. The results of the experiment are described in chapters 4 and 5. Chapter 4 discusses one of the most serious problems we encountered, thermal lensing, and chapter 5 describes the final spectrum measured with the instrument.

Chapter 2

Interferometer Configuration and Sensitivity Limits

One fundamental limit of the fringe sensitivity of a Michelson interferometer is determined by the statistics of photon counting. In this chapter we develop the theoretical sensitivity limit for the frontally-modulated power-recycled Michelson interferometer used in this experiment. The basic layout of the interferometer we use is shown below in figure 2.1. We first develop the sensitivity of a simple Michelson interferometer, describe the Schnupp modulation scheme we use to measure the changes in the Michelson interferometer arm length, and discuss the impact of adding power recycling. We then calculate the maximum signal to noise ratio such an interferometer can achieve based on a quantum mechanical description of the photon arrival statistics.

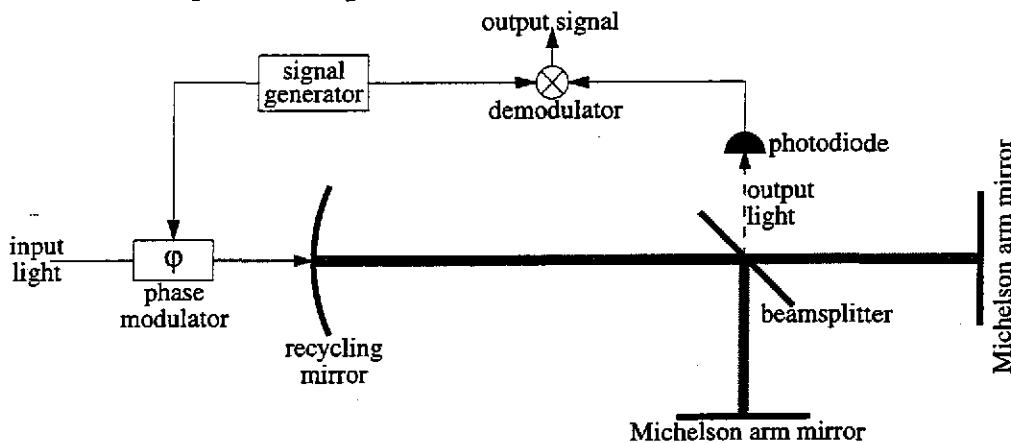


Figure 2.1: Schematic view of recycled Michelson interferometer with frontal modulation. The modulator puts phase modulation sidebands onto the light, the sidebands are used by the readout scheme to determine how far the Michelson interferometer (the three mirrors on the right side of the diagram) is from the optimal working point. The two arms of the Michelson interferometer have macroscopically different lengths, which is required by the readout scheme.

2.1 Michelson Interferometer Sensitivity and Schnupp Modulation

Description

A simple Michelson interferometer comprises a beamsplitter and two arm mirrors. The beamsplitter divides an incident laser beam into two output beams, which are reflected by the arm mirrors back to the beamsplitter where they interfere. The interference between the two return beams gives information about the relative length of the arms. Figure 2.2 shows the beams for this configuration.

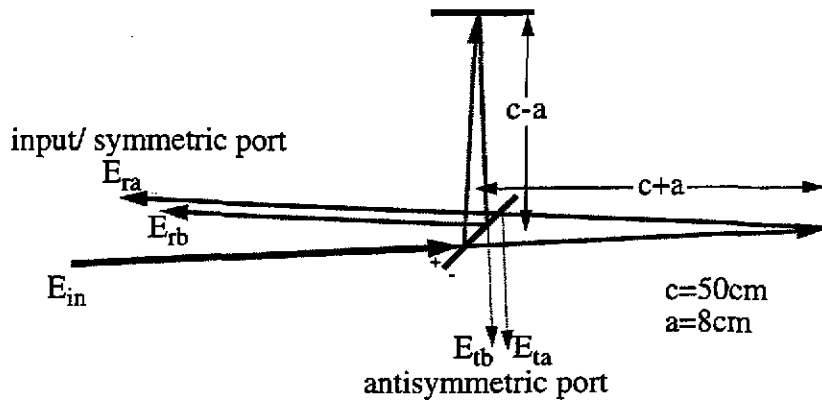


Figure 2.2: Schematic view of an asymmetric Michelson interferometer.

The incident and reflected beams in the PNI are coaxial, but have been separated in this diagram for clarity. Although the symbol placement implies some propagation distance, the fields E_{in} , E_t , and E_r are defined immediately after their last beamsplitter interaction.

The Michelson interferometer arms in this experiment were different lengths. A macroscopic asymmetry adds a frequency selectivity to the transfer function, and is a key part of the length measurement scheme. The length (and angle, see section 3.4) detection is accomplished with a RF heterodyne technique called Schnupp Modulation. [Schnupp '86, see also Regehr '95.] Phase modulation sidebands are impressed on the light before it enters the interferometer (hence the term frontal modulation), and differential misalignments convert the phase modulation into amplitude modulation at the antisymmetric port of the beamsplitter. The Michelson interferometer's antisymmetric port is held at a dark fringe, so ideally none of the power of the carrier is transmitted to the detector, instead, it is reflected back towards the laser. However, the concept behind Schnupp modulation is that the macroscopic asymmetry forces some of the power in the sidebands to be transmitted through the antisymmetric port. If the carrier begins to slip away from the dark fringe, carrier light transmitted out of the dark port begins to beat against sidebands, producing the RF amplitude modulation which we measure.

This scheme was chosen for the LIGO readout because it enables power recycling (discussed in the next section), allows frontal modulation (so the modulators do not experience the full recycled light power), and requires a minimum number of large, suspended optics (which are complicated and expensive). To meet LIGO's requirements, there will be 300 Watts of power incident on the LIGO beamsplitter [LIGO SRD '95]. By using a fron-

tally-modulated, recycled configuration, LIGO can reach high circulating power levels with only 10 Watts of input power, no active intracavity optical elements, and only a few watts of output power on the photodetectors.

Michelson Interferometer's Response to Phase Modulated Light

A recycled Michelson interferometer can be described as a series of simpler optical elements. One element is the unrecycled asymmetric Michelson interferometer. Following figure 2.2, we describe the electric fields of the four exit paths [following Gonzalez '97]:

$$\begin{aligned} E_{ra}(k) &= E_{in} \cdot t_{BS}^2 \cdot e^{-ik2(c+a)} \\ E_{rb}(k) &= E_{in} \cdot r_{BS}^2 \cdot e^{-ik2(c-a)} \\ E_{ta}(k) &= E_{in} \cdot t_{BS} \cdot -r_{BS} \cdot e^{-ik2(c+a)} \\ E_{tb}(k) &= E_{in} \cdot t_{BS} \cdot r_{BS} \cdot e^{-ik2(c-a)}. \end{aligned}$$

Here, r_{BS} and t_{BS} are the field reflectivity and transmission, respectively, of the beamsplitter, k is the wavenumber of light, c is the average, one-way length of the arms (50cm) and a is the asymmetry (8cm). The reflected fields are coaxial, as are the transmitted fields; the total field of the reflected beam is

$$E_r(k) = E_{ra}(k) + E_{rb}(k) = E_{in} [t_{BS}^2 \cdot e^{-ik2(c+a)} + r_{BS}^2 \cdot e^{-ik2(c-a)}]. \quad (2.1)$$

We can rewrite the field in terms of the fractional power the beamsplitter transmits and reflects, and the difference between them.

$$T_{BS} \equiv t_{BS}^2, \quad R_{BS} \equiv r_{BS}^2, \quad U_{BS} \equiv R_{BS} - T_{BS}$$

The reflected field then becomes

$$\begin{aligned} E_r(k) &= E_{in} e^{-ik2c} (\cos(2ka) + iU_{BS} \sin(2ka)) \\ &\approx E_{in} e^{-ik2c} \cos(2ka) \end{aligned} \quad (2.2)$$

for a 50/50 beamsplitter. The field transmitted to the other port of the Michelson interferometer (alternately called the antisymmetric port or the dark port) takes the form

$$E_t(k) = E_{ta}(k) + E_{tb}(k) = 2iE_{in} \cdot t_{BS} \cdot r_{BS} \cdot e^{-ik2c} \cdot \sin(2ka). \quad (2.3)$$

If the beamsplitter is not perfectly balanced, then the minimum reflected field increases from 0 to $E_r(k)_{\min} = E_{in} U_{BS}$, but the maximum reflected field remains the same (which

is where this experiment operates). The biggest effect an unequal beamsplitter would have is to reduce the transmitted light. The reduction factor is $\sqrt{1 - U_{BS}^2} \approx 1 - 0.01$ for our beamsplitter (see chapter 5), so this effect has been ignored. Equations 2.2 and 2.3 are true for any wavenumber, k . We can specialize these expressions to describe the salient features of the Michelson interferometer in this experiment.

The first specialization involves the laser light incident on the interferometer. The light from the laser is single frequency and single spatial mode. The light is passed through a resonant phase modulator which adds sidebands to the light which are separated from the carrier frequency by ω_m radians/sec. The light at the output of the phase modulator has the form

$$\begin{aligned}\vec{E}_{in}(t) &= E_{in} e^{i\{\omega t + \Gamma \sin(\omega_m t)\}} \\ &\approx E_{in} e^{i\omega t} [J_0(\Gamma) + 2iJ_1(\Gamma) \sin(\omega_m t) + O(J_2(\Gamma))] \\ &\approx E_{in} e^{i\omega t} [J_0(\Gamma) + J_1(\Gamma) e^{i\omega_m t} - J_1(\Gamma) e^{-i\omega_m t}]\end{aligned}\quad (2.4)$$

representing the carrier, the upper sideband, and the lower sideband. Here, Γ is the modulation depth, and $J_0(\Gamma)$ and $J_1(\Gamma)$ are Bessel functions of the first kind [Oliver '72]. We ignore the terms in $J_2(\Gamma)$ and above, because the modulation depth for our experiment was small ($\Gamma = 0.49$) and the higher order terms appear at higher harmonics.

There are a series of approximations we can make to the expressions of the output fields of the Michelson interferometer if we consider only the three primary frequencies which emerge from the phase modulator. First, the transmitted port of the Michelson interferometer is actively servoed to the dark fringe of the carrier, so we rewrite the asymmetry length a as

$$a \equiv A + \delta, \quad (2.5)$$

where A is the nominal asymmetry of 8cm and δ is the variation from that asymmetry. Since these variations are quite small, it is reasonable to make the approximations

$$\sin(2k_0 a) = \sin(2k_0 A + 2k_0 \delta) \approx 2k_0 \delta \quad \text{and} \quad \cos(2k_0 a) = 1 \quad (2.6)$$

where k_0 is the wavenumber of the carrier.

Next we define the wavenumbers for the upper and lower sidebands to be $k_+ \equiv k_0 + k_{SB}$, and $k_- \equiv k_0 - k_{SB}$ where $k_{SB} = \omega_m/c$. We make the approximations

$$\begin{aligned}
\sin(2k_+a) &= \sin(2k_0A + 2k_{SB}A + 2k_0\delta + 2k_{SB}\delta) \\
&\approx \sin(2k_0\delta + 2k_{SB}A) \\
&\approx 2k_0\delta \cos(2k_{SB}A) + \sin(2k_{SB}A)
\end{aligned} \tag{2.7}$$

and

$$\sin(2k_-a) \approx 2k_0\delta \cos(2k_{SB}A) - \sin(2k_{SB}A) \tag{2.8}$$

$$\cos(2k_+a) \approx \cos(2k_{SB}A) - 2k_0\delta \sin(2k_{SB}A) \tag{2.9}$$

$$\cos(2k_-a) \approx \cos(2k_{SB}A) + 2k_0\delta \sin(2k_{SB}A). \tag{2.10}$$

We make a further approximation to the amplitude of the fields reflected by the Michelson interferometer by adding a loss term, L , which represents the power lost to absorption, scattering, and light conversion into higher order spatial modes. This reflectivity loss reduces the power reflected by the Michelson interferometer by a factor of $1 - L$, reducing the reflected field by $\sqrt{1 - L}$. The two dominant loss mechanisms in this experiment, at the power levels used, were unwanted reflections from the back surface of the beamsplitter (see section 5.2.1) and the contrast loss caused by thermal lensing of the beamsplitter (see chapter 4).

We include the loss, and rewrite the field reflectivity of the Michelson interferometer for the carrier as

$$\begin{aligned}
r_{M0} &= \frac{E_r(k_0)}{E_{in}(k_0)} = \sqrt{1 - L} e^{-ik_0 2c} \cos(2k_0 a) \\
&\approx \left(1 - \frac{L}{2}\right) e^{-ik_0 2c}.
\end{aligned} \tag{2.11}$$

We combine eqns. 2.2 and 2.9 to get the upper sideband reflectivity,

$$r_{M+} \approx \left(1 - \frac{L}{2}\right) e^{-ik_0 2c} e^{-ik_{SB} 2c} [\cos(2k_{SB}A) - 2k_0\delta \sin(2k_{SB}A)] \tag{2.12}$$

and likewise combine eqns. 2.2 and 2.10 to get the lower sideband reflectivity.

$$r_{M-} \approx \left(1 - \frac{L}{2}\right) e^{-ik_0 2c} e^{ik_{SB} 2c} [\cos(2k_{SB}A) + 2k_0\delta \sin(2k_{SB}A)] \tag{2.13}$$

If we assume that the field transmission and reflection of the beamsplitter are reasonably well matched, then the transmission of the Michelson interferometer for the carrier field in the TEM_{00} mode is found by combining eqns. 2.3 and 2.6.

$$t_{M0} \approx ie^{-ik_0 2c} 2k_0 \delta \quad (2.14)$$

The transmission for the sidebands is found by combining eqns. 2.3 and 2.7 or 2.8.

$$t_{M+} \approx ie^{-ik_0 2c} e^{-ik_{SB} 2c} (2k_0 \delta \cos(2k_{SB} A) + \sin(2k_{SB} A)) \quad (2.15)$$

$$t_{M-} \approx ie^{-ik_0 2c} e^{ik_{SB} 2c} (2k_0 \delta \cos(2k_{SB} A) - \sin(2k_{SB} A)) \quad (2.16)$$

Using these expressions for the transmission and reflection coefficients, we can derive the behavior of the recycling cavity.

2.2 Power Recycling Cavity

Since the Michelson interferometer is highly reflective, we can treat it as a mirror with frequency sensitive transmission and reflection described by eqns. 2.11 - 2.16. Instead of throwing the reflected power away, it is stored within an optical resonator called the “power recycling cavity”, a Fabry-Perot cavity formed between the Michelson “mirror” and a cavity input mirror, commonly called the recycling mirror.

The field inside a Fabry-Perot cavity like the one shown in figure 2.3 can be easily related to the incident field for slowly varying configurations.

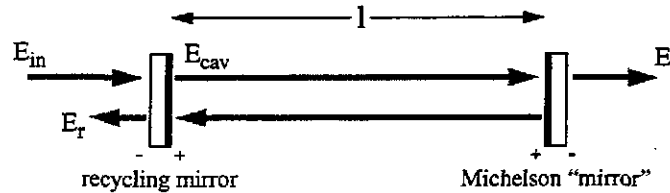


Figure 2.3: Fields within a Fabry-Perot cavity

The steady state field within the cavity is

$$E_{cav}(k) = E_{in}(k) \frac{t_{RM}}{1 - r_{RM} \cdot r_{MM}(k) \cdot e^{-ik2l}} \quad (2.17)$$

where $r_{MM}(k)$ [§] is the field reflectivity of the Michelson “mirror”, and t_{RM} and r_{RM} are the field transmission and reflectivity of the recycling mirror. The field transmitted by the recycling cavity is related to the field within the cavity by the transmission of the rear mirror and the extra propagation phase.

§. The Michelson interferometer’s asymmetry adds a strong frequency dependence to the reflectivity.

$$E_{\text{out}}(k) = E_{\text{cav}}(k) \cdot t_{\text{MM}}(k) \cdot e^{-ikl} = E_{\text{in}}(k) \frac{t_{\text{RM}} \cdot t_{\text{MM}}(k) \cdot e^{-ikl}}{1 - r_{\text{RM}} \cdot r_{\text{MM}}(k) \cdot e^{-ik2l}} \quad (2.18)$$

It is worth considering how the transmission of the recycling cavity is related to the transmission of the rear Michelson “mirror”. If $E_{\text{cav}}(k)$ were unaffected by differential phase shifts in the Michelson interferometer, then a standard Michelson interferometer with a large input power would be identical to a recycled Michelson interferometer with a proportionately smaller input power (for dynamic cavities, this is only true for measurements at frequencies below pole frequency of the recycling cavity, which is 13kHz for this interferometer). Since the cavity field is a function of the reflectivity of the Michelson interferometer, this comparison does not strictly hold, but two approximations used in the following section do lead to that result. Both approximations hold when the Michelson interferometer’s antisymmetric port is near the dark fringe of the carrier. First, the reflectivity for the carrier is proportional to $\cos(2k_0a)$, which we set to 1 in eqn. 2.6. Second, as is shown in eqn. 2.30, the signal we measure results from the product of the fixed component of the carrier transmission with the fluctuating component of the sideband transmission and from the product of the fixed component of the sideband transmission with the fluctuating component of the carrier transmission. Since the fixed component of the carrier transmission in the TEM_{00} mode is held to 0, the fluctuations in the sideband reflection and transmission are ignored.

Using the expressions for the transmission and reflection coefficients of the Michelson “mirror”, we can describe the transmission coefficients of the recycling cavity. Again, several approximations are used. First, the carrier and the sidebands are resonant in the recycling cavity, so

$$e^{-ik_0 2(l+c)} = 1, \quad e^{-ik_+ 2(l+c)} = 1, \quad e^{-ik_- 2(l+c)} = 1. \quad (2.19)$$

The cavity transmission for the carrier becomes

$$t_0 = \frac{E_{\text{out}}(k_0)}{E_{\text{in}}(k_0)} = \frac{t_{\text{RM}} \cdot i e^{-ik_0 2c} 2k_0 \delta \cdot e^{-ikl}}{1 - r_{\text{RM}} \cdot \left(1 - \frac{L}{2}\right)}. \quad (2.20)$$

If we absorb the losses from the recycling mirror into the loss L of the Michelson “mirror,” we can rewrite the recycling mirror reflectivity as

$$r_{\text{RM}} = \sqrt{1 - t_{\text{RM}}^2} \approx 1 - \frac{T_{\text{RM}}}{2} \quad (2.21)$$

where $T_{\text{RM}} = t_{\text{RM}}^2$ is the power transmission of the recycling mirror. The carrier transmission then simplifies to

$$t_0 \approx \frac{2it_{\text{RM}} \cdot 2k_0\delta \cdot e^{-ik_0(l+2c)}}{T_{\text{RM}} + L} \quad (2.22)$$

We now examine the transmission coefficients for the sidebands. By substituting the expressions for the Michelson interferometer interactions with the sidebands (eqns. 2.12 - 2.16) into the cavity output field equation (2.18), we get the sideband transmission of the recycled Michelson interferometer. The transmission for the upper sideband is

$$t_+ \approx \frac{t_{\text{RM}} \cdot ie^{-i(k_0+k_{\text{SB}})(2c+l)} (2k_0\delta \cos(2k_{\text{SB}}A) + \sin(2k_{\text{SB}}A))}{1 - r_{\text{RM}} \cdot \left(1 - \frac{L}{2}\right) (\cos(2k_{\text{SB}}A) - 2k_0\delta \sin(2k_{\text{SB}}A))} \quad (2.23)$$

and the transmission of the lower sideband is

$$t_- \approx \frac{t_{\text{RM}} \cdot ie^{-i(k_0-k_{\text{SB}})(2c+l)} (2k_0\delta \cos(2k_{\text{SB}}A) - \sin(2k_{\text{SB}}A))}{1 - r_{\text{RM}} \cdot \left(1 - \frac{L}{2}\right) (\cos(2k_{\text{SB}}A) + 2k_0\delta \sin(2k_{\text{SB}}A))} \quad (2.24)$$

For convenience, let $SA \equiv \sin(2k_{\text{SB}}A)$ and $CA \equiv \cos(2k_{\text{SB}}A) \approx 1 - SA^2/2$. We can then rewrite the transmissions as

$$t_+ \approx \frac{2t_{\text{RM}} \cdot ie^{-i(k_0+k_{\text{SB}})(2c+l)} (2k_0\delta CA + SA)}{T_{\text{RM}} + L + (SA^2 + 4k_0\delta SA)} \quad (2.25)$$

and

$$t_- \approx \frac{2t_{\text{RM}} \cdot ie^{-i(k_0-k_{\text{SB}})(2c+l)} (2k_0\delta CA - SA)}{T_{\text{RM}} + L + (SA^2 - 4k_0\delta SA)} \quad (2.26)$$

Using these expressions for the interferometer transmission, we can examine the impact of changing the differential length on the transmitted light power.

We recall that the form of the field incident on the interferometer (eqn. 2.4) is

$$E_{\text{in}} = \sqrt{P_{\text{in}}} (J_0(\Gamma)e^{i\omega t} + J_1(\Gamma)e^{i(\omega+\omega_m)t} - J_1(\Gamma)e^{i(\omega-\omega_m)t}) \quad (2.27)$$

where P_{in} is the input power, Γ is the modulation index, and $J_0(\Gamma)$ and $J_1(\Gamma)$ are Bessel functions. Let

$$J_0 \equiv J_0(\Gamma) \quad J_1 \equiv J_1(\Gamma)$$

so the output field is

$$E_{out} = \sqrt{P_{in}} e^{i\omega t} (t_0 J_0 + t_+ J_1 e^{i\omega_m t} - t_- J_1 e^{-i\omega_m t}) . \quad (2.28)$$

The output power, $E_{out}^* E_{out}$, then has components at DC, the modulation frequency, and twice the modulation frequency. The power at the output of the interferometer at the modulation frequency is

$$P_{mod} = P_{in} [e^{i\omega_m t} (\overline{t_0 J_0 t_+ J_1} - \overline{t_0 J_0 t_- J_1}) + e^{-i\omega_m t} (\overline{t_0 J_0 t_+ J_1} - \overline{t_0 J_0 t_- J_1})] . \quad (2.29)$$

The signal in this term is used to measure the deviations from the dark fringe. We see that the power at the modulation frequency is the carrier field heterodyned with the sideband fields. The interferometer length is generated by mixing down the power on the photodiode with a reference from the signal used to modulate the light.

To evaluate 2.29, we must expand the products $\overline{t_0 t_+}$, $\overline{t_0 t_-}$, and their conjugates to first order in $k_0 \delta$. If we let $\psi \equiv k_{SB}(2c + l)$, then these products become

$$\begin{aligned} \overline{t_0 t_+} &= \frac{-2it_{RM} \cdot 2k_0 \delta \cdot e^{ik_0(l+2c)}}{T_{RM} + L} \cdot \frac{2t_{RM} \cdot ie^{-i(k_0 + k_{SB})(2c+l)} (2k_0 \delta CA + SA)}{T_{RM} + L + (SA^2 + 4k_0 \delta SA)} \\ &\approx \frac{8T_{RM} \cdot SA}{(T_{RM} + L) \cdot (T_{RM} + L + SA^2)} \cdot k_0 \delta \cdot e^{-i\psi} \end{aligned} \quad (2.30)$$

and

$$\overline{t_0 t_-} \approx \frac{-8T_{RM} \cdot SA}{(T_{RM} + L) \cdot (T_{RM} + L + SA^2)} \cdot k_0 \delta \cdot e^{i\psi} . \quad (2.31)$$

We can now write the expression for the output power at the modulation frequency. Since this power is detected by a photodiode, we will also include η , the quantum efficiency of the detector, which is about 0.85 electrons/ photon for our detector [Csatorday '98]. The detected output power at the modulation frequency is

Carrier/ Sideband Ratio: There are various light interrogation points in the interferometer which allow us to compare the power distribution between the carrier and the sidebands. The carrier to sideband power ratio at the input is

$$CSB_{in} = \frac{J_0^2}{J_1^2}. \quad (2.37)$$

The carrier to sideband ratio in the recycling cavity is then

$$CSB_{BS} = \frac{J_0^2 RG_0}{J_1^2 RG_{+,-}} = CSB_{in} \left(\frac{L + T_{RM} + SA^2}{L + T_{RM}} \right)^2. \quad (2.38)$$

The carrier to sideband ratio at the dark port is related to the carrier to sideband ratio at the beamsplitter by the transmission of the Michelson interferometer. The total power transmission of the *Michelson interferometer* for the carrier at resonance is L_C , the contrast loss (see eqn. 2.59). The sideband power transmission is $\sin^2(2k_{SB}A) + L_C$, so the output ratio is

$$CSB_{dp} = \left(\frac{J_0^2}{J_1^2} \right) \left(\frac{L + T_{RM} + SA^2}{L + T_{RM}} \right)^2 \left(\frac{L_C}{\sin^2(2k_{SB}A) + L_C} \right). \quad (2.39)$$

2.4 Noise

The goal of this experiment is to demonstrate a sensitive phase detection. The sensitivity to phase changes was developed in sections 2.2 and 2.3. In this section we describe the fundamental quantum-mechanical noise which limits the phase sensitivity. First, a derivation of the sensing noise is given, which follows [Caves '80, and Caves '81]. Then the "shot noise" description will be used to relate that result to the sensing scheme and interferometer configuration which is employed for this experiment.

To derive the sensitivity limit of phase detection, we consider a beam of laser light incident on a simple Michelson interferometer.

The incident light is of the form

$$E_1^+ = \begin{cases} A e^{i(kx - \omega t)} - iA e^{i(\Phi - \mu)} \sin(\phi/2) e^{i(ky - \omega t)}, & y > x \\ A e^{i\Phi} \cos(\phi/2) e^{i(kx - \omega t)}, & y < x \end{cases} \quad (2.40)$$

and the field entering from the other port is

$$E_2^+ = \begin{cases} Ae^{i\Phi} \cos(\phi/2) e^{i(ky - \omega t)}, & y > x \\ Ae^{i(ky - \omega t)} - iAe^{i(\Phi + \mu)} \sin(\phi/2) e^{i(kx - \omega t)}, & y < x \end{cases} \quad (2.41)$$

where ϕ is the phase shift between the arms, Φ is the mean phase of the arms (in radians), and μ is the relative phase shift of the beamsplitter.

Another basis to use is the output beams of the interferometer. These fields are related to the “in” fields by

$$\begin{aligned} E_1^- &= e^{-i\Phi} [ie^{i\mu} E_1^+ \sin(\phi/2) + E_2^+ \cos(\phi/2)] \\ E_2^- &= e^{-i\Phi} [E_1^+ \cos(\phi/2) + ie^{-i\mu} E_2^+ \sin(\phi/2)]. \end{aligned} \quad (2.42)$$

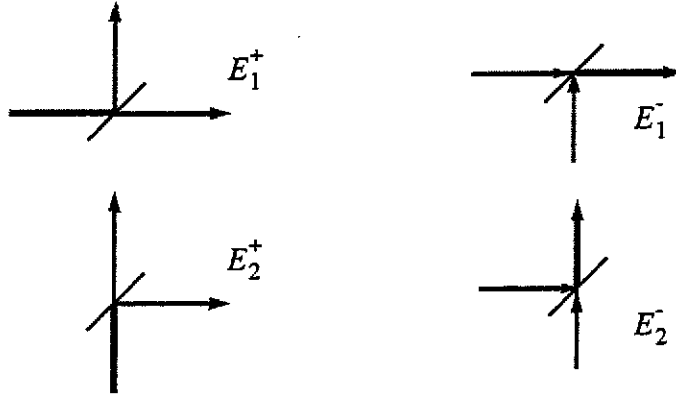


Figure 2.4: Field Eigenstates described by equations 2.40 through 2.42.

The light from the laser is in the coherent state [Loudon '83]. The creation and annihilation operators for the input fields are a_1^\dagger , a_1 , a_2^\dagger , and a_2 . [See, for example, Sakurai '85.] The respective operators for the “out” fields are then

$$\begin{aligned} c_1 &= e^{i\Phi} [-ie^{-i\mu} a_1 \sin(\phi/2) + a_2 \cos(\phi/2)] \\ c_2 &= e^{i\Phi} [a_1 \cos(\phi/2) - ie^{-i\mu} a_2 \sin(\phi/2)]. \end{aligned} \quad (2.43)$$

The number operator for the number of photons exiting port 2 of the interferometer is then

$$\begin{aligned} c_2^\dagger c_2 &= a_1^\dagger a_1 \cos^2(\phi/2) + a_2^\dagger a_2 \sin^2(\phi/2) \\ &\quad - i \sin(\phi/2) \cos(\phi/2) (e^{i\mu} a_1^\dagger a_2 - e^{i\mu} a_2^\dagger a_1) \end{aligned} \quad (2.44)$$

and the number operator squared is

$$\begin{aligned}
(c_2^\dagger c_2)^2 &= a_1^\dagger a_1 a_1^\dagger a_1 \cos^4(\phi/2) \\
&+ a_2^\dagger a_2 \sin^2(\phi/2) (\text{terms in } a_1^\dagger a_1, a_2^\dagger a_2, \text{ or singleton } a_2 \text{ or } a_2^\dagger) \\
&+ \text{terms in } a_1^\dagger a_1 \text{ and singleton } a_2 \text{ or } a_2^\dagger \\
&- \sin^2(\phi/2) \cos^2(\phi/2) (\text{terms in } a_2^2 \text{ or } a_2^{\dagger 2}) \\
&+ \sin^2(\phi/2) \cos^2(\phi/2) (a_1^\dagger a_1 a_2 a_2^\dagger + a_1 a_1^\dagger a_2^\dagger a_2).
\end{aligned} \tag{2.45}$$

We prepare the interferometer so that the “in” state field 1 is the coherent state excited to a level α , which contains, on average, N photons. The field entering the dark port is the vacuum field, or the ground state of the propagating electromagnetic field

$$|\text{in}\rangle = |(\text{field } 1 = \alpha), (\text{field } 2 = 0)\rangle = |\alpha, 0\rangle.$$

Since the field entering port 2 is the vacuum state, the expectation value of any operator with different numbers of a_2^\dagger and a_2 will be 0. We also note that:

$$\begin{aligned}
\langle \alpha, 0 | a_1^\dagger a_1 | \alpha, 0 \rangle &= |\alpha|^2 = N, \\
\langle \alpha, 0 | a_2^\dagger a_2 | \alpha, 0 \rangle &= 0, \text{ and} \\
\langle \alpha, 0 | a_2 a_2^\dagger | \alpha, 0 \rangle &= 1.
\end{aligned} \tag{2.46}$$

We now evaluate the expectation value and the variance of the number of photons emerging from the second port.

$$\langle N_2 \rangle = \langle \alpha, 0 | c_2^\dagger c_2 | \alpha, 0 \rangle = N \cos^2(\phi/2) \tag{2.47}$$

The expectation value of N_2^2 is

$$\begin{aligned}
\langle N_2^2 \rangle &= \langle \alpha, 0 | (c_2^\dagger c_2)^2 | \alpha, 0 \rangle \\
&= \cos^4(\phi/2) N(N+1) \\
&+ \sin^2(\phi/2) \cos^2(\phi/2) \langle \alpha, 0 | (a_1^\dagger a_1 a_2 a_2^\dagger + a_1 a_1^\dagger a_2^\dagger a_2) | \alpha, 0 \rangle \\
&= \cos^4(\phi/2) N(N+1) + \sin^2(\phi/2) \cos^2(\phi/2) N
\end{aligned} \tag{2.48}$$

so the uncertainty in the output becomes

$$\begin{aligned}
(\Delta N_2)^2 &= \langle N_2^2 \rangle - \langle N_2 \rangle^2 \\
&= \cos^4(\phi/2) N + \sin^2(\phi/2) \cos^2(\phi/2) N \\
&= N \cos^2(\phi/2),
\end{aligned} \tag{2.49}$$

or

$$\Delta N_2 = \sqrt{N} |\cos(\phi/2)| = \sqrt{\langle N_2 \rangle}. \quad (2.50)$$

This relationship is the basis of the uncertainty associated with measuring the phase of an interferometer and the origin of “shot noise.” Figure 2.5 shows a plot of the average (normalized) output of an interferometer, along with the associated uncertainty.

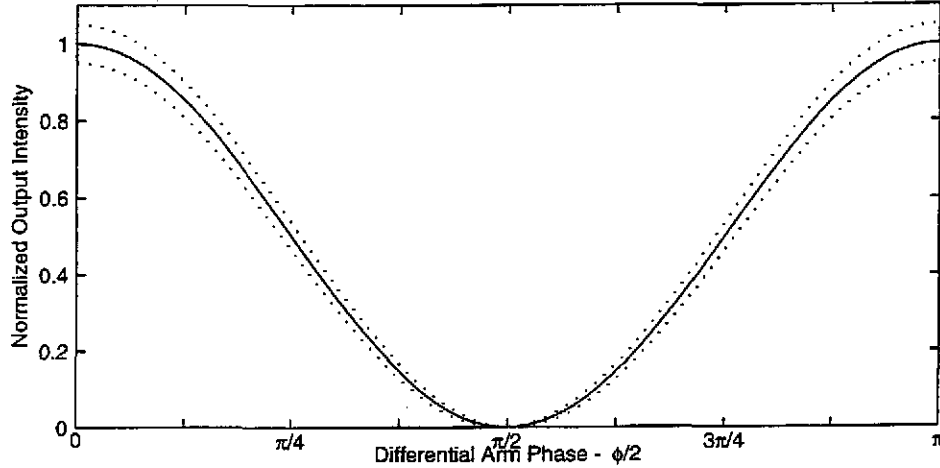


Figure 2.5: Plot of $(N_2 \pm \Delta N_2)/N$ vs. differential phase for $N=400$.

If you attempt to measure the phase difference between the two arms by measuring the intensity of the output light, then the signal is equal to

$$\frac{d\langle N_2 \rangle}{d\phi} = N \cos(\phi/2) \sin(\phi/2). \quad (2.51)$$

This sets the limit of the phase sensitivity for a detection scheme with a diode at the output which determines the phase difference between the arms by measuring the power at the antisymmetric port to be

$$\Delta\phi = \frac{d\phi}{d\langle N_2 \rangle} \Delta N_2 = \frac{\sqrt{N} |\cos(\phi/2)|}{N \cos(\phi/2) \sin(\phi/2)} = \frac{1}{\sqrt{N} \sin(\phi/2)} \geq \frac{1}{\sqrt{N}}. \quad (2.52)$$

It is important to note that N is the expected number of photons at the beamsplitter, not at the photodiode.

It is important to consider the spectral analysis of the measurement. We rewrite the sensitivity in terms of photon arrival rate, rather than integrated photon number. The photon arrival rate at the detector, \dot{N}_2 , is related to the phase by

$$\langle \dot{N}_2 \rangle = N \cos^2(\phi/2). \quad (2.53)$$

Since the photon arrival times are Poisson distributed, the Wiener-Khintchine theorem [see, for example, Yariv '91, chapter 10] states that the amplitude spectral density of the photon arrival rate is

$$\Delta\tilde{N}_2(f) = \sqrt{2\langle\dot{N}_2\rangle} \frac{\text{photons}}{\text{sec}\sqrt{\text{Hz}}} \quad (2.54)$$

The quantum efficiency of the photodetector means that only some of the arriving photons will be measured, therefore the measured arrival rate will be reduced to $\eta\dot{N}_2$. The measured power fluctuations are

$$\Delta\tilde{P}_{\text{out}} = \sqrt{2h\nu\eta P_{\text{out}}} \frac{\text{Watts}}{\sqrt{\text{Hz}}} \quad (2.55)$$

The phase uncertainty measured by a detector can then be expressed as

$$\begin{aligned} \Delta\tilde{\Phi}(f) &= \frac{d\phi}{d\langle\dot{N}_2\rangle} \Delta\tilde{N}_2(f) = \frac{d\phi}{d\langle P_{\text{out}}\rangle} \Delta\tilde{P}_{\text{out}}(f) \\ &= \sqrt{\frac{2h\nu}{\eta P_{\text{BS}}}} \frac{\text{radians}}{\sqrt{\text{Hz}}} \end{aligned} \quad (2.56)$$

2.5 Sensitivity limit for modulation readout scheme with optical losses

We can now compare the result of an idealized phase detection to an analysis of the phase sensitivity limit for the interferometer configuration and readout scheme employed for this experiment.

The readout scheme is *slightly* different from a pure intensity readout in that the measured intensity is not measured at DC, but is instead is measured at 25.556 MHz and demodulated to give the interferometer phase measurement.

In eqn. 2.32 we calculated the measured signal at the modulation frequency to be

$$\Delta P_{\text{out}} = \frac{\eta P_{\text{in}} 8J_0 J_1 T_{\text{RM}} \cdot SA}{(T_{\text{RM}} + L) \cdot (T_{\text{RM}} + L + SA^2)} \cdot \Delta\phi \quad (2.57)$$

To establish the phase sensing limit, we invert this expression, and rewrite the results in terms of amplitude spectral density of noise.

$$\Delta\tilde{\Phi}(f) = \frac{(T_{\text{RM}} + L) \cdot (T_{\text{RM}} + L + SA^2)}{\eta P_{\text{in}} 8J_0 J_1 T_{\text{RM}} \cdot SA} \cdot \Delta\tilde{P}_{\text{out}}(f) \quad (2.58)$$

The measured noise from the “shot noise” of the light incident on the detector at the dark port has the form $\Delta\tilde{P}_{\text{out}}(f) = \sqrt{2h\nu\eta P_{\text{out}}}$ §. The noise at different frequencies is uncorrelated, and since we are using a modulation scheme, the noise from the fluctuations in the output intensity are multiplied by an additional $\sqrt{2}$ because both the upper and the lower sidebands are demodulated to the baseband. Henceforth, we will write $\Delta\tilde{P}_{\text{out}}(f) = \sqrt{2}\sqrt{2h\nu\eta P_{\text{out}}}$, and remember that this refers to the noise after the demodulation step, referred back to the diode. To determine P_{out} , we measure the contrast loss of the interferometer. The contrast loss is simply

$$L_C \equiv \text{contrast loss}(k) = \frac{\text{light exiting Michelson dark port}(k)}{\text{light incident on Michelson IFO}(k)}. \quad (2.59)$$

The power contributing to the noise can be in any spatial mode, unlike the signal, which is only detected (for ideal diodes) in the TEM₀₀ mode. At the power levels used in this experiment and with the automatic alignment system operating, the dominant contrast loss mechanism was due to thermally induced wavefront distortions between the beams in the two Michelson interferometer arms. Since the light in the two arms experiences different distortions, (one beams passes through the beamsplitter, and the other does not), the two beams returning to the beamsplitter do not interfere perfectly, so power in higher spatial order modes exits the dark port. This is described more fully in Chapter 4 - Thermal Lensing.

The measured intensity of the carrier light exiting the dark port can be expressed as the incident light (eqn. 2.27) times the recycling gain (eqn. 2.35) times the contrast loss.

$$P_{\text{out},0} = \eta P_{\text{in}} J_0^2 \cdot RG_0 \cdot L_C = \eta P_{\text{in}} J_0^2 \frac{4T_{\text{RM}}}{(L + T_{\text{RM}})^2} \cdot L_C. \quad (2.60)$$

The intensity of each of the sidebands is

$$P_{\text{out},\pm} = \eta P_{\text{in}} J_1^2 \frac{4T_{\text{RM}}(\sin^2(2k_{\text{SB}}A) + L_C)}{(L + T_{\text{RM}} + \sin^2(2k_{\text{SB}}A))^2}. \quad (2.61)$$

The DC intensity measured by the photodiode should be

§. This formula does not account for the extra “non-stationary shot noise” resulting from synchronously demodulating the power in the time-varying sidebands. That added noise is described in equation 2.67

$$\begin{aligned}
P_{\text{out}} &= \eta P_{\text{out},0} + 2\eta P_{\text{out},+/-} \\
&= 2\eta P_{\text{out},+/-} \left(1 + \frac{1}{2} CBS_{\text{dp}}\right) \\
&= \eta P_{\text{in}} 4T_{\text{RM}} \left[\frac{J_0^2 \cdot L_C}{(L + T_{\text{RM}})^2} + \frac{2J_1^2 (SA^2 + L_C)}{(L + T_{\text{RM}} + SA^2)^2} \right].
\end{aligned} \tag{2.62}$$

We can now express the phase sensitivity limit in terms of measured parameters

$$\Delta\tilde{\phi}(f) = \frac{(T_{\text{RM}} + L) \cdot (T_{\text{RM}} + L + SA^2)}{\eta P_{\text{in}} 8J_0 J_1 T_{\text{RM}} \cdot SA} \sqrt{4h\nu\eta P_{\text{out}}}. \tag{2.63}$$

If we set the losses to 0 and assume perfect contrast, then $\Delta\phi$ becomes

$$\begin{aligned}
\Delta\tilde{\phi}(f) &= \frac{(T_{\text{RM}} + SA^2)}{\eta P_{\text{in}} 8J_0 J_1 \cdot SA} \sqrt{4\eta P_{\text{in}} 4T_{\text{RM}} \frac{h\nu 2J_1^2 (SA^2)}{(T_{\text{RM}} + SA^2)^2}} \\
&= \sqrt{\frac{2h\nu T_{\text{RM}}}{\eta P_{\text{in}} 4J_0^2}} \\
&= \sqrt{\frac{2h\nu}{\eta P_{0, \text{BS}}} \text{ radians}} \sqrt{\text{Hz}}
\end{aligned} \tag{2.64}$$

which matches the prediction for a perfect system in eqn. 2.56.

If we consider the losses, then we can expand eqn. 2.63 to express the amplitude spectral density of the shot noise limited phase sensitivity in an interferometer with losses.

$$\begin{aligned}
\Delta\tilde{\phi}(f) &= \frac{(T_{\text{RM}} + L) \cdot (T_{\text{RM}} + L + SA^2)}{\eta P_{\text{in}} 8J_0 J_1 T_{\text{RM}} \cdot SA} \sqrt{4h\nu} \sqrt{2\eta P_{\text{out},+/-}} \sqrt{1 + \frac{1}{2} CBS_{\text{dp}}} \\
&= \frac{(T_{\text{RM}} + L)(T_{\text{RM}} + L + SA^2)}{\eta P_{\text{in}} 8J_0 J_1 T_{\text{RM}} \cdot SA} \sqrt{8h\nu} \sqrt{\eta P_{\text{in}} J_1^2 \frac{4T_{\text{RM}}(SA^2 + L_C)}{(L + T_{\text{RM}} + SA^2)^2}} \sqrt{1 + \frac{1}{2} CBS_{\text{dp}}}
\end{aligned} \tag{2.65}$$

We can cancel many of these terms, so

$$\begin{aligned}
\Delta\tilde{\phi}(f) &= \frac{T_{\text{RM}} + L}{\eta P_{\text{in}} 8J_0 T_{\text{RM}} \cdot SA} \sqrt{8h\nu} \sqrt{4\eta P_{\text{in}} T_{\text{RM}} (SA^2 + L_C)} \sqrt{1 + \frac{1}{2} CBS_{\text{dp}}} \\
&= \sqrt{\frac{2h\nu (T_{\text{RM}} + L)^2}{\eta P_{\text{in}} J_0^2 4T_{\text{RM}}}} \sqrt{1 + \frac{1}{2} CBS_{\text{dp}}} \sqrt{\frac{SA^2 + L_C}{SA^2}}.
\end{aligned}$$

The first term contains the input carrier power and the recycling gain, including losses, so we can express the minimum phase measurement in terms of the power at the beamsplitter.

$$\Delta\tilde{\phi}(f) = \sqrt{\frac{2h\nu}{\eta P_{0,BS}}} \sqrt{1 + \frac{1}{2}CSB_{dp}} \sqrt{1 + \frac{L_C}{SA^2}} \quad (2.66)$$

This is similar to the ideal expression, with a few differences. Cavity losses reduce the recycling gain, decreasing the power at the beamsplitter. Contrast losses add noise by allowing excess light power on the detector. The second term represents the additional noise from contrast loss for carrier power, and the third term represents additional noise from contrast loss for sideband power.

Nonstationary Shot Noise

There is an additional factor which contributes to the shot noise sensitivity which is due to the time dependence of the output intensity resulting from the modulation scheme [Schnupp '89, Niebauer, '91]. This "nonstationary shot noise" contribution can degrade the interferometer sensitivity, and increase the amplitude spectral density of the shot noise. For square wave modulation and demodulation, there is no impact on performance, however, the harmonic content of such a system makes it impractical to implement in a system with the fundamental frequency at 25MHz. For sine wave modulation/ demodulation, the nonstationary shot noise increases the shot noise limited sensitivity by a factor of

$$ns = \sqrt{\frac{3 + CSB_{dp}}{2 + CSB_{dp}}} \quad (2.67)$$

If we multiply the result of eqn. 2.66 by the nonstationary shot noise correction, we see that the shot noise limited sensitivity of the interferometer should be

$$\begin{aligned} \Delta\tilde{\phi}(f) &= \sqrt{\frac{2h\nu}{\eta P_{0,BS}}} \sqrt{1 + \frac{1}{2}CSB_{dp}} \sqrt{1 + \frac{L_C}{SA^2}} \sqrt{\frac{3 + CSB_{dp}}{2 + CSB_{dp}}} \\ &= \sqrt{\frac{h\nu}{\eta P_{0,BS}}} \sqrt{3 + CSB_{dp}} \sqrt{1 + \frac{L_C}{SA^2}} \end{aligned} \quad (2.68)$$

Clearly, the key to achieving good phase sensitivity is to maximize the carrier power at the beamsplitter, while minimizing the contrast losses, which appear in the terms involving L_C and CSB_{dp} , and represent excess light on the detector.

Chapter 3

Description of the Experiment

3.1 Configuration of the Interferometer

The Phase Noise Interferometer is a suspended¹, frontally-modulated, power-recycled Michelson interferometer. The Michelson interferometer's arms are different lengths; the asymmetry is required by the Schnupp modulation scheme used to measure the arm lengths. This is the same control scheme used by LIGO, for which this machine is a prototype. The basic optical configuration of the experiment is shown in figure 3.1.

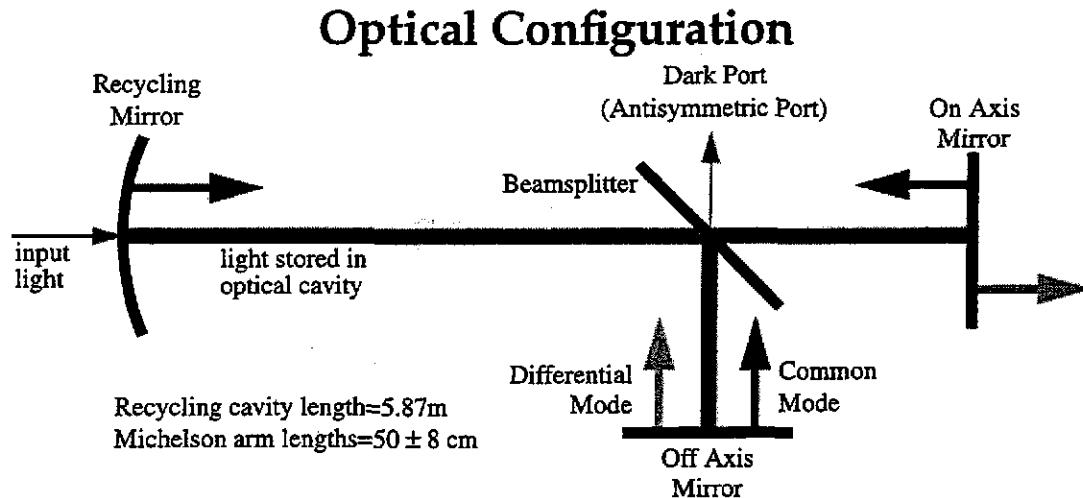


Figure 3.1: Optical Configuration of the Phase Noise Interferometer

The heart of the experiment is the Michelson interferometer shown on the right side of figure 3.1. The Michelson interferometer is sensitive to the differential-mode degree of freedom, the mode which will be excited by a passing gravitational wave. These passing waves generate differential phase shifts on the light in the two arms of the LIGO interferometer, as discussed in chapter 1. The Phase Noise Interferometer measures differential shifts with high precision, and our goals are to:

- 1) Make the instrument as sensitive to differential phase as possible;
- 2) Have the sensitivity limited only by the laser power on the beamsplitter; and
- 3) Demonstrate how LIGO can reach its phase sensitivity requirements.

1. The four optics which compose the interferometer, shown in figure 3.1, are suspended as pendula, as described in section 3.5.1.

Many things are required to allow us to reach these goals, but they can be broadly grouped into two categories: first, have enough power on the beamsplitter to reach the required sensitivity; second, eliminate other noise sources which corrupt the measurement.

Since we cannot buy 70Watt lasers which meet our requirements, we use power recycling to achieve high power on the beamsplitter. The Michelson interferometer is set to reflect nearly all of the carrier power back towards the laser source, so it can be thought of as a mirror. By adding a partially transmitting mirror between the laser and the Michelson interferometer, we make the Michelson interferometer into the back “mirror” of a Fabry-Perot cavity. This optical cavity allows us to increase the power incident on the beamsplitter by a factor of about 365, which is more aggressive than LIGO’s recycling. We use a 700mW laser (of which 211mW of carrier are incident on the interferometer) and a power recycling gain of 365, while LIGO will use a new 10W laser and a recycling gain of only 30. As we will see in chapter 4, Thermal Lensing, the high power we use causes thermal distortion of the optics, and ultimately limits the instrument’s performance.

Considerable effort went into eliminating other noise sources which corrupt the measurement. Careful design reduces the impact of these noise sources. In this chapter, we describe the design of the experiment, and discuss how the design impacts relevant noise sources. Other noise sources will be described in chapter 5, where the final spectrum is discussed.

Active control is employed throughout the instrument. These controls and readouts are shown schematically in figure 3.2. Within the interferometer, the differential length of the Michelson interferometer (differential mode) and the length of the recycling cavity (common mode) are controlled, and all six angular degrees of freedom are controlled (pitch and yaw for the differential mode, the common mode front mirror, and common mode rear mirror). The laser frequency is controlled, and several active systems are used to isolate the instrument from ground motion. Each of these systems are discussed in turn.

3.2 The Differential Mode and the Detection of Optical Phase

The differential length of the Michelson interferometer is measured with Schnupp modulation described in chapter 2. A 25.556MHz phase modulation is impressed on the input light to the interferometer. Interferometer misalignments convert the phase modula-

tion into amplitude modulation which is detected by RF photodiodes at the interferometer's dark port. For this technique, the Michelson interferometer's anti-symmetric port is held at a dark fringe, so that essentially none of the carrier power is transmitted to the detector; instead, it is reflected back towards the laser.

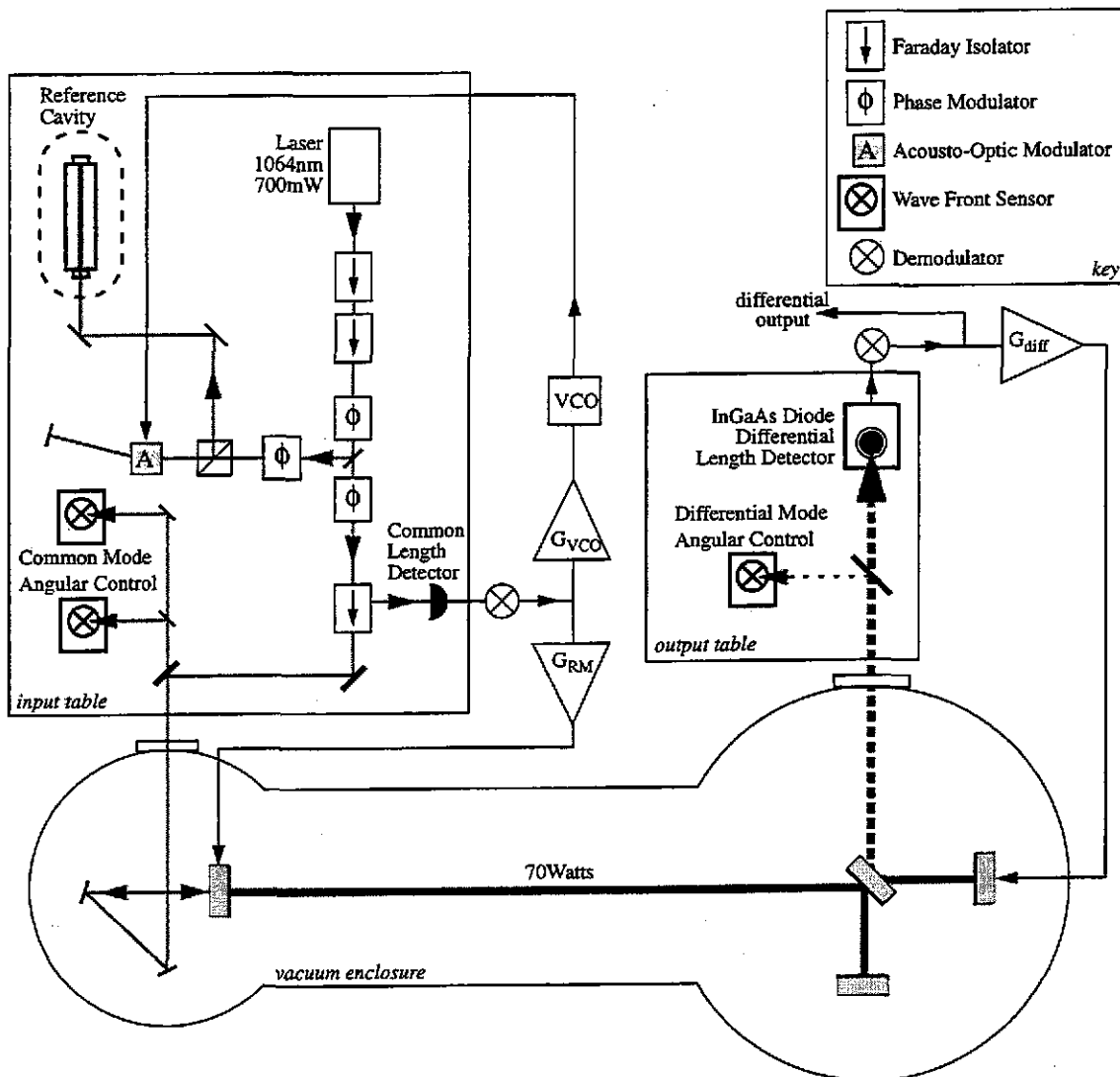


Figure 3.2: Overview of the experimental layout

The asymmetry makes the Michelson interferometer frequency selective, so although the anti-symmetric port is at the dark fringe for the carrier frequency, it is not at the dark fringe for the RF modulation sidebands. If the carrier begins to slip away from the dark fringe, then the carrier light transmitted out of the dark port begins to beat against the phase modulation sidebands, producing the RF amplitude modulation which we measure.

The amplitude modulation is measured with a 3mm EG&G InGaAs photodiode. A small bias voltage is applied to the photodiode to decrease its capacitance, and the diode is put in series with an inductor to form a resonant tank circuit tuned to the modulation frequency. A pair of RF traps at $2f_{\text{mod}}$ and $3f_{\text{mod}}$ were used to trap the harmonics, preventing the signal at $2f_{\text{mod}}$ from saturating the downstream electronics. The first active part in the detection chain is the RF preamplifier, an AC coupled Maxim 4107. The RF signal from the preamp is mixed with the local oscillator, yielding a baseband error signal proportional to the phase difference between the two Michelson interferometer arms. The error signal is used to generate the phase noise spectra shown in this work, and to control the differential arm lengths of the interferometer. The length error signal is processed by an analog control loop, and fed to electromagnets which actuate the position of one of the two Michelson arm mirrors. The open loop gain for this control loop is shown in figure 3.3.

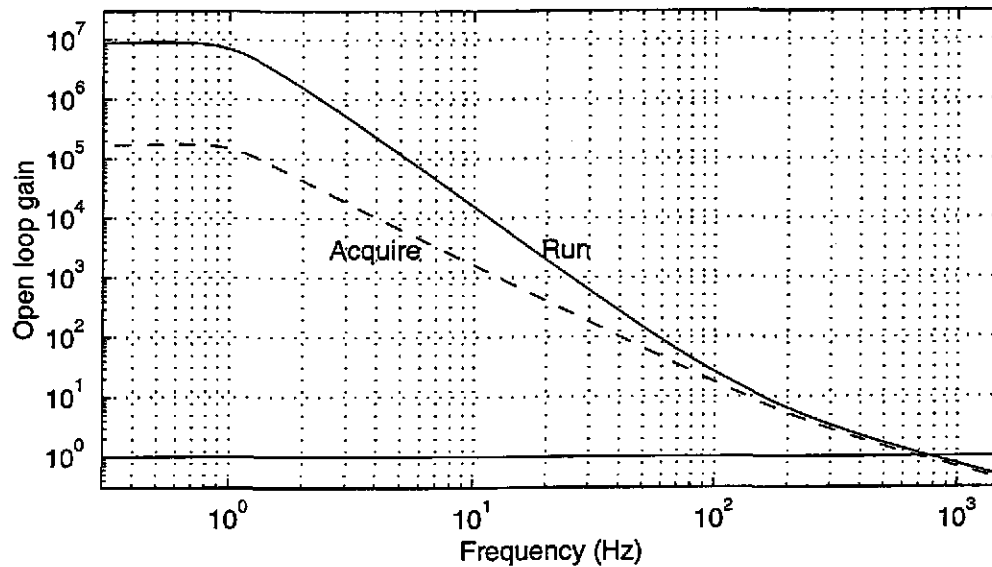


Figure 3.3: Open loop gain of differential Michelson interferometer control loop.

The dashed curve is the open loop gain of the differential length servo controller in the lock acquisition mode. Once lock is achieved, the controller is switched into the run mode, which has more gain at low frequencies, as shown by the solid curve.

The controller has two modes, the acquire mode, which is used to lock the interferometer, and the run mode, which is used to make measurements after the machine is locked. The acquire mode is unconditionally stable, and remains out of saturation much longer than the run mode. The additional gain in the run mode holds the interferometer closer to the optimal working point, reducing the influence of “bilinear” noise terms which couple

wavelength reference. The cavity discriminates between the carrier and the sideband frequencies, and the laser frequency is controlled so that the carrier resonates in the optical cavity, while the phase modulation sidebands are reflected from the front of the cavity. As the laser frequency moves off resonance from the optical cavity, the phase shift between the carrier and sidebands changes. This generates an amplitude modulated signal on the laser frequency, and the phase of the signal is determined by the direction of the laser frequency drift. The amplitude modulation of the light reflected from the cavity is measured with a fast photodiode.

The signal from the photodiode is demodulated, and the resulting signal is proportional to the difference between the round trip cavity length and an integral number of wavelengths of the carrier. This error signal is used to adjust the laser frequency along three feedback paths: a slow thermal control which changes the laser frequency by heating the laser crystal, a piezo-electric crystal which changes the laser frequency by squeezing the laser crystal, and an external phase correction Pockels-cell for high frequency feedback. A schematic view of the Prestabilized Laser is shown in figure 3.4.

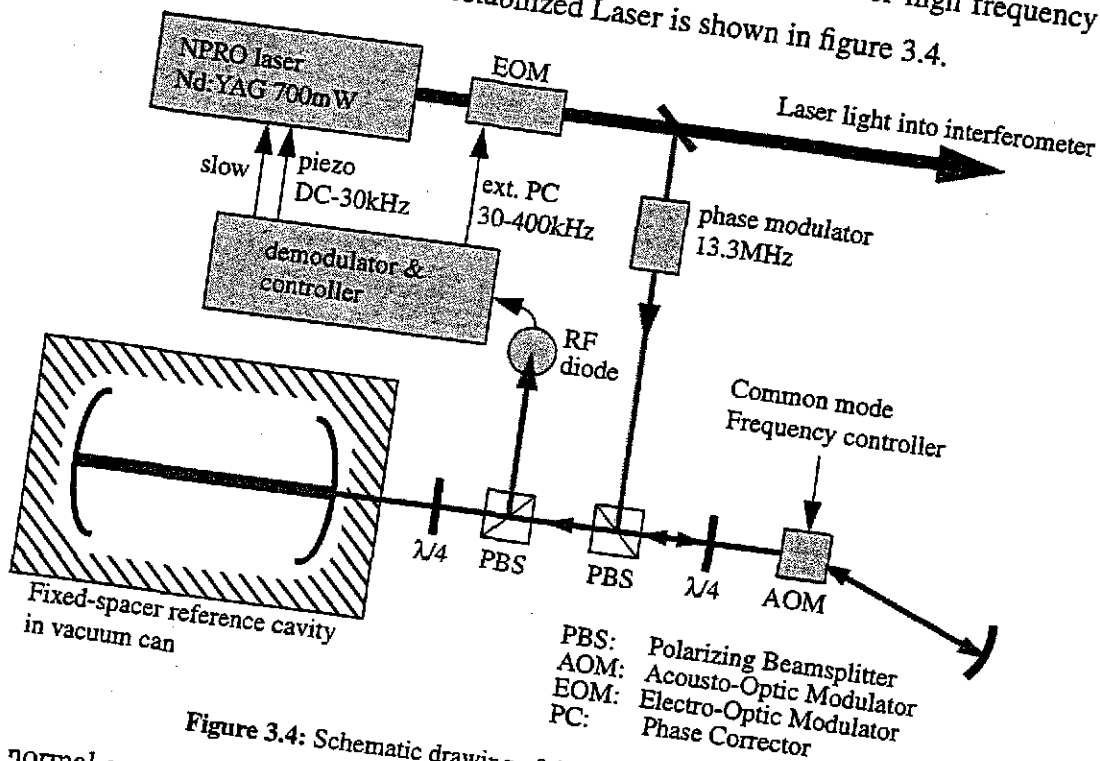


Figure 3.4: Schematic drawing of the Prestabilized Laser.

normal operation, the thermal controller was adjusted by the operator and was used in the PZT loop, and was not under active feedback control. The majority of

through length offsets (such as laser intensity fluctuations). The resulting spectra are discussed at length in chapter 5.

3.3 The Common Mode and the Importance of Frequency Noise

In this experiment, the control of the common mode cavity length and the control of the laser frequency were very closely related. This control had a high priority, since laser frequency noise was the limiting noise source below 1kHz in our previous attempt to demonstrate phase sensitivity.

3.3.1 Coupling of Frequency Noise into Phase Noise

Frequency noise on the input light couples directly into phase noise at the beamsplitter through the asymmetry of the Michelson interferometer arm lengths. The differential phase of the Michelson interferometer is:

$$\phi = \frac{2\pi \cdot 2(l_2 - l_1)}{\lambda} = \frac{4\pi \cdot \Delta l \cdot f}{c} \quad (3.1)$$

A macroscopic path length difference Δl implies a sensitivity to laser frequency of

$$\frac{d\phi}{df} = \frac{4\pi \cdot \Delta l}{c} \quad (3.2)$$

which means a frequency noise on the input light of $df = 1.8 \times 10^{-2} \text{ Hz}/\sqrt{\text{Hz}}$ results in a phase noise of

$$d\phi = \frac{4\pi \cdot \Delta l}{c} \cdot df = 1.2 \times 10^{-10} \frac{\text{rad}}{\sqrt{\text{Hz}}} \quad (3.3)$$

our measured noise floor. Frequency noise adds in quadrature to shot noise, so to limit the frequency noise to 5% of the total noise floor at $1.2 \times 10^{-10} \text{ rad}/\sqrt{\text{Hz}}$ requires a frequency noise of $df = 4 \times 10^{-3} \text{ Hz}/\sqrt{\text{Hz}}$.

A two-stage control system was used to suppress the frequency noise to this level.

3.3.2 The Prestabilized Laser

The first stage of laser frequency control is accomplished with the Prestabilized Laser system (PSL). A 21mW beam is taken from the main beam going to the interferometer, phase modulated at 13.3MHz, and reflection-locked to a fixed-spacer reference cavity suspended in a small vacuum enclosure mounted on the input optics table. Reflection locking (Pall locking) [Drever '83] uses a high finesse optical cavity as a laser

$$\begin{aligned}
P_{\text{mod}} &= \eta P_{\text{in}} [e^{i\omega_m t} (\overline{t_0 J_0 t_+ J_1} - \overline{t_0 J_0 t_- J_1}) + e^{-i\omega_m t} (\overline{t_0 J_0 t_+ J_1} - \overline{t_0 J_0 t_- J_1})] \\
&= \frac{\eta P_{\text{in}} 8 J_0 J_1 T_{\text{RM}} \cdot SA}{(T_{\text{RM}} + L) \cdot (T_{\text{RM}} + L + SA^2)} \cdot k_0 \delta \cdot [e^{i\omega_m t} (e^{-i\psi} + e^{-i\psi}) + e^{-i\omega_m t} (e^{i\psi} + e^{i\psi})] \quad (2.32) \\
&= \frac{\eta P_{\text{in}} 8 J_0 J_1 T_{\text{RM}} \cdot SA}{(T_{\text{RM}} + L) \cdot (T_{\text{RM}} + L + SA^2)} \cdot 4 k_0 \delta \cdot \cos(\omega_m t - \psi).
\end{aligned}$$

We can rewrite this cumbersome expression in a more tractable form. First, we note that the phase difference between the light returning from the two arms to the beamsplitter is $\phi = 4k_0\delta$ because of the way the asymmetry is defined in figure 2.2 and equation 2.5. We replace the terms describing mirror transmission and loss with the recycling gain, RG , and the carrier to sideband ratio at the beamsplitter, CSB_{BS} , and see that the detected power at the dark port at frequency ω_m is

$$P_{\text{mod}} = \eta P_{\text{in,carrier}} \cdot RG \cdot 2 \sqrt{CSB_{\text{BS}}} \sin(2k_{\text{SB}} A) \cdot \phi. \quad (2.33)$$

Thus, we see that the demodulated signal is proportional to the power at the beamsplitter and the phase offset between the two arms.

2.3 Useful Expressions

Here we develop a few other useful expressions.

Recycling gain: The recycling gain is the ratio of the stored power to the incident power when the cavity is at resonance. [See, for example, Fritschel '91.]

$$RG = \frac{\text{Circulating power}}{\text{Incident power}} = \left(\frac{t_{\text{RM}}}{1 - r_{\text{RM}} \cdot r_{\text{MM}}(k)} \right)^2 \quad (2.34)$$

For the carrier, this is

$$RG_0 = \frac{4T_{\text{RM}}}{(L + T_{\text{RM}})^2}. \quad (2.35)$$

$L + T_{\text{RM}}$ represents the total round trip power loss for light in the cavity. The recycling gain for the sidebands is smaller, because the sidebands experience the additional asymmetry loss at the Michelson interferometer. The recycling gain of the sidebands is

$$RG_{+,-} = \frac{4T_{\text{RM}}}{(L + T_{\text{RM}} + SA^2)^2}. \quad (2.36)$$

the frequency actuation was done by the PZT on the laser head. The PZT response is flat up to 150 kHz, and so the high frequency feedback path is an external phase correction Pockels-cell which is the dominant feedback path from 30kHz to 400kHz.

The open loop gain of the servo loops is shown in figure 3.5. The crossover point between the PZT loop and the external Pockels-cell loop is at 30kHz, and the unity gain point of the entire system is 400kHz.

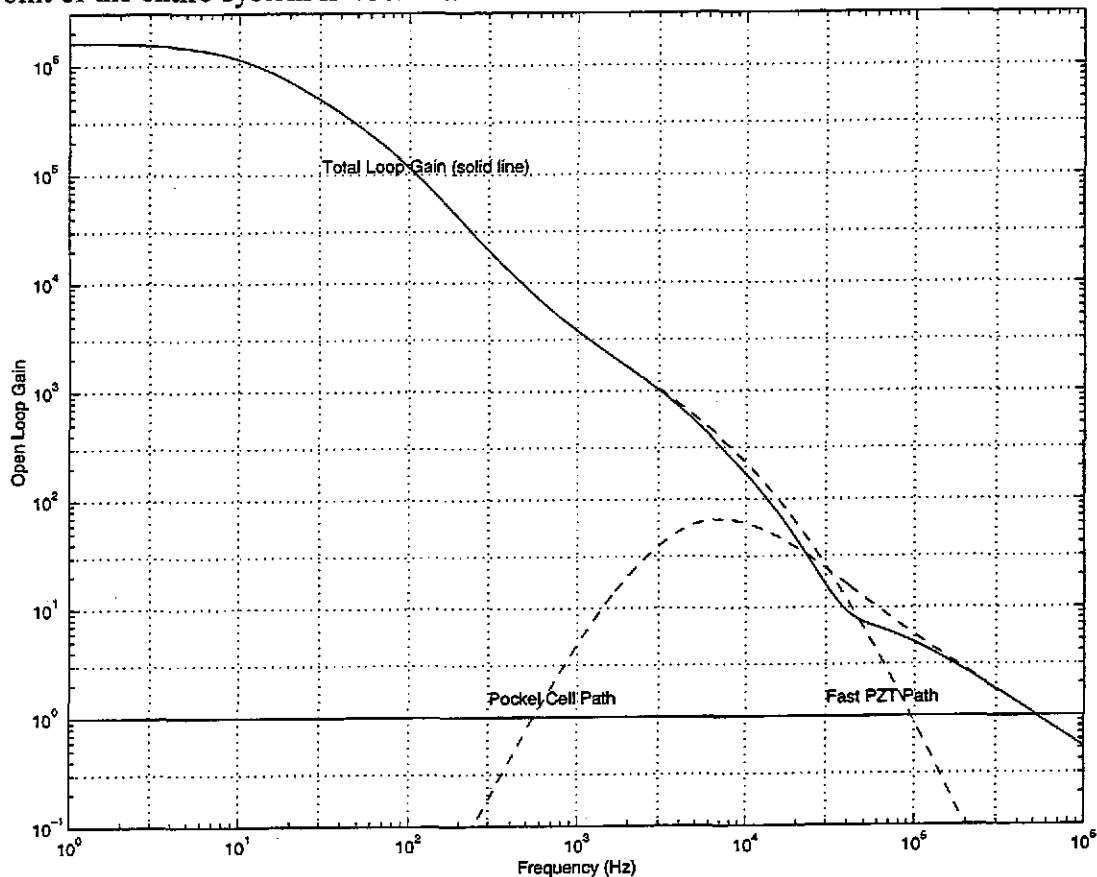


Figure 3.5: Open loop gain of the Prestabilized Laser

The acousto-optic modulator (AOM) shown in figure 3.4 is an external input to the Prestabilized Laser servo system. The AOM is driven by a voltage controlled oscillator (VCO) and is used as a double-pass frequency shifter. This input is used by the second stage of the frequency control system, discussed in section 3.3.3.

Figure 3.6 shows the frequency noise of the laser light under the control of the Prestabilized Laser control loop. This noise is measured with a suspended cavity, consisting of the on-axis Michelson mirror and the power recycling mirror. The $20\text{mHz}/\sqrt{\text{Hz}}$ noise

floor of the Prestabilized Laser from 2kHz to 20kHz is set by the noise in the VCO which controls the acousto-optic modulator.

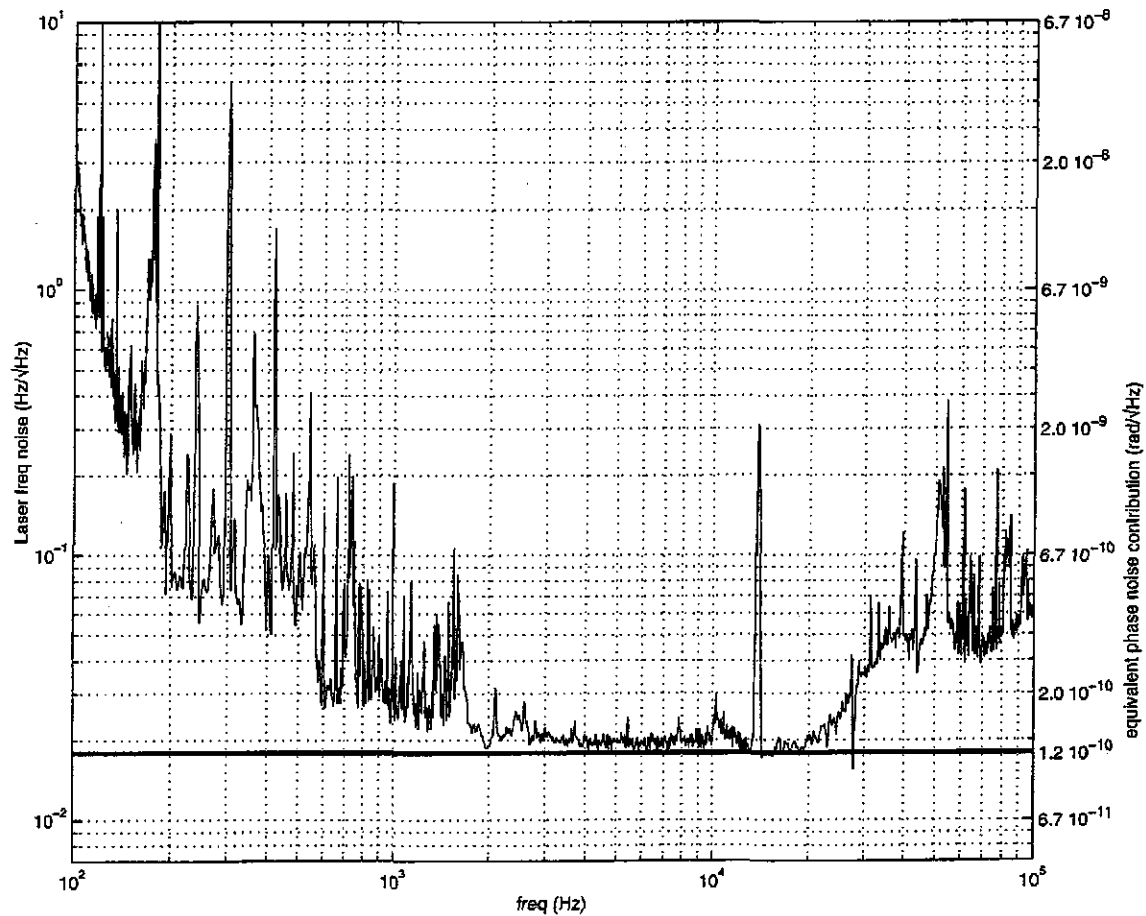


Figure 3.6: Frequency Noise of the Prestabilized Laser

The equivalent phase noise is the frequency noise of light in the cavity times the Michelson asymmetry factor of $6.7 \cdot 10^{-9}$ radians/Hz. The solid line is the point at which the frequency noise contributes the same level of noise as the shot noise. The suspended cavity acts as a low-pass filter for the frequency noise, with a single pole at 13kHz. This figure shows the frequency noise of light incident on the cavity. The effect of the cavity pole is not considered in the equivalent phase noise conversion for this figure, so the impact of frequency noise on phase noise above 13kHz is overstated by this figure.

3.3.3 Cavity Common Mode Control, the Second Stage of Frequency Control

The frequency noise of the Prestabilized Laser shown in figure 3.6 is too large to achieve the level of phase sensitivity needed for this experiment, so a second stage of frequency stabilization is used.

The second stage compares the on resonance length of the power recycling cavity with the laser frequency. This is important for two different reasons. First, the power recycling cavity must be on resonance to achieve power buildup within the cavity. Second,

above 15Hz, the length of the power recycling cavity of the suspended interferometer is the frequency reference for the second stage of laser frequency noise suppression. The power recycling cavity length is 5.87m, and the recycling mirror and the Michelson mirrors are supported on different tables, as shown in figure 3.7. This makes the cavity length susceptible to seismic disturbances at and below the isolation stack resonance frequencies. However, at frequencies above a few tens of Hertz, the suspended mirrors have excellent seismic isolation, and the cavity provides an exceptionally stable frequency reference. Section 3.5 provides a more detailed discussion of the seismic and acoustic isolation of the suspended interferometer.

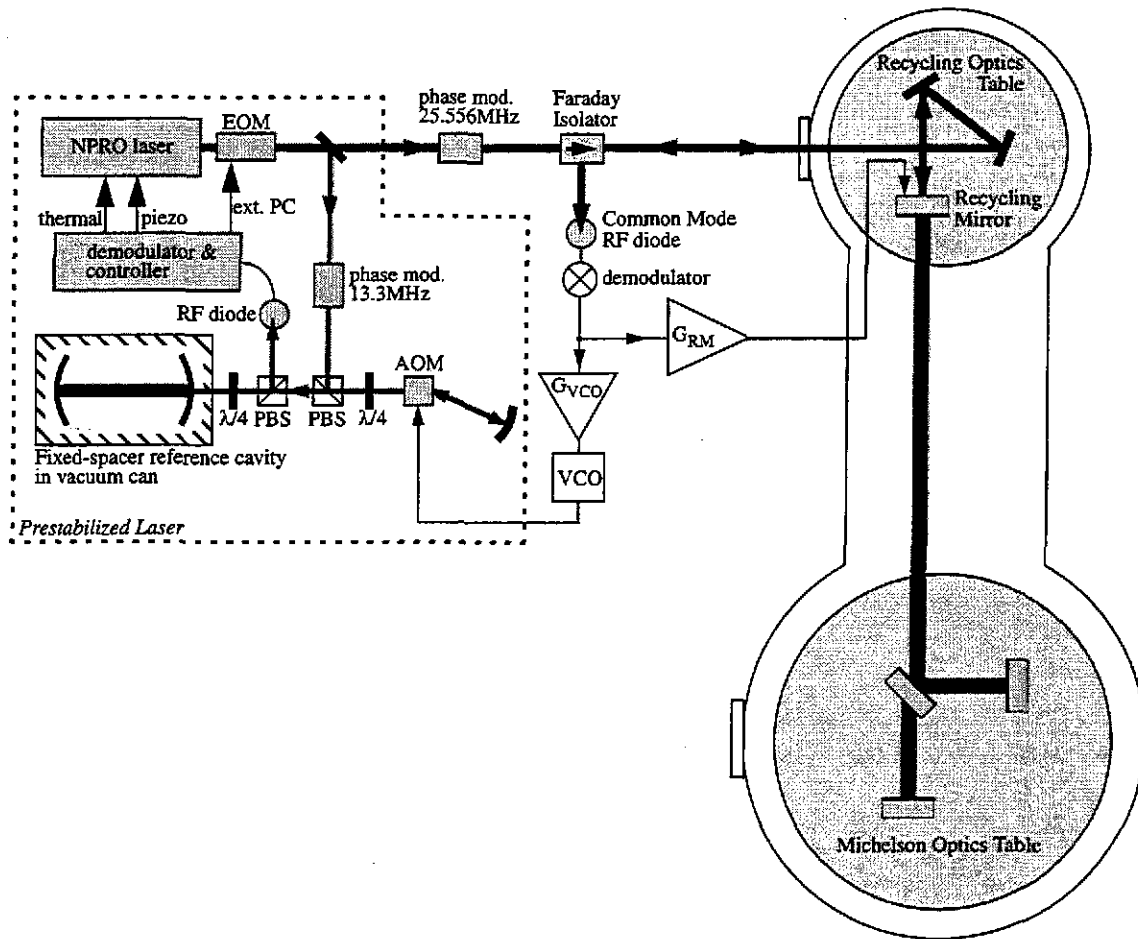


Figure 3.7: Common Mode Servo Control

The frequency dependence of the power recycling cavity stability necessitates a control system with two different feedback paths. Below 15Hz, the common mode length servo pushes the recycling mirror, using the fixed-spacer reference cavity as a length reference for the recycling cavity. Above 15Hz, the common mode servo controls the frequency

of the light from the Prestabilized Laser. The laser frequency is adjusted with a special input in the PSL loop. This input is an Acousto-optic modulator (AOM) between the phase modulator and the reference cavity as shown in figure 3.7. The AOM is controlled by a Voltage Controlled Oscillator (VCO), and is centered at 80MHz. The AOM is used as a frequency shifter. The first diffracted beam is reflected by a mirror whose center of curvature is set to the middle of the AOM, and the light is double-passed through the modulator. By placing the modulator at the center of curvature of the mirror, we can shift the AOM frequency without changing the angle of the double-passed beam. Changing the frequency of the AOM introduces a new frequency offset between the laser and the fixed-spacer reference cavity, which the Prestabilized Laser servo removes by changing the laser frequency, using the power recycling cavity length as a reference for the laser frequency. Since the frequency difference can be changed with the VCO, one can control the frequency of the light going to the interferometer without pulling the fixed-spacer reference cavity away from the center of its control range, holding both the reference cavity and the recycling cavity on resonance simultaneously. One sees that the second stage of frequency noise suppression is limited to regions where the open loop gain of the Prestabilized Laser is large. In practice, the additional phase shift which the Prestabilized Laser loop introduced near its unity gain frequency limited the second stage bandwidth to 100kHz.

The crossover point between the two feedback paths in the common mode servo was chosen to allow a large separation in the open loop gains of the two paths at 150Hz. This is necessary because, in a servo system with two feedback paths, the gain in one feedback path affects the performance of the other path.

Using the system shown in figure 3.8, a simplified view of the second stage frequency noise/ common mode length control loop, we can calculate the transfer function from input frequency noise, f , to residual frequency noise, r . The open loop gain of the laser frequency control path is $G_F = D \cdot F$, and the open loop gain of the power-recycling length control path as $G_L = D \cdot L \cdot s$. The transfer function becomes

$$\frac{r}{f} = \frac{1 + G_L}{1 + G_F + G_L} \quad (3.4)$$

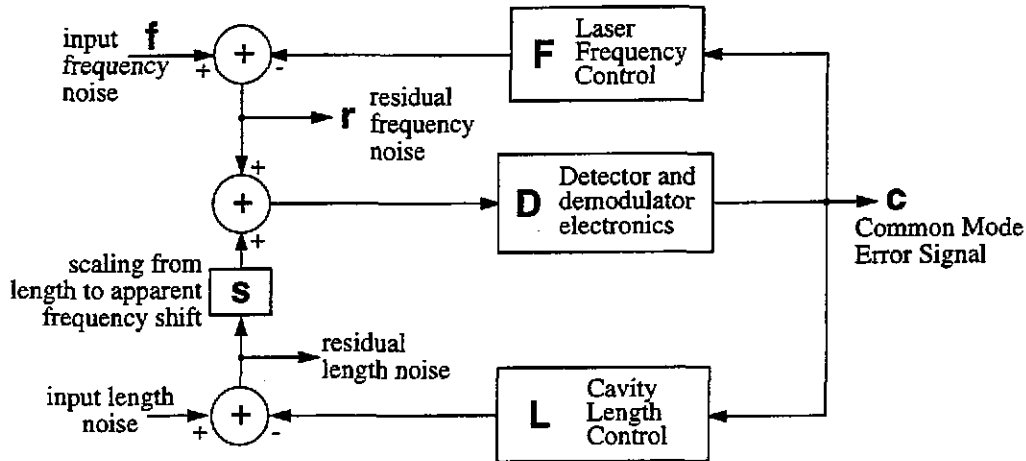


Figure 3.8: Servo Paths for Common Mode Servo

The open loop gain of the system is $G_F + G_L$, so the frequency noise suppression is reduced by the cavity length control path. In regimes where $G_F \gg G_L \gg 1$, the frequency noise is suppressed by approximately G_F/G_L , instead of the factor G_F we would expect for a single feedback path. To achieve good suppression of frequency noise, it is important to roll off the gain of the power recycling length loop as rapidly as possible.

The open loop gain of the second stage is shown below in figure 3.9. There are several interesting features of the common mode loop control path evident in figure 3.9. The low frequency gain of the loop is large in order to hold the cavity length constant against the low frequency drift of the Stacis active seismic isolation feet. The feet exhibit a motion of about $10\mu\text{m}$ peak-to-peak at frequencies around 0.1Hz. These controllers are discussed in more detail in section 3.5. The next feature of interest is the 2.5Hz notch in the frequency control path. This notch was added to help reduce the dynamic range requirements of the frequency control path resulting from the large motions of the optics at 2.5Hz, the frequency of the first stack resonance. At this frequency, stack motion still couples reasonably well to motion of the suspended optics, since the pendulum isolation is only $(1\text{Hz}/2.5\text{Hz})^2 = 0.16$. Furthermore, the proximity to the 18Hz crossover frequency of the two feedback paths constrains the relative phase of the two loops near this frequency, so a notch with a Q of 1 at the input to the frequency control electronics was a reasonable solution, since it reduces the phase margin at the crossover frequency by only 8 degrees.

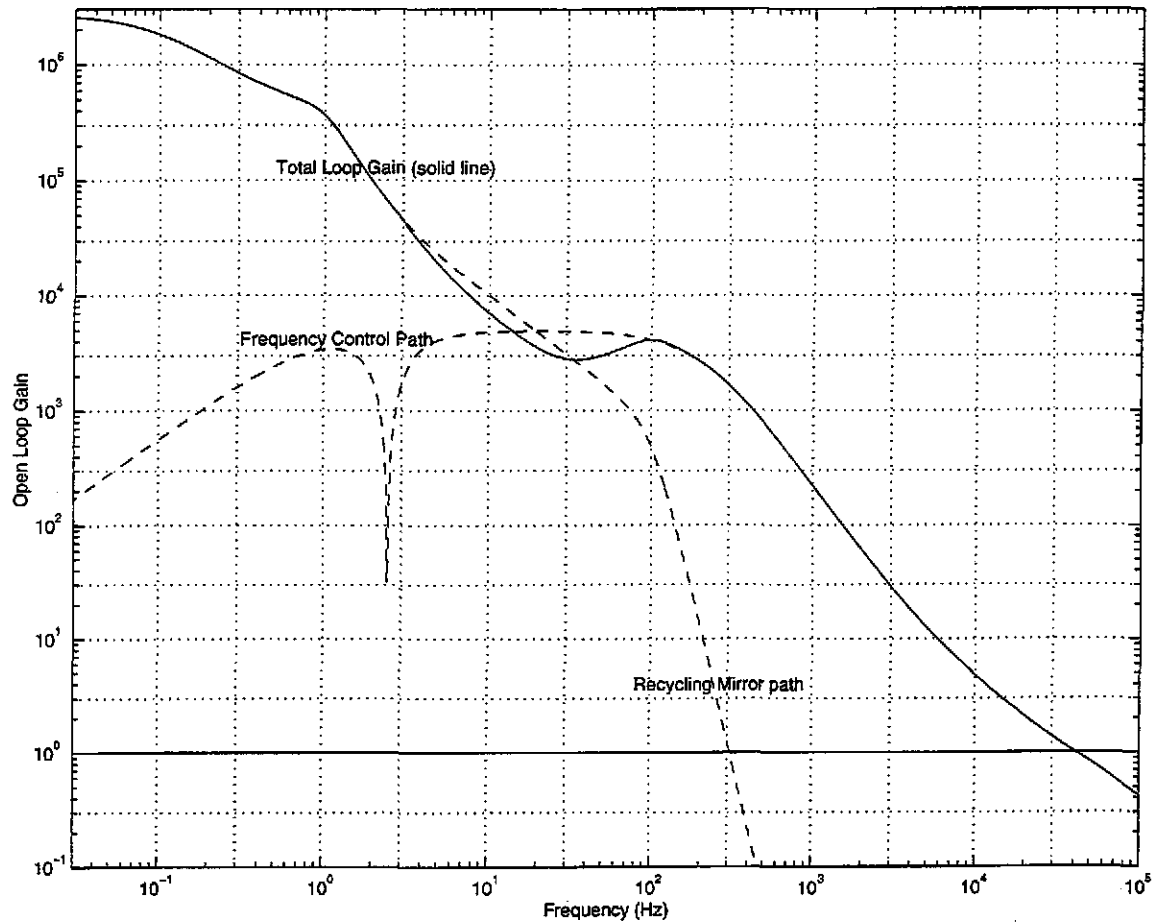


Figure 3.9: Open Loop Gain of the second stage of Frequency Control

After the two feedback paths cross at 18Hz, it is important to get as much relative gain between the feedback paths as possible before the unity gain frequency of the loop is reached at about 100kHz. The factor which ultimately limits the bandwidth of the common mode loop is the 1.14 μ sec time delay of the Acousto-optic modulator, which adds 41 degrees of phase shift at 100kHz. A fourth-order 100Hz lowpass Butterworth filter is used to rapidly attenuate the gain of the recycling mirror feedback path. More radical filters were found to be unnecessary. The predicted common mode loop suppression of frequency noise is shown in figure 3.10. This figure shows the closed loop gain from point **f** (input frequency noise) to point **r** (residual frequency noise) in figure 3.8.

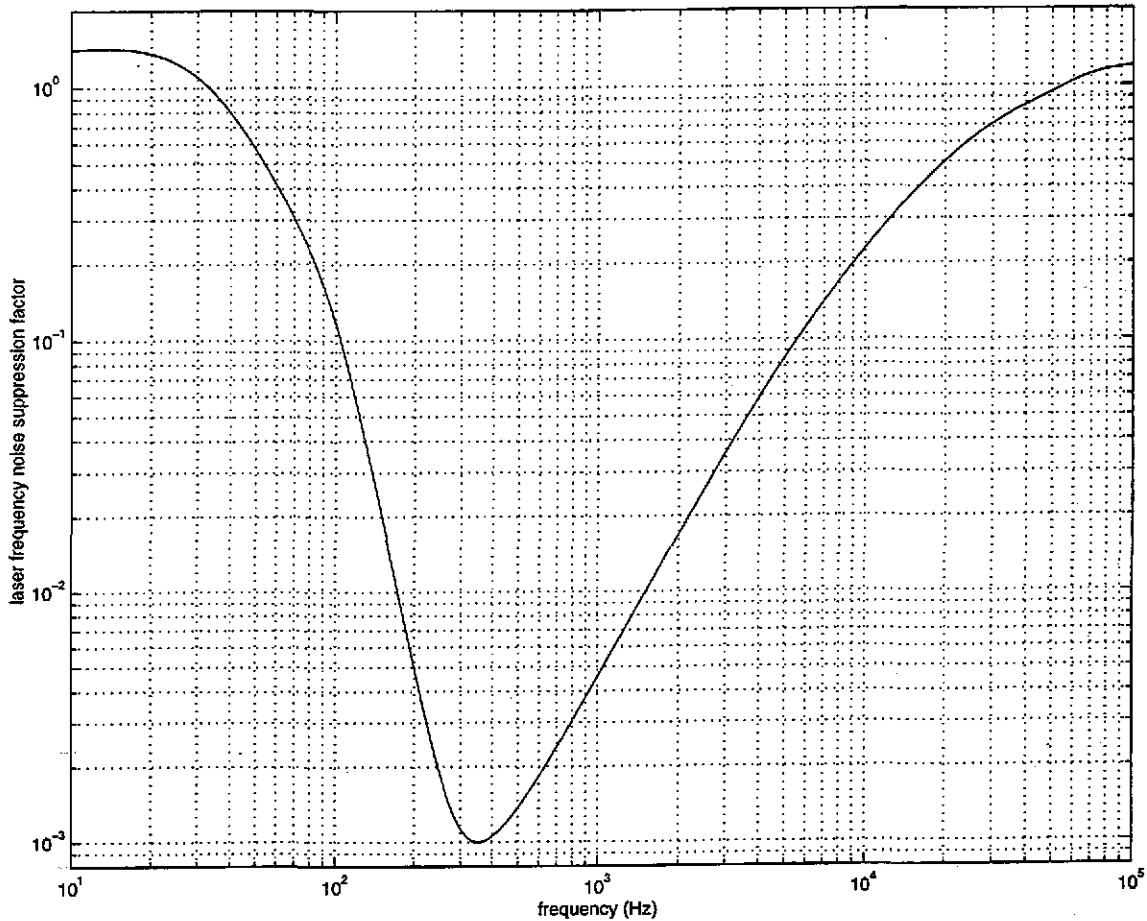


Figure 3.10: Suppression of Frequency Noise by the Common Mode Loop

The residual frequency noise of the laser light in the power recycling cavity after adding the second stage to the frequency control loop is shown in figure 3.11. This figure presumes to show the residual frequency noise at point **r** in the common mode servo shown in figure 3.8. Figure 3.11 actually shows the error signal of the common mode loop (point **c** in figure 3.8), converted to units of frequency noise with the calibration peak at 2kHz, and corrected by the gain in the recycling mirror path.

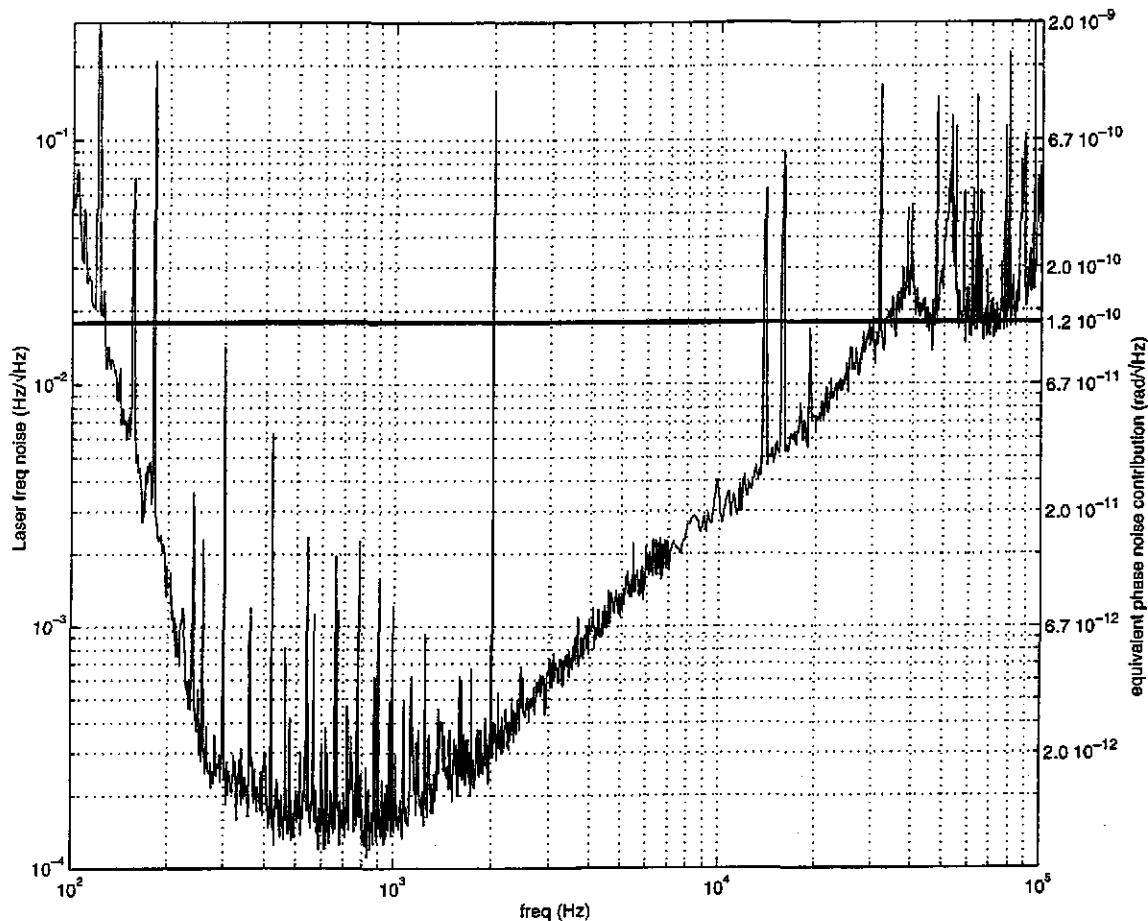


Figure 3.11: Frequency Noise of Laser Light in the Power Recycling Cavity

This is an in-loop measurement of the residual frequency noise of the second stage of laser frequency control. The solid line at $1.8 \times 10^{-2} \text{ Hz}/\sqrt{\text{Hz}}$ is the level of frequency noise required to result in a noise contribution equal to the photon shot noise we measured. The peak at 2kHz is a calibration peak. The two peaks around 15kHz are from video monitors.

3.4 Wavefront Sensing and Control of the Suspended Interferometer

We believe this is the first suspended power-recycled Michelson interferometer with “wavefront sensing” and control of all six independent angular degrees of freedom. Wavefront sensing was first described by Anderson [Anderson '84] and has been demonstrated on a several experiments [Sampas '90, Morrison I '94, Mavalvala '97]. The sensors used in this experiment were developed by Dr. Daniel Sigg and Dr. Nergis Mavalvala for Dr. Mavalvala's thesis work in our laboratory [Mavalvala '97], and are scheduled for deployment in the LIGO interferometers. The Argon-Ion version of the Phase Noise Interferometer used a single wavefront sensor to control the differential mode alignment, which is critical to achieving a high, stable recycling gain.

The wavefront sensing scheme used in this experiment uses the demodulated signal from an RF quadrant diode (aligned as shown in figure 3.12) to detect phase gradients between the carrier and RF sidebands across the beam at some point in an interferometer. These spatial phase gradients give information about the angular misalignments of optical cavities. The production of spatial RF phase gradients is related to the production of the average RF phase offset generated by length changes in the cavity, except that the quadrant diodes allow measurement of the RF amplitude modulation generated by the interference of the TEM_{00} mode of the carrier with the TEM_{01} mode of the sideband (and vice-versa) generated by misalignments [Morrison II '94, Hefetz '97]. This enables the wavefront alignment scheme to use the same 25.556MHz frontal modulation sidebands as the length detection scheme. It also means that the differential mode angular detector is at the same interferometer port as the differential length detector, and the common mode angular detectors are at the same port as the common mode length detectors.

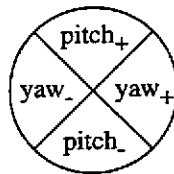


Figure 3.12: Alignment of quadrant diode for wavefront sensor measurement

For a perfectly aligned cavity, all the power is in the TEM_{00} mode. As the cavity becomes misaligned, power is converted into TEM_{01} or TEM_{10} modes of the aligned cavity basis. Since the TEM_{00} and TEM_{01} modes propagate with different Guoy phases, the power at the detector is proportional to the product of the TEM_{00} field, the TEM_{01} field generated by the misalignment, and the cosine of the Guoy phase between these modes at the detector location. For nondegenerate cavities, the Guoy phase propagation differential between the front and rear cavity optics makes it possible to position the detectors so that one can distinguish between the error signals generated at the front and at the rear of the cavity. We used lenses to construct “Guoy phase telescopes” before each of our common mode detectors so that one detector was sensitive only to recycling mirror misalignments, and the other was sensitive only to common mode Michelson mirror misalignments, which simplified the control problem to a set of parallel single-input single-output loops.

The two main requirements for the control loops were to provide enough gain at 2.5Hz to suppress the differential mode angular misalignments from the fundamental stack frequency to a few μ radians rms, while introducing less than 10^{-17} meters/ $\sqrt{\text{Hz}}$ of length displacement at 150Hz. Figure 3.13 shows the open loop gain of the differential alignment servo used to meet these requirements

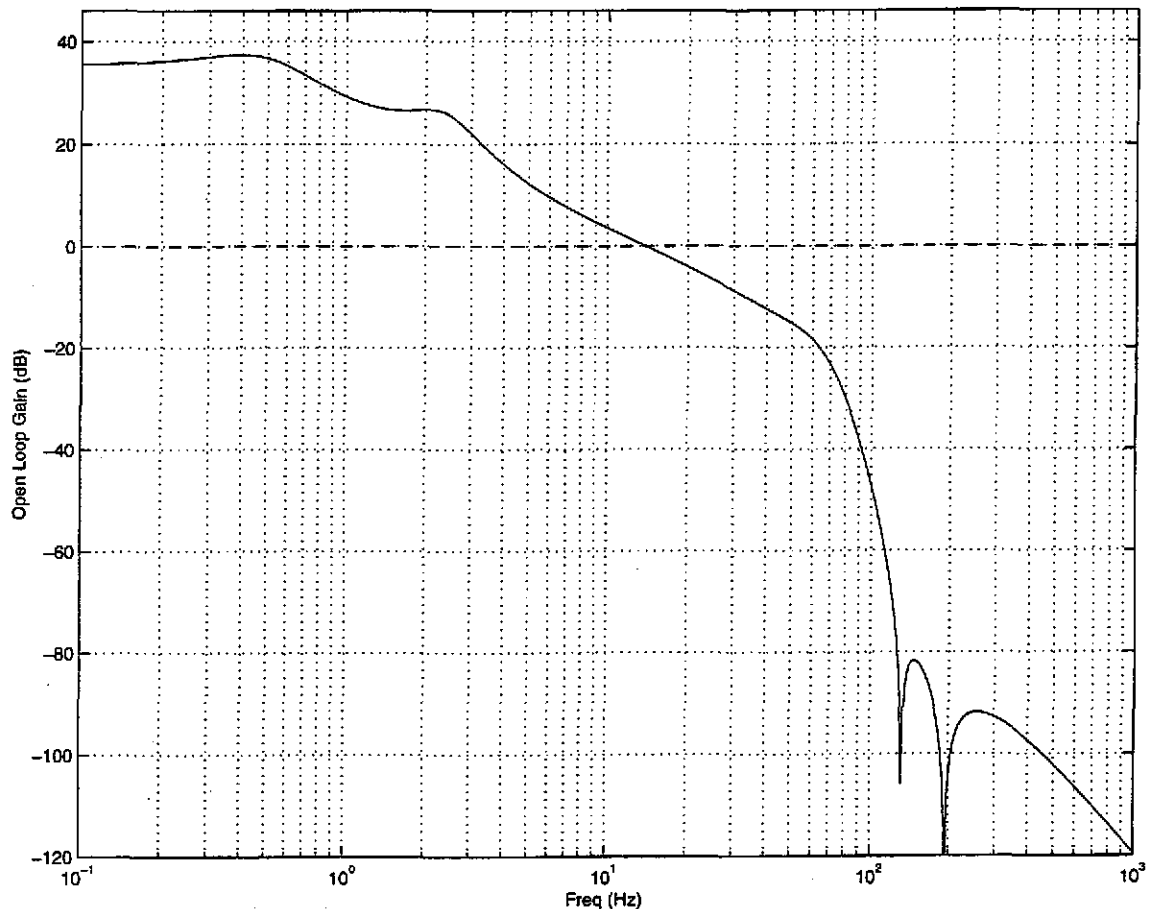


Figure 3.13: Open loop gain of the differential angular alignment servo

The rms misalignments were reduced to 4μ radians. The noise caused by angular motions is discussed in depth in section 5.4.3, Beam Jitter. To allow unconditionally stable operation of the angular control system, extra gain at 2.5Hz was provided by a resonant gain stage with a Q of 1.7, and out-of-band control actuation was reduced by a derated 5th order low-pass elliptic filter at 90Hz. The filter was derated by lowering the Q of the 90Hz pole pair, which reduces filter ringing at the expense of passband flatness and phase shift.

A detail of the open loop gain and phase near the unity gain frequency are shown below in figure 3.14.

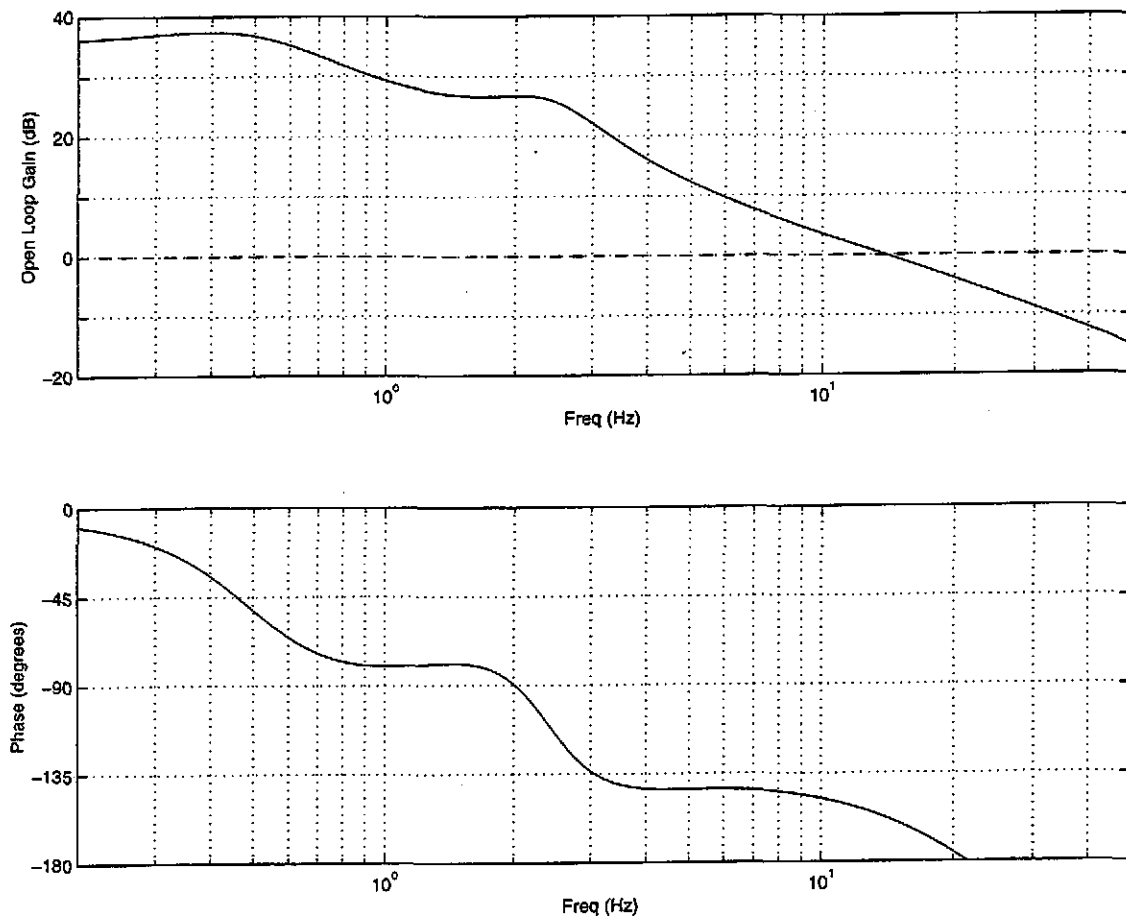


Figure 3.14: Detail of unity gain point for alignment control servo.

3.5 Environmental Isolation of the Interferometer Optics

“Do you know how often they detect gravity waves at MIT?”

“No, how often?”

“Every 15 minutes, until the Red Line quits running!”¹

Considerable effort was exerted to isolate the experiment from environmental noise. The four optics which comprise the interferometer were housed in a vacuum enclosure, and were supported by a three stage seismic isolation system. The input optics table was mounted on a seismic isolation platform, and the output table was mounted on a seismic isolation platform and surrounded by an anechoic enclosure.

1. Related to the author by a complete stranger in Harvard Square.

3.5.1 Interferometer Optics

The interferometer optics were isolated from environmental noise by enclosing them in a vacuum system and supporting them with a three stage seismic isolation system. The vacuum system was a 14 thousand liter system held at a nominal pressure of 6×10^{-7} torr with a 480 liter/sec. Perkin-Elmer Ion pump. As shown in figures 3.7 and 3.15, the vacuum system enclosed the entire interferometer. The vacuum envelope comprised two tanks, one holding the recycling mirror and its stack, the other holding the Michelson optics on their stack. The two tanks were joined by a 4.2 meter long, 70cm diameter tube.

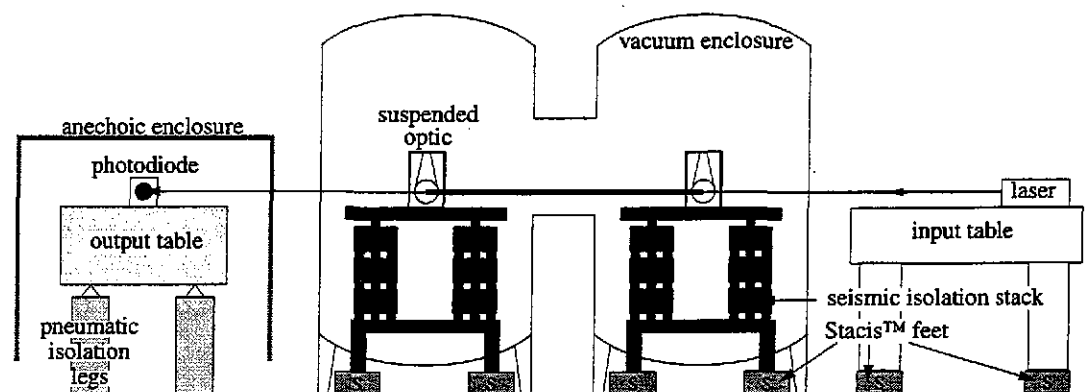


Figure 3.15: Environmental isolation of the experiment.

The experiment has several types of environmental isolation, including active seismic isolation of the input optics table, a three layer seismic isolation system of the interferometer optics, and seismic isolation of the output optics table. The interferometer is in a vacuum system to eliminate air pressure fluctuations and acoustic noise, and the output table is surrounded by an anechoic enclosure.

Each of the two tanks had a separate seismic isolation system. The bottom of each seismic isolation system consisted of a set of three Stacis 2000™ active isolators manufactured by Barry Controls Inc. Each foot supported one leg of a triangular platform within the tank. The platform in the vacuum system supported a three-leg four-layer passive isolation stack. The top layer of the stack is a large, aluminum optical table. Steering mirrors and beam blocks were attached directly to this table, while the interferometer optics had one additional isolation stage. The interferometer optics were each suspended by a single loop of wire from a small cage. The three Michelson optics were one the optical table in one tank, and the recycling mirror was on the table in the other tank.

The Stacis™ system is a set of three active seismic isolation stands made by Barry Controls. The controls for each foot are independent, and each foot controls three degrees of freedom, one vertical and two horizontal directions. To prevent the payload from being

overconstrained, the Stacis foot also includes a passive flexure between the active controller and the payload. Motion of the payload support point is monitored with geophones, and actively servoed away by actuating PZT stacks between the ground and the payload support point. The bandwidth of the system extends from about 1Hz to about 100Hz, with a maximum gain between 10 and 20Hz. The closed loop gain of the system supporting the Michelson optics is shown in figure 3.16.

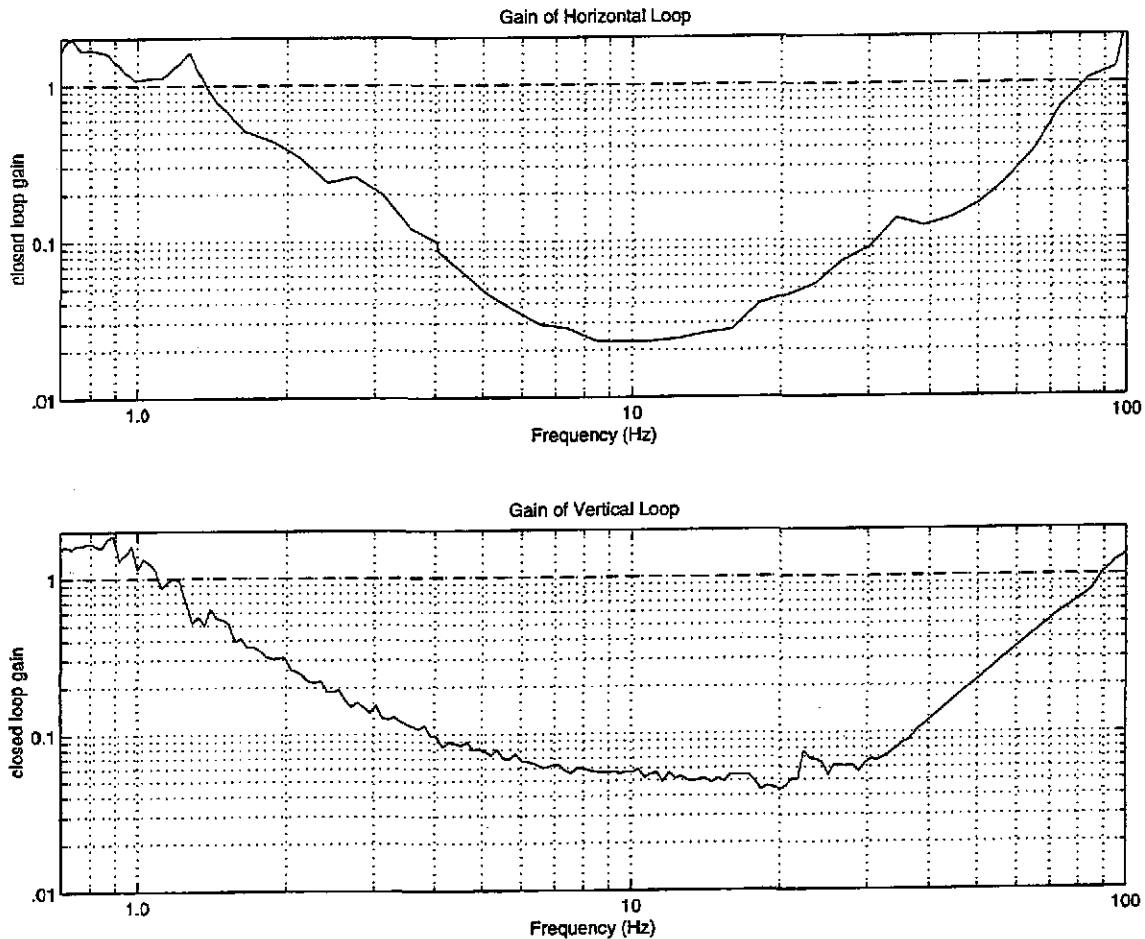


Figure 3.16: Closed loop gain for one foot of the Stacis™ system supporting the Michelson optics

The second stage of seismic isolation was the passive isolation stack which is similar to the LIGO stack and was designed to isolate the experiment from ground motion at frequencies higher than the mechanical resonance frequencies of the stack. The stack was within the vacuum system and sat on a triangular support platform. Each corner of the support platform was held by a leg which feeds through the vacuum enclosure with a flexible vacuum bellows, and rested on one of the Stacis™ feet. The vacuum bellows acted as a

soft spring which connected the leg to the vacuum enclosure, decoupling enclosure motion from leg motion, and allowing the considerable weight of the enclosure to be supported directly by the floor.

The stack was a four-layer three-leg design, as shown in figure 3.17. Each layer was essentially a mass-spring system, attenuating motion of the previous stage by $(f/f_{res})^2$ at frequencies above the resonant frequency of the mass-spring system.

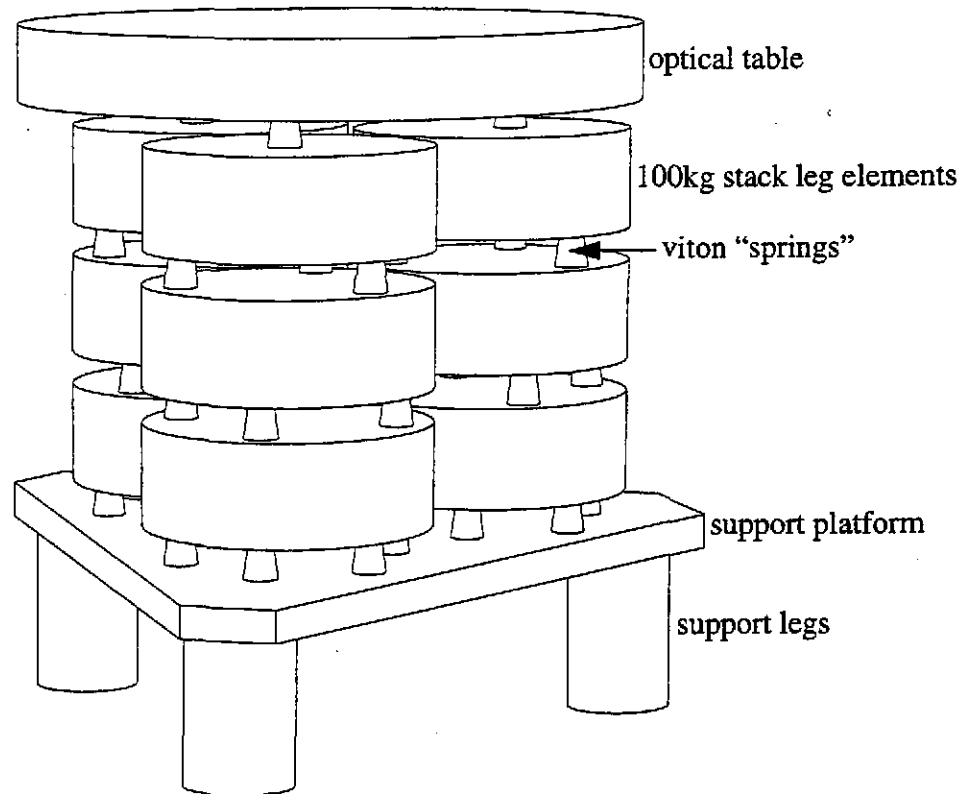


Figure 3.17: Seismic isolation stack

The dynamics of this type of stack have been calculated and measured by J. Giaime. [Giaime '95, Giaime '96]

The final layer of seismic isolation for the interferometer optics was the single-stage, single-loop pendulum suspensions, which are similar to the LIGO Small Optics Suspensions. The optic was hung as a pendulum bob in a single loop of wire, as shown in figure 3.18. The pendulum was about 30cm long, for a 1Hz pendulum mode, and the wire attachments were configured so the pitch and yaw frequencies were around 0.5Hz. Also shown in figure 3.18 are the permanent magnet-fin assemblies which were glued onto the optic so

that it can be controlled. The four assemblies on the back of each optic were used to control the interferometer length, as well as the pitch and yaw motion of the optic. The fifth assembly, which was mounted on the side of the optic, allowed damping of the side to side motion of the optic. The two remaining degrees of freedom were not controlled, but were merely set by the suspension wires. The “bounce” mode or vertical motion of the optic had a resonance at 19Hz as the optic stretches the steel suspension wires. The “roll” mode of the optic, (in which one end of the wire extends while the other contracts) is at 28Hz.

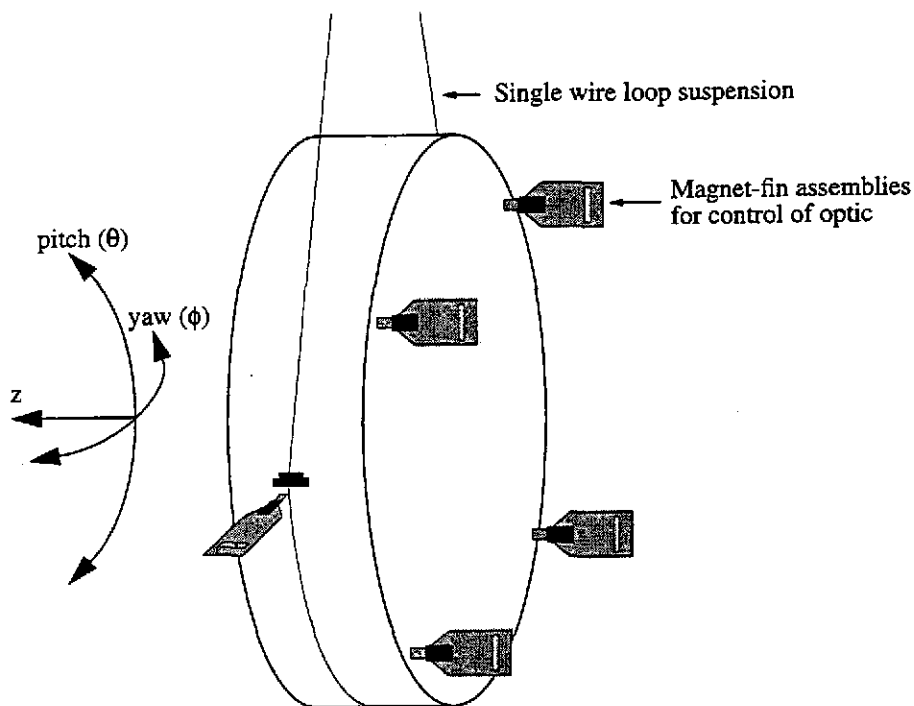


Figure 3.18: Optic suspended by a single loop of wire

The assemblies are composed of an aluminum standoff, a permanent magnet, and an aluminum fin. The standoff is glued onto the optic with vac-seal, a vacuum compatible epoxy. A small permanent magnet is glued to the other end of the standoff. The magnet is partially enclosed by the end of a thin aluminum fin (see figure 3.19). The fin has a small slit machined into it, which is used as part of an optical sensing system to determine the optic’s location. The aluminum standoff is used to reduce the coupling between internal thermal motion of the optic and the sintered magnet material, so as to minimize the impact of the lossy magnet material on the internal Q’s of the optical substrate [Gillespie II '95].

The entire structure has resonances at about 4kHz, which can be seen clearly in the phase noise spectrum (see section 5.3.1).

The optic hangs within a stainless steel “cage” which provides a suspension point for the wire, holders for the control sensors and actuators of the magnet-fin assemblies, and motion limit stops to protect the optic (“earthquake stops”).

The magnet-fin assemblies fit into OSEMs (Optical Sensor, Electromagnetic Motor), actuators which are mounted on the suspension cage (see figure 3.19). The OSEM provides two functions: it contains an optical sensor which locates the slit in the fin, and it has a coil electromagnet which can apply force to the optic via the permanent magnet.

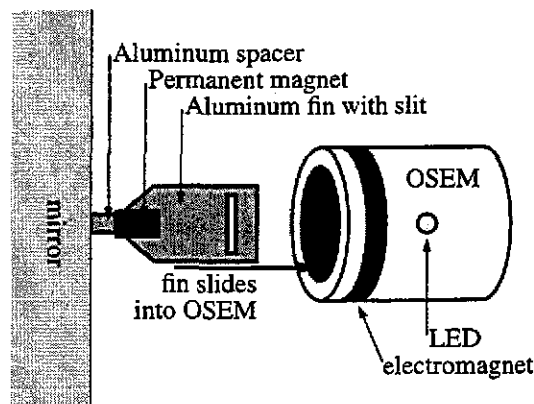


Figure 3.19: OSEM detail

A controller unit provides local control of each optic. The optical sensors provide information about the optic’s location, and a low frequency, AC coupled servo is used to damp out the pendulum resonances of the optic for side-to-side motion, \hat{z} motion (normal to the optical surface), pitch, and yaw. The controller also applies DC current to the coils for initial interferometer alignment.

The suspension wire is a 2 mil diameter steel wire. It is located on the optic by a pair of small rods as shown in figure 3.20. First, a glass “guide rod” is glued to the side of the optic. An aluminum “wire take-off rod” of a slightly large diameter is then placed below the guide rod. The wire take-off rod is set in the channel formed by the side of the optic and the guide rod and held in place by the tension of the wire. The wire is set into a very small groove around the wire take-off rod. The optic is then balanced by sliding the wire take-off rods back and forth. When the optic is within 2 milliradians of vertical, the wire take-off rods are glued in place by a small dot of epoxy on each end. The wire is not glued

to the optic. The optic can be removed entirely from the suspension wire and vacuum baked to remove residuals from the epoxy joints. The optic can then be re-hung from the wire by placing the wire back into the grooves in the wire take-off rods. After baking, the optics hung within about 5 milliradians of vertical.

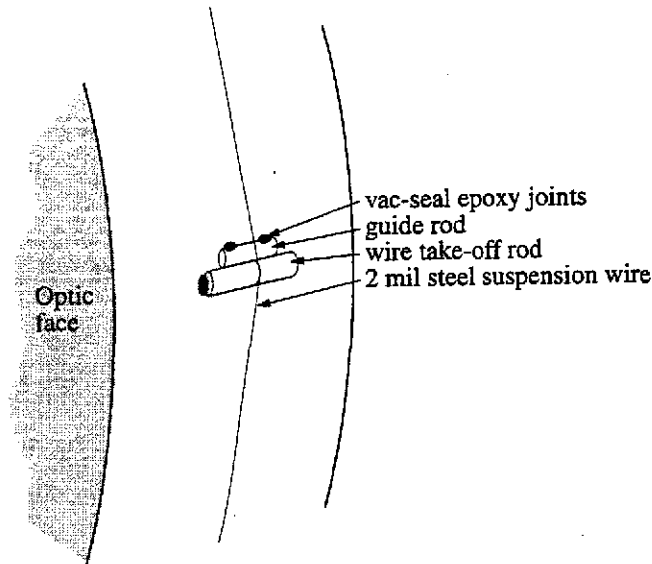


Figure 3.20: Suspension wire attachment detail

3.5.2 Parasitic Interferometry

One source of noise in interferometers is light which is removed from the main beam (by an imperfect anti-reflective coating, for example), sent along some path, and recombined with the main beam, introducing phase and amplitude noise as various parameters of the path change. In previous work, this “parasitic interferometry” between the recycling mirror and optics on the input optics table caused excess noise in the interferometer output, so steps were taken to reduce the impact of that noise path on this experiment. A second parasitic path, between the output optics and the Michelson beamsplitter, also caused noise and considerable effort went towards reducing the impact of that noise source as well.

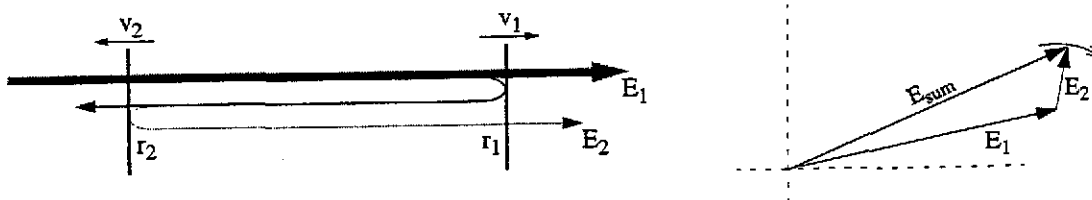


Figure 3.21: Electric fields of a parasitic interferometer

Parasitic interferometers result from unintended scattering of light into the measurement beam. Figure 3.21 shows a diagrammatic view of a typical parasitic path. An optic in the path of the main beam has a reflectivity, r_1 , which reflects or scatters light to a second optic, which in turn reflects or scatters light back into the fundamental mode of the main beam, with a field reflectivity r_2 . As the optics move with velocity v_1 and v_2 , the resultant output field, \vec{E}_{sum} , becomes:

$$\vec{E}_{\text{sum}} = \vec{E}_1 + \vec{E}_2 \approx \vec{E}_1 \left(1 + r_1 r_2 e^{\frac{2\pi i}{\lambda} \left[l_0 + \int 2(v_1 + v_2) dt \right]} \right). \quad (3.5)$$

where \vec{E}_2 is the additional field scattered back into the field of unperturbed beam, \vec{E}_1 , and l_0 is the initial extra propagation length of the scattered beam. The magnitude of the scattered light vector is often constant, but the relative phase of the scattered light with respect to the main beam changes with the path length. For large relative motions of the optics, with relative velocity v , the scattered field can move through many fringes, modulating the amplitude and frequency of the resulting beam around the frequency $2v/\lambda$ Hz. When the relative motions are less than a wavelength, the coupling is approximately linear. For small reflectivities, the peak to peak power modulation is approximately $4r_1 r_2$.

Parasitic Interferometry at the Input Table

Parasitic interferometry at the input to the main interferometer causes changes to the input field. These changes couple to the output of the Phase Noise Interferometer both as frequency noise (see section 3.3.3) and to a lesser extent as laser intensity noise (see section 5.4.4).

To control this, steps were taken to reduce the reflectivity of the scattering components and their relative velocity. The input optics table was supported on a set of three Stacis feet, and brewster-angle polarizers were used in the Faraday isolator (shown in figure 3.7) which separated the light reflected by the interferometer from the incident beam. The table was also enclosed in a small clean room enclosure, which reduced dust accumulation (a significant cause of back-scattered light) and damped the acoustic noise.

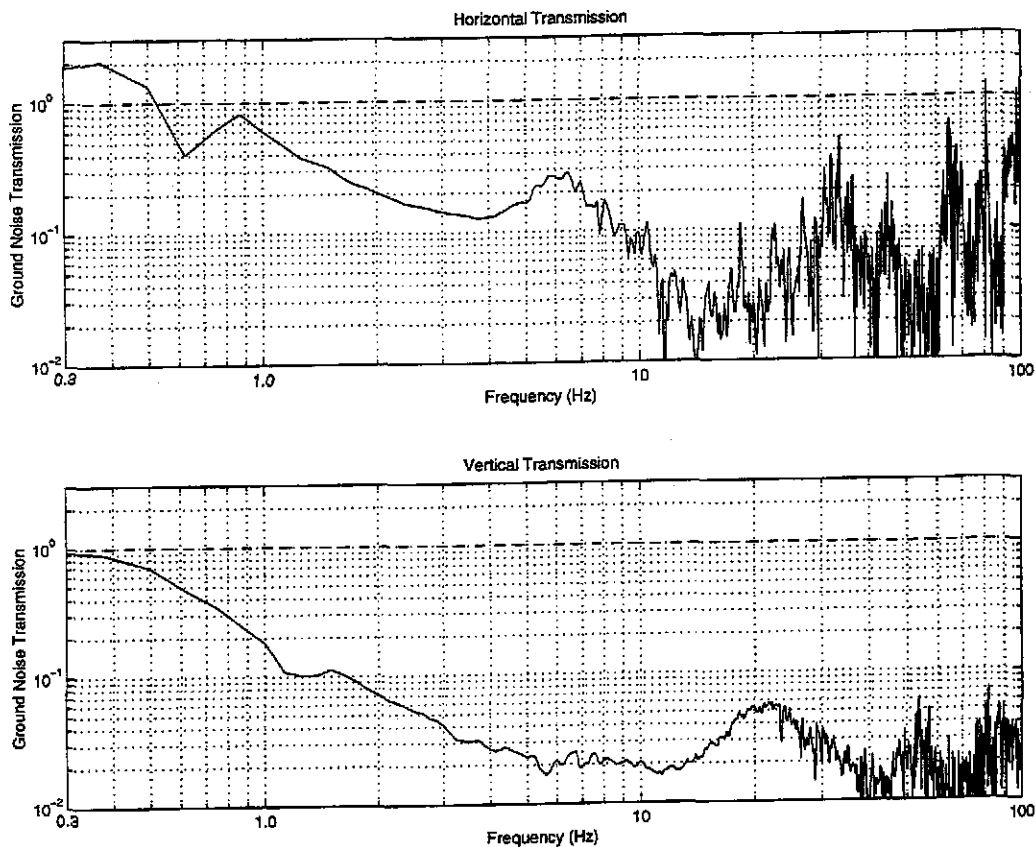


Figure 3.22: Seismic Isolation of the Input Optics Table

The coherence between floor motion and table motion is only large at frequencies less than 10Hz for horizontal motion and less than 25Hz for vertical motion.

The most likely scattering sources for the input optics were the recycling mirror, which reflects 35% of the incident carrier power (in lock), and the Faraday isolator. The recycling mirror is located within the vacuum system and supported by a seismic isolation system described in the previous section. To reduce the relative motion between it and the input optics, a set of Stacis feet was used to reduce the velocity of the input optics table. Lower relative velocity means the parasitic interferometry fringes between the input table and the interferometer would be below the measurement band. A hard-mount system such as Stacis is essential, because it preserved the alignment of the input beam with the interferometer. The transmission of floor motion to table motion is shown in figure 3.22, and the motion of the input table is shown in figure 3.23.

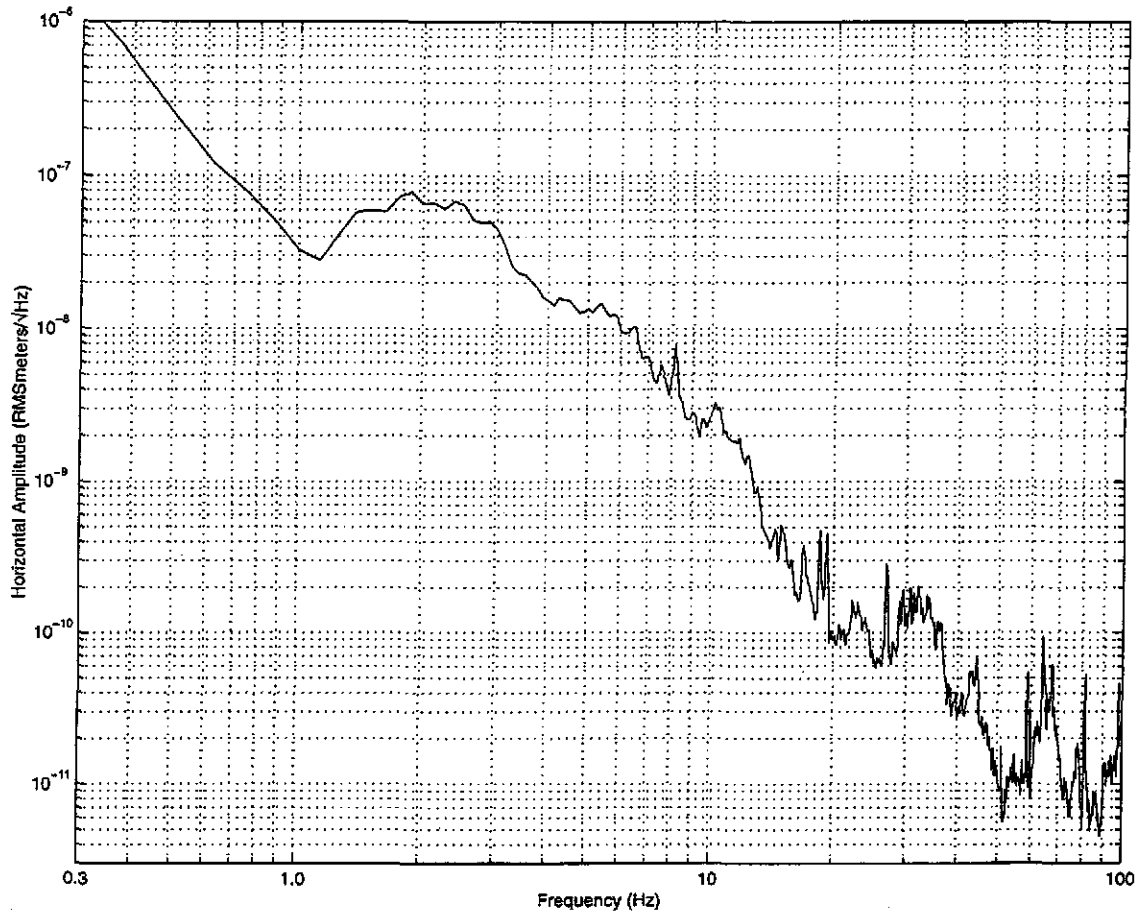


Figure 3.23: Horizontal Motion of Input Optics Table

The combined steps of cleanliness, seismic isolation, and reduced backscatter of the brewster angle polarizers reduced the level of parasitic interferometry of the input optics to the point that it was not observed during normal operation.

Parasitic Interferometry at the Output Optics Table

Parasitic interferometers at the output also cause noise. Carrier light which scatters into the TEM_{00} spatial mode at the photodetector is read out directly as signal from the instrument. This is unlike noise on the input light, where frequency noise is only coupled by the asymmetry, and amplitude noise by the average excursions from optimal fringe contrast. Parasitic interferometry amongst the output optics becomes an important noise source as the contrast loss increases due to thermal lensing (see chapter 4) or some other source of contrast loss. Contrast loss is of special concern for parasitic interferometry, because it generates excess optical power which does not contain any signal. Even if the

excess power is in higher order spatial modes, the parasitic reflectors can scatter much of the power back into the modes which have a large overlap with the TEM₀₀.

These interferometers can form either between two optics in the output chain, or between an output optic and the beamsplitter itself. The beamsplitter is particularly problematic. First, the Michelson interferometer length is set so that the Michelson "mirror" behaves as a high reflector, and second, the seismic and acoustic isolation of the interferometer imply that the mechanical admittance of the output optics and the beamsplitter are different, which accentuates the coupling of low frequency ground noise to differential path length changes of a parasitic interferometer.

We discovered that parasitic interferometry between the interferometer and the output table was a significant contributor to the excess noise of the instrument. To eliminate this noise source, four things were done:

1. Seismic isolation the output optics table.
2. Acoustic isolation of the output optics table.
3. Replacement of the length sensing photodiode.
4. Control of all specular reflections.

Seismic Isolation. The output optics table was clamped to a 500lb. granite slab, which was supported by 3 Newport XL-A pneumatic seismic isolation legs.

Acoustic Isolation. The output optics table was placed in an anechoic enclosure to reduce the acoustic drive on the optics. Acoustic drive generally excites the mechanical resonances of various optics mounts (e.g. pickoff beamsplitters, focusing lenses, and periscopes) along the output beam path. These resonances typically range from 200Hz - 1000Hz. Figure 3.24 shows the reduction of sound pressure within the enclosure over this range of frequencies.

The main improvement seen from the seismic and acoustic isolation was the increased stationarity of the interferometer spectrum, and the reduction of low frequency noise (below ~700Hz).

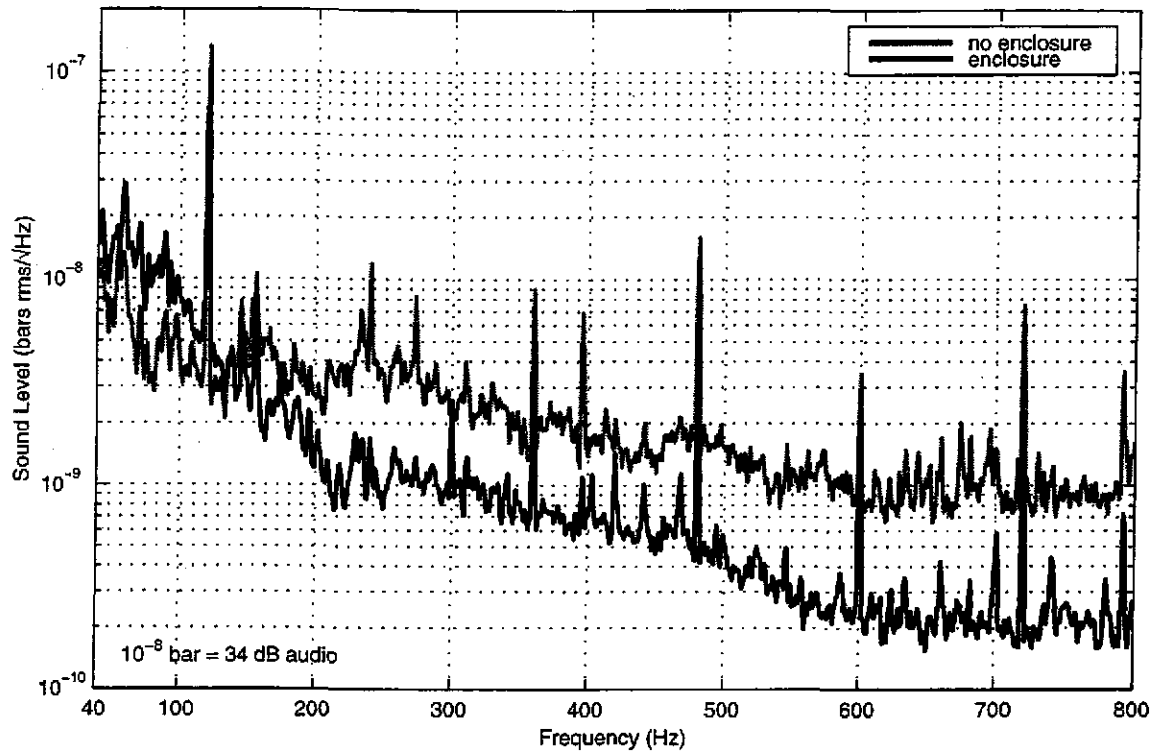


Figure 3.24: Acoustic drive level at the output optics table, with and without anechoic enclosure.

Length Diode. Another improvement of the spectrum resulted from changing the RF photodiode from a 2mm diameter Hamamatsu¹ diode with a BRDF of 1.1×10^{-4} /ster. to a physically smoother, 3mm diameter EG&G² diode with a 6.5° incidence angle BRDF of 0.37×10^{-4} /ster. [Csatorday '98]. The smoother surface reduced the backscattered intensity, and the large diameter allowed us to turn the diode at a higher angle to the incident beam and still catch all of the output beam, which further reduces the backscatter since the BRDF is greatest near the specular reflection. The diode was operated at 30° from normal incidence.

Specular reflections. Although the transmissive optics on the output table were all AR coated, specular reflections from these optics were still present. These beams were all steered off the output table and into beamstops. These beams can be problematic, since they contain much higher power per steradian than scattered light, and often end wind up incident on elements near the length photodiode, resulting in scattering paths with rela-

1. model G5832-2
2. model C30642G

tively high intensity due to the large view angle presented by the nearby photodiode. The reflected light from the length sensing diode was sent onto a piece of 1064nm absorbing glass at a 45° angle, located 70cm from the diode. Other beams were propagated a few meters into standard beamblocks.

The dominant source of backscatter into the main beam was the photodiode itself. Several different configurations of optical isolators were employed to prevent backscattered light from the diode from reentering the interferometer, but we found that the best performance was achieved with the EG&G diode at a high incidence angle, with no optical isolators. Each additional transmissive optical element we added degraded the interferometer performance, both through additional backscattered light, and through the additional specular reflected beams which needed to be captured.

The isolation allowed us to operate the interferometer at any time during the day, although the performance was severely compromised during rush hour. Although the interferometer worked during the day, the best data were still taken late at night.

beamsplitter passes through the lens twice, whereas the beam reflected by the beamsplitter is only effected by the change in the bulk curvature of the optics's surface resulting from thermoelastic deformations. Since the two wavefronts returning to the beamsplitter surface have different curvatures, it is not possible to perfectly interfere the beams. Since the TEM_{00} mode leaving the interferometer is actively servoed to the null fringe, the difference appears as higher order spatial modes which exit the dark port of the interferometer. For beams which have a parabolic curvature difference, the resulting lost power is in the cylindrically symmetric Laguerre-Gauss 1,0 mode (see [Siegman '86]). We will see that the cylindrical symmetry does not persist at high power, so Hermite-Gaussian solutions oriented along the horizontal and vertical axes of the interferometer are more appropriate, with the lost power more conveniently described as TEM_{20} and TEM_{02} modes.

The loss which results from thermal lensing impacts the interferometer performance in two ways. First, the loss lowers the recycling gain, and thus lowers the power incident on the beamsplitter, which reduces the signal level, as shown in chapter 2. Second, the light exiting the dark port in the higher order spatial modes contains no information about the interferometer length, nor will it beat against the light in the sidebands which do contain length information, because the predominant sideband intensity is in the TEM_{00} spatial mode and the photodetectors have excellent spatial uniformity. Since the readout signal is generated by the interference of the carrier and the sideband, spatial uniformity of the photodiode insures minimal mixing between spatial modes, so power in higher order modes like scattered light and contrast defect do not impact the signal level [Thorne '89, Csatorday '98]. Although there is no signal in the light which exits because of the contrast loss, the light intensity does increase the shot noise level, and so it contributes directly to the noise level of the interferometer.

The most convenient way to describe the impact of the thermal lensing on the interferometer is to examine the contrast loss as a function of the power incident on the beamsplitter. The contrast loss is simply defined as the amount of power "leaking" out of the dark port of the interferometer divided by the power incident on the beamsplitter. Figure 4.1 shows the measurement of the contrast loss for the Phase Noise Interferometer. For this measurement, the sideband power was reduced by a factor of 100, but not eliminated. Since the sideband is coupled out of the dark port by the asymmetry, this sideband power

disturbs the measurement of the carrier losses. The level of the sideband power in these measurements would be equivalent to a contrast loss of 2.5×10^{-6} . This is less than 10% of the best contrast loss, and has not been removed from any of the data.

Figure 4.1 shows an initial contrast loss of about 2×10^{-4} , falling to a minimum of 2.5×10^{-5} at 36 watts of power incident on the beamsplitter, and then rising as the beamsplitter power increases. The initial loss is a result of the Michelson asymmetry. Since both of the Michelson end mirrors are flat, the path length asymmetry results in a mismatch of the gaussian parameters of the two beams returning to the beamsplitter from the Michelson arms. As the power increases, the beamsplitter heats up and begins to act as a lens for the light transmitted to the on-axis mirror. In the PNI, $\frac{dn}{dT}$ is positive, the on-axis arm is longer than the off-axis arm, and the cavity waist is at the average position of the Michelson arm lengths, so the initial lensing improves the matching of the arms, and acts to improve the contrast loss. However, figure 4.1 illustrates that the lensing is strong enough to compensate for the asymmetry at about 36 watts of incident power. As the power increases, the lensing overwhelms the asymmetry, and the contrast loss begins to increase.

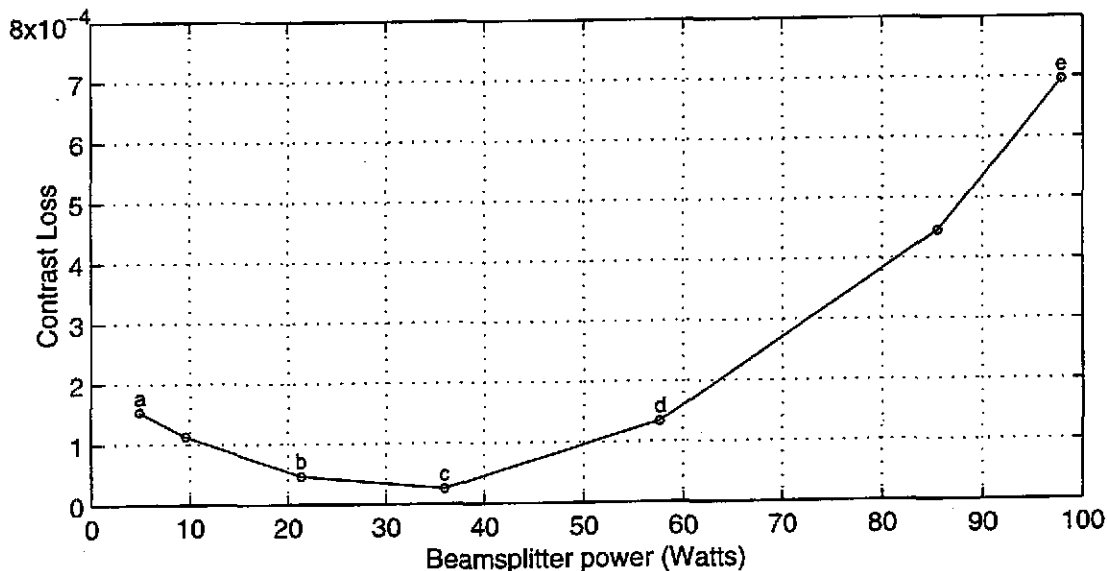


Figure 4.1: Measured contrast loss of the beamsplitter as a function of incident power. Data points are shown as circles. The letters correspond to the powers at which the images in figures 4.8 - 4.12 were taken.

Initially, the interferometer was designed to run at about 120 watts of circulating power, but the excess power at the dark port resulting from the high loss decreased the interferometer sensitivity. A more modest 70 watts yielded the best interferometer results.

The beamsplitter is believed to be the lensing culprit for two reasons. First, it is the only transmissive optic in the Michelson interferometer, and fused silica transmissive optics are much more sensitive to thermal lensing than reflective optics because of the relatively small impact of thermoelastic deformations described above. Second, the images of the beam exiting the dark port show that the beam is not axially symmetric, indicating an astigmatic thermal lens. Of the four suspended optics, which are the only optics exposed to the full recycled power, only the beamsplitter sees a beam which is not axisymmetric. Since the beamsplitter is angled at 50 degrees to the incident beam, the light propagates through the optic at an angle of 32 degrees from normal. Although the freespace beam is circular, the beam in the beamsplitter becomes elliptical, with different ellipticities on the surface and in the bulk.

When an elliptical beam is propagated through an optic, the resulting thermal lens is not axially symmetric. Inside the beamsplitter, the beam is wider than it is tall, but the lens within the optic is foreshortened by the change in propagation direction of the beam at the optic surface, resulting in interesting astigmatic effects.

4.2 Modeling of the Thermal Lens

Ryan Lawrence, a graduate student at MIT, constructed a three-dimensional model of our beamsplitter geometry using a finite element analysis program called Ideas™. The model showed that the thermal lens (as seen in the frame of the freespace beam) is stronger in the horizontal direction than the vertical direction. The resulting horizontal and vertical lenses were used to calculate the expected intensity pattern of the beam emerging from the dark port.

4.2.1 Thermal Lens parameters

The finite element model was used to track the heat flow within the optic and was used to generate a set of six parameters which describe the thermal lens generated by the beamsplitter. The model tracks heat input from the elliptical beam, heat flow within the optic, and radiation losses from the optical surface. The temperature increase of the material is calculated, then the change in optical path length along the beam direction is calculated for many points within the beam. Since it is a full three-dimensional model, it correctly accounts for the effects of non-radial heat flow. It also accounts for the fact that,

in surface heating at non-normal angles, one side of the transmitted beam is transmitted through much more heated material than the other side, as is shown in figure 4.2.

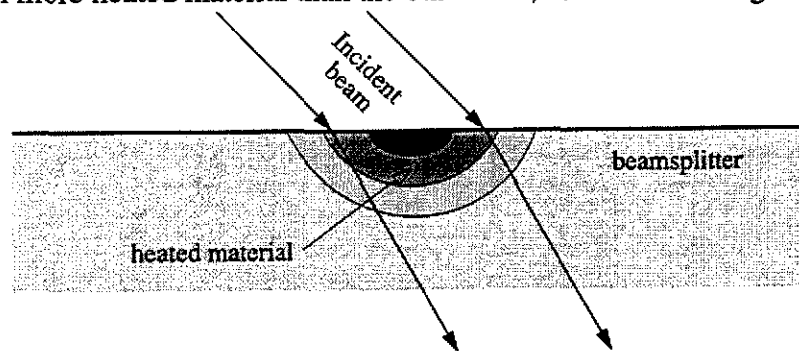


Figure 4.2: Schematic view of the heat flow from surface absorption of the beamsplitter. Power absorbed from the laser by the coating flows into the substrate and heats it. Since the beam is not normal to the surface, one side of the beam (here, the left side) travels through more heated material than the other side, and so the thermal lens is not symmetric.

This results in a lens which is not centered on the incident beam because the center of the beam does not travel through the path of greatest integrated thermal distortion within the optic. Modeling shows that the lens is not symmetric even when the first order thermal “wedge” is removed.

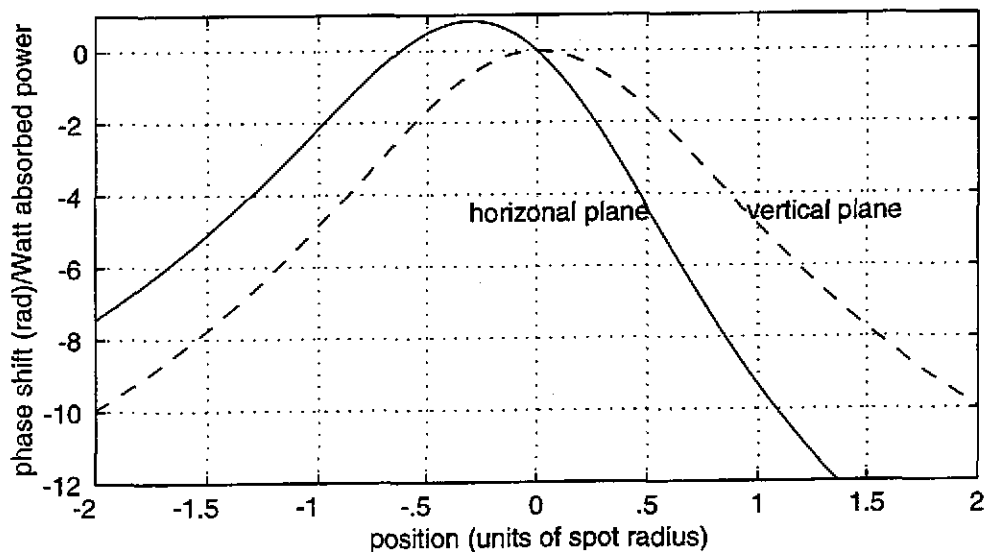


Figure 4.3: Thermal distortion of the beamsplitter for power absorbed at one surface. The center of the thermal lens effect has been arbitrarily set to 0 phase shift in this figure and in figure 4.4 to ease the comparisons of the curvatures in the two directions.

The finite-element model yielded a pair of two-dimensional maps of the path length added by the thermal distortion generated by the heat absorbed at the surface and by the heat absorbed in the bulk. Since Gaussian beam propagation through an ideal lens is completely described by the parabolic coefficient of the lens along its primary axes, the two-

dimensional phase map of the distortion was reduced to a few parameters. Cuts through the phase surface in the horizontal and vertical direction are shown in figures 4.3 and 4.4.

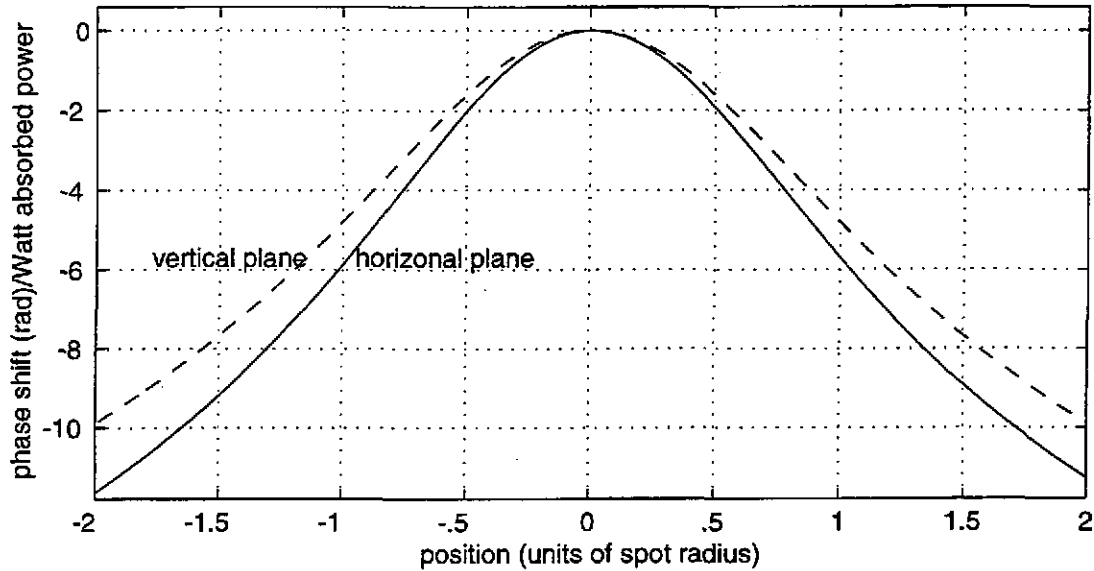


Figure 4.4: Thermal distortion of the beamsplitter caused by bulk absorption

These four curves were then used to generate the six parameters used in a beam propagation calculation. Four of the parameters were the best fit parabolas to the models out to 1 beam radius (1.3mm). These parabolas describe the thermal deformation as an ideal lens in the horizontal and vertical planes, in units of curvature per μWatt of absorbed power.

Table 4.1: Model Parameters

| Lens | Curvature |
|-----------------------------|---|
| Surface, horizontal | $-5.78 \times 10^{-7} \frac{\text{meters}}{\text{meters}^2 \cdot \mu\text{Watt}}$ |
| Surface, vertical | $-5.05 \times 10^{-7} \frac{\text{meters}}{\text{meters}^2 \cdot \mu\text{Watt}}$ |
| Bulk, horizontal | $-6.01 \times 10^{-7} \frac{\text{meters}}{\text{meters}^2 \cdot \mu\text{Watt}}$ |
| Bulk, vertical | $-4.90 \times 10^{-7} \frac{\text{meters}}{\text{meters}^2 \cdot \mu\text{Watt}}$ |
| Bulk, horizontal correction | $-1.67 \times 10^4 \frac{\text{m}}{\text{m}^6 \cdot \mu\text{W}} + 1.76 \times 10^{-1} \frac{\text{m}}{\text{m}^4 \cdot \mu\text{W}} - 2.28 \times 10^{-7} \frac{\text{m}}{\text{m}^2 \cdot \mu\text{W}}$ |
| Bulk, vertical correction | $-1.29 \times 10^4 \frac{\text{m}}{\text{m}^6 \cdot \mu\text{W}} + 1.37 \times 10^{-1} \frac{\text{m}}{\text{m}^4 \cdot \mu\text{W}} - 1.83 \times 10^{-7} \frac{\text{m}}{\text{m}^2 \cdot \mu\text{W}}$ |

These six parameters are used to define the properties of the astigmatic thermal lens generated by the beamsplitter. The units for the first four entries are lens curvature per total absorbed power.

Figures 4.3 and 4.4 show that the thermal distortions are not perfect parabolas. Since it is assumed that most of the absorption is in the bulk of the material, two additional parameters were generated to describe the lens. These are 6th order polynomial fits to the residuals for the bulk out to 2.0 mm. The parameters are shown in table 4.1

4.2.2 Propagation Model

Once the lensing properties of the beamsplitter are known, the performance of the interferometer can be modeled to predict the spatial profile of the beam exiting the dark port as a function of the power incident on the beamsplitter and the optical absorption.

The propagation model is based on simple ABCD gaussian beam propagation matrices. The horizontal and vertical axes of the beam are propagated independently. The initial beam incident on the beamsplitter is described by the spot size and radius of curvature in the horizontal and vertical directions. There are six basic steps of the propagation model.

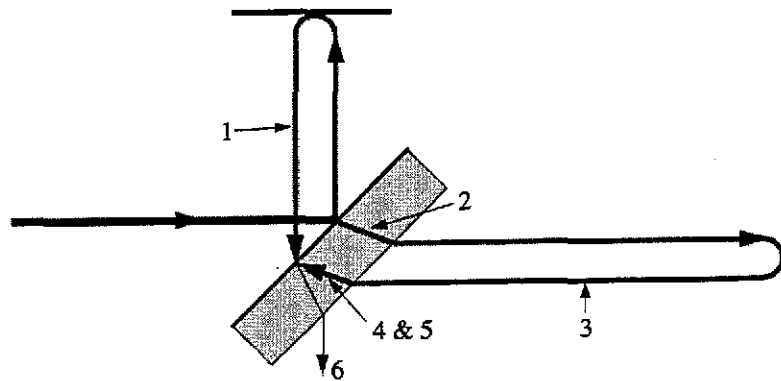


Figure 4.5: Diagram listing the steps of the beam propagation model

1. The off-axis beam is propagated through a free-space of twice the length of the off-axis arm (42 cm) and the resulting beam parameters are used to generate a two-dimensional electric field at the beamsplitter.
2. The beamsplitter is modeled as a beam duct with a quadratic index. The quadratic index is calculated from the parameters in table 4.1, the power passing through the beamsplitter, and selected numbers for the coating and bulk absorption. The two beam parameters are then each propagated through the appropriate "duct". [Siegman '86]
3. The beam parameters are propagated through a free-space length of twice the on-axis arm (58 cm each way).
4. The parameters are again propagated through the beamsplitter duct, and then the two dimensional electric field at the beamsplitter surface is generated.
5. The electric field of the on-axis arm is phase-shifted by the perturbation correspond-

ing to the non-parabolic component of the thermal lens.

6. The electric fields from the two arms are combined with the phase which minimizes the total power. The total output power and its spatial distribution are generated.

The total absorption necessary to make the model yield a contrast loss curve similar to the data was quite large. It necessitated an absorption which was either 47 ppm/cm for the bulk, or 90 ppm at the back surface, given a $\frac{dn}{dT}$ of 1.18×10^{-5} .

The majority of the absorption was assumed to be in the bulk of the beamsplitter, because, for such a large surface absorption, the effects of the asymmetric horizontal thermal lens should have been quite obvious, but were not seen. In fact, the dark port beam profile was quite symmetric right to left, so the absorption was assumed to be in the bulk of the beamsplitter.

The best fit to the measured power output curve, with 1 ppm absorption at each surface, was given by a bulk absorption of 47 ppm/cm. This is a factor of 3 higher than the optic specification of 15 ppm/cm, and independent measurements of the bulk and surface absorption of the beamsplitter are planned for the future to find the actual values of the absorption and $\frac{dn}{dT}$ for this sample. The power predicted by the model is shown below in figure 4.6.

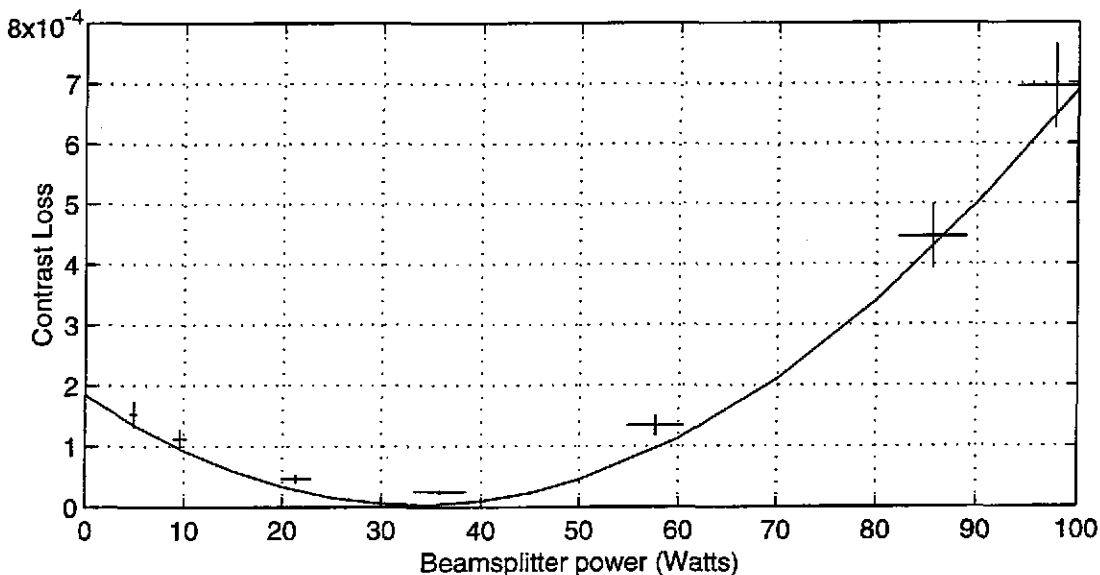


Figure 4.6: Measured contrast loss and predicted contrast loss with 47 ppm/cm bulk absorption. The solid line is the predicted contrast loss, and the crosses are the data (with uncertainty) measured with reduced sideband intensity.

Although a simple lens at the position of the beamsplitter predicts a contrast loss which is almost identical to figure 4.6, the advantage of tracking the two axes of the beam independently is that intensity profiles of the output can be generated and compared with the measured spatial distributions in figures 4.8 - 4.12. A set of modeled intensity plots is shown below in figure 4.7. At low power, the distribution is axially symmetric, then the intensity becomes larger on the top and bottom until the best contrast point is reached, beyond which the brightest points on the outer ring are to the sides of the central spot.

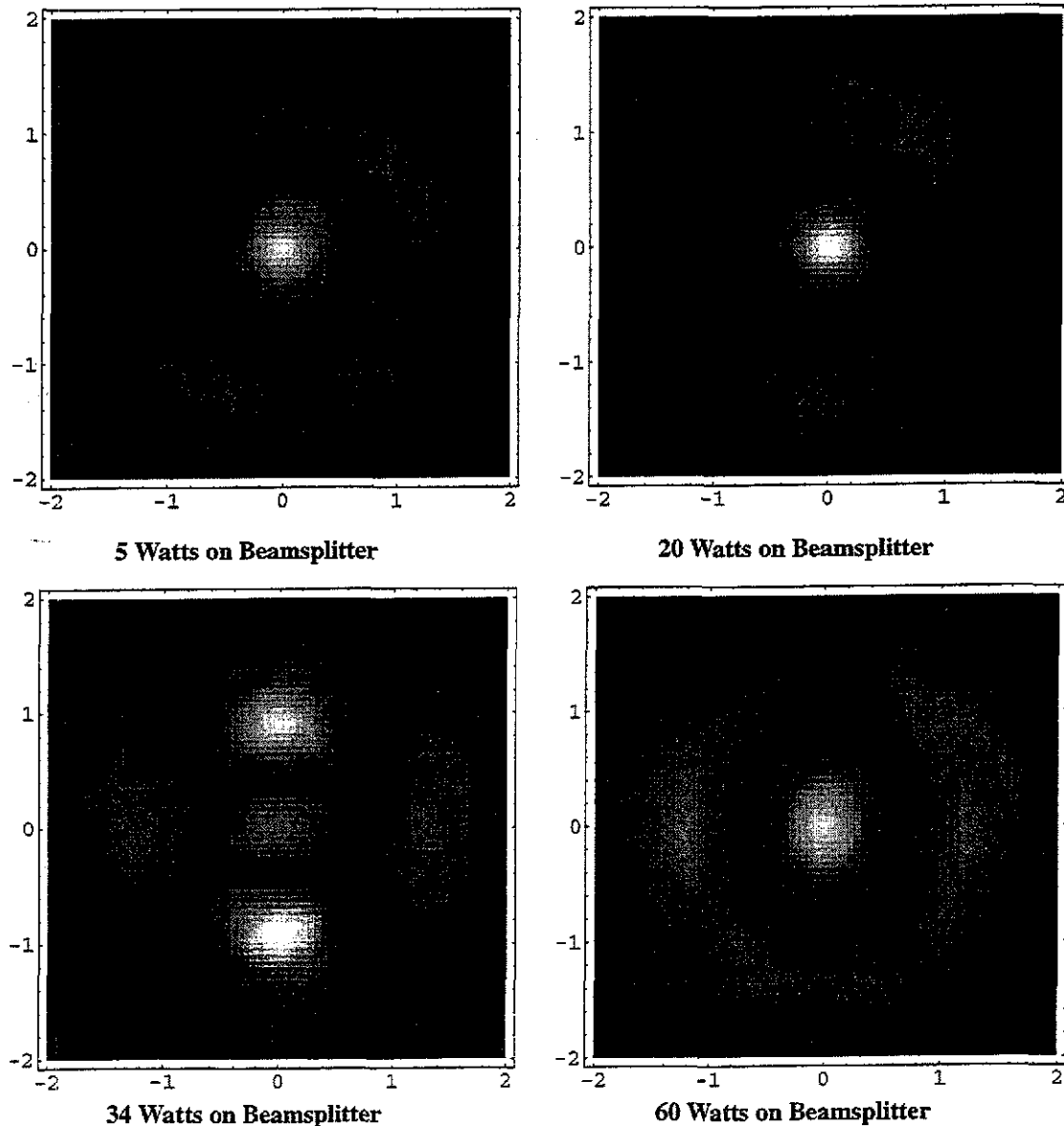


Figure 4.7: Modeled intensity distribution of the dark fringe. The spatial scale is in units of beam radius. All of the intensities have been normalized to 1 at the brightest point in the picture to emphasize the change in the spatial distribution.

This behavior can be explained by the differing curvature per absorbed power parameters generated by the finite element model. The curvature, and hence the "lens," is stronger in the horizontal direction than in the vertical direction. At low power, the arm length imbalance means that there is minimal thermal lensing, so the beam returning from the on-axis arm has more curvature than the beam from the off-axis arm. (Since the two spots are 8.5% and 11.8% of the Rayleigh range from the beam waist, the spots are similar in size.) As the power incident on the beamsplitter increases, the thermal lens in the horizontal plane becomes more powerful than the thermal lens in the vertical plane, and compensates for the path length asymmetry more completely, allowing better contrast in the horizontal plane than in the vertical plane, so the cylindrical symmetry is broken and the output resembles a TEM₀₂ mode. At the best overall contrast, the horizontal plane is slightly overcompensated, and the vertical plane is still slightly undercompensated, yielding a cross pattern as seen in the 34 watt picture. As the power incident on the beamsplitter increases, the lenses both overcompensate the asymmetry, and so the stronger lens (horizontal) now has worse contrast, and there is more power in the horizontal plane than in the vertical.

Images of the beam at the dark port show that the interferometer qualitatively matches the modeling work. Figures 4.8 through 4.12 show pictures of the dark port beam at various power levels. The RF modulation sidebands are reduced to a low level, so that even in figure 4.10, which shows the intensity pattern at the best contrast, less than 10% of the total power is from the sidebands. The series of images shows an output pattern which evolves along the horizontal and vertical planes of the interferometer. These planes are shown in the pictures as cross-hairs. The image rotation results from the periscopes used to steer the beams out of the interferometer.

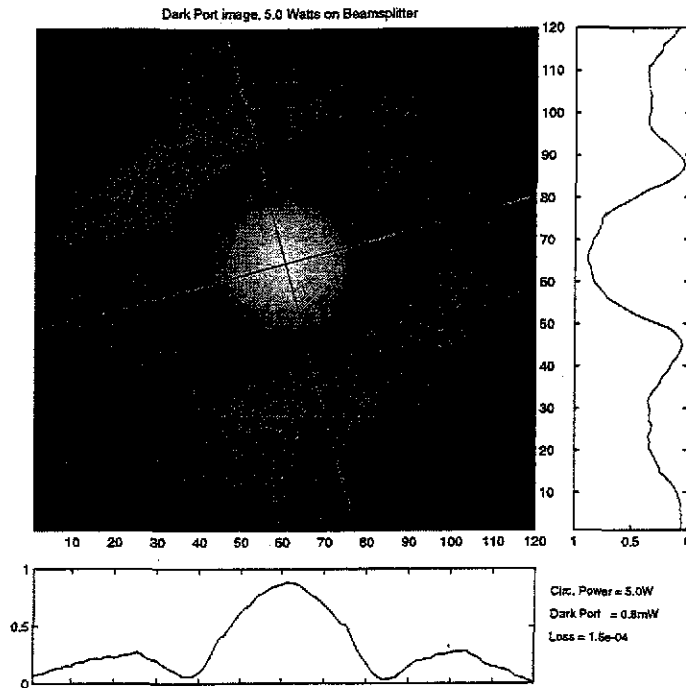


Figure 4.8: Image of Dark Port beam with 5 watts of circulating power in the interferometer. Note that the beam is almost perfectly axisymmetric. The curves on the side and bottom on the image are the intensity along the cross-hairs superimposed on the image. The intensity scale is linear, where 0 is no light, and 1 represents the maximum light the camera electronics can process (at current gain settings and optical attenuators, etc.) without saturating. This level changes from image to image.

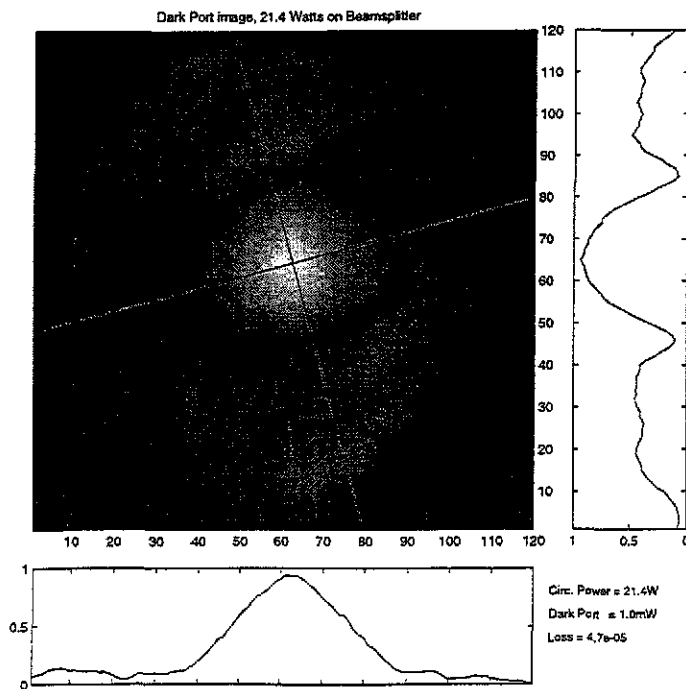


Figure 4.9: Dark Port image with 21 watts of circulating power. Note how the pattern has bulges to the top and bottom of the central peak.

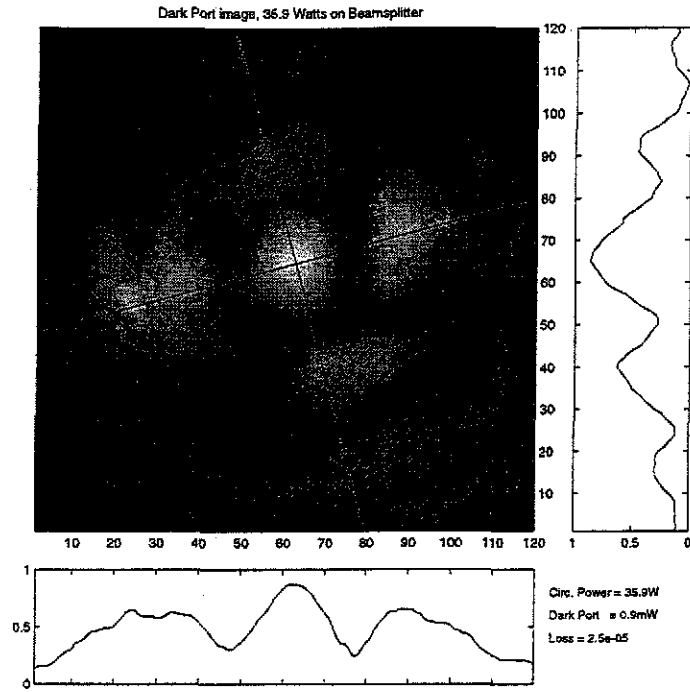


Figure 4.10: Dark Port Image with 36 watts of circulating power. This is the circulating power level which yields the best contrast.

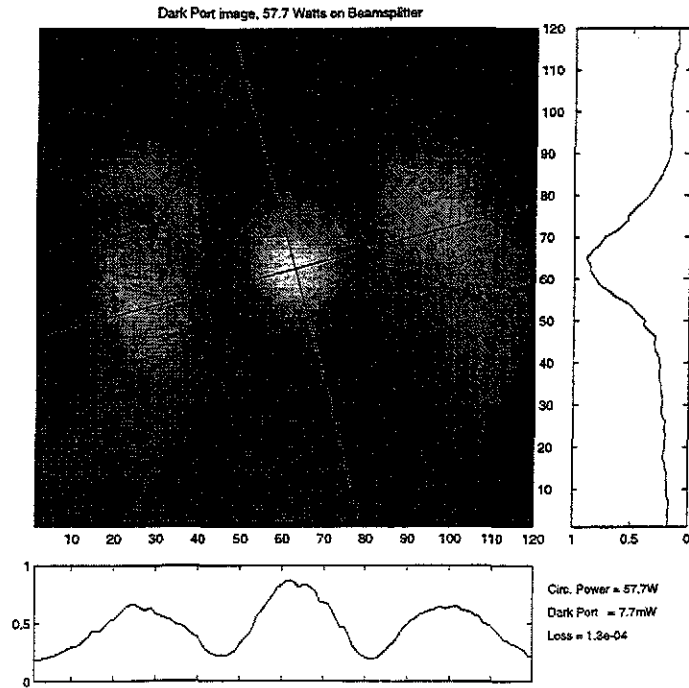


Figure 4.11: Dark Port Image with 57 watts of circulating power

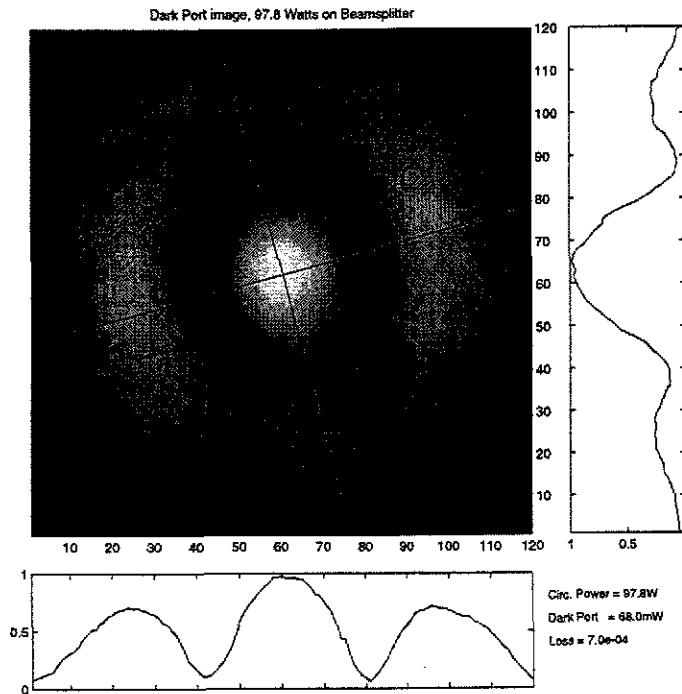


Figure 4.12: Dark Power image with 98 watts of circulating power

The horizontal lobes of the intensity distribution are evident both at this power level and at the 57 Watt level shown above in figure 4.11.

The model accurately predicts the emergence of the vertical lobes at powers less than the optimal contrast, followed by horizontal lobes at powers greater than the optimal contrast. Near the optimal contrast point, the model does generate cross shaped patterns but does not yield as much structure as was actually observed at the dark port, and the power loss prediction it gives is too low, which corresponds with lack of higher order structure and other loss mechanisms in the model.

The natural question to ask with any shot-noise limited experiment is what prevented the use of additional power. In this experiment, the limit is clearly set by the contrast loss caused by thermal lensing of the beamsplitter. The astigmatic effects of beamsplitter thermal lensing are clearly seen in the images of the dark port beam. The losses required to explain the contrast loss we measured (47 ppm/cm with a $\frac{dn}{dT}$ of 1.18×10^{-5}) are higher than expected, and future measurements need to be made to confirm the model.

Chapter 5

Phase Sensitivity and Phase Noise

5.1 Measurement of the Optical Phase Sensitivity

Measurements of the optical phase were taken by examining the error signal of the differential mode output. The differential length of the interferometer is under active control, with a unity gain frequency of 1kHz. The measurement band of interest for this experiment, which ranges from 150Hz to 10kHz (see chapter 1), overlaps with the active band of the servo, so measurements of the error signal must be corrected by the loop gain to be meaningful.

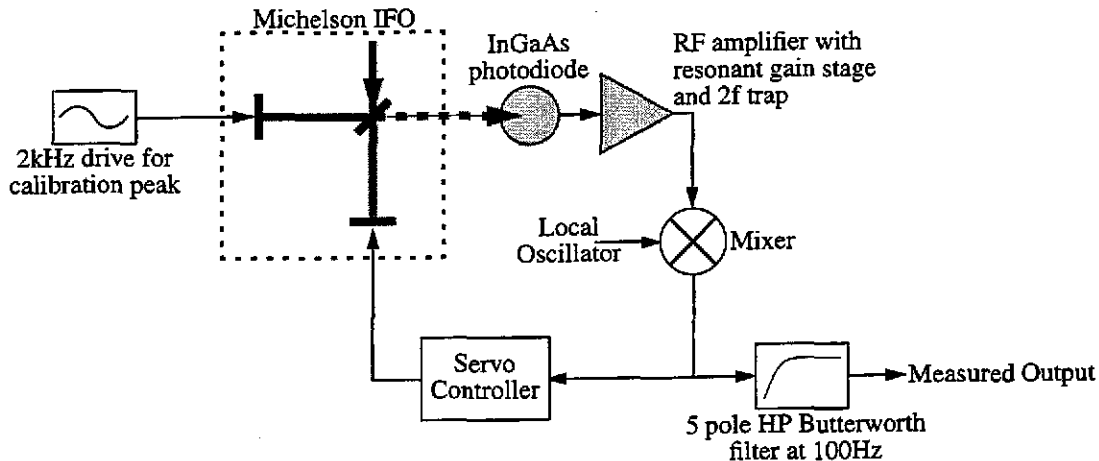


Figure 5.1: Schematic view of Michelson interferometer readout and control configuration.

To measure the phase sensitivity of the interferometer, we measure the spectrum of the signal at the point "Measured Output," correct by the loop gain, then calibrate by matching the amplitude of the calibration signal to its known value.

5.2 Result of the Measurement

The resulting calibrated phase measurement is shown in figure 5.2. The spectrum is limited by shot noise at frequencies above 600Hz, and shows several features.

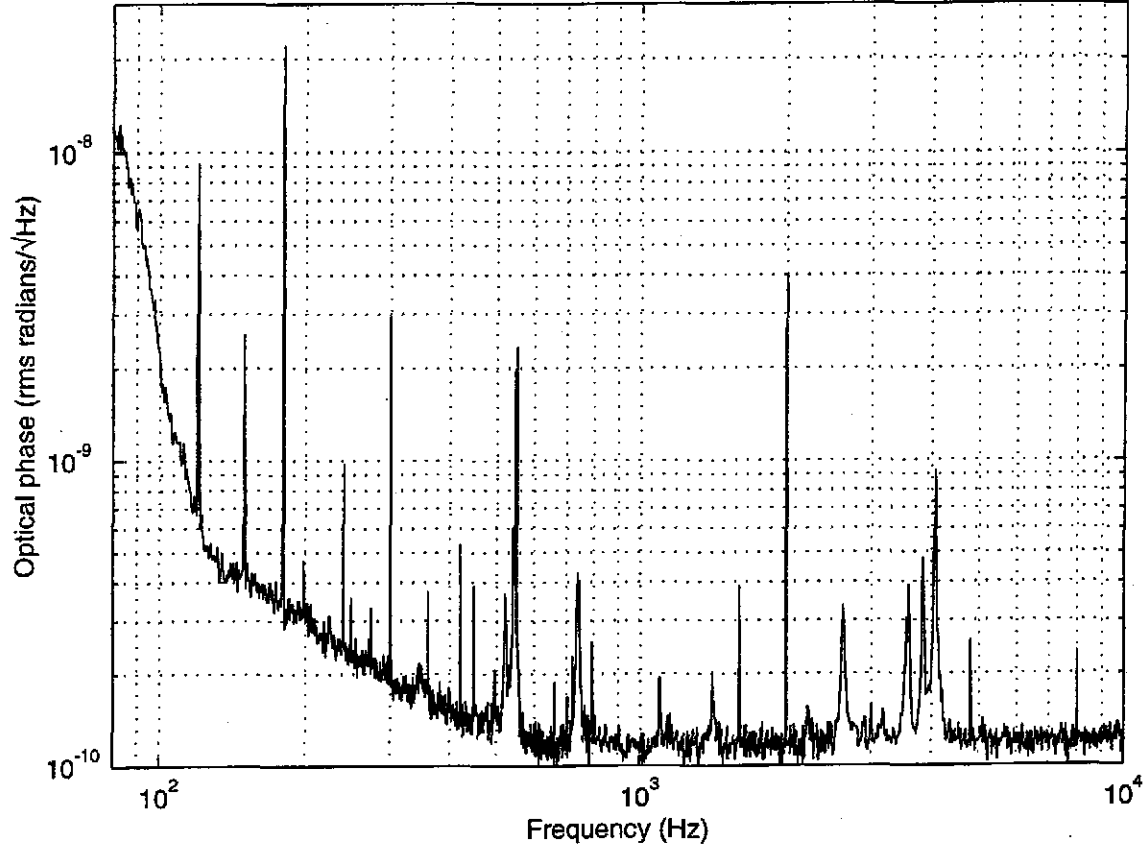


Figure 5.2: Spectrum of the Phase Noise Interferometer.

5.2.1 Shot Noise Limited Regime

In chapter 2 we showed that the shot noise limited sensitivity for a recycled Michelson interferometer with this readout configuration is

$$\Delta\tilde{\phi}(f) = \sqrt{\frac{h\nu}{\eta P_{0,BS}}} \sqrt{3 + CSB_{dp}} \sqrt{1 + \frac{L_C}{\sin^2(2k_{SB}A)}}, \quad (5.1)$$

which expresses the sensitivity in terms of the carrier power at the beamsplitter, parameters of the modulation readout scheme, and loss parameters (the contrast loss L_C , and the dark port carrier to sideband ratio, CSB_{dp}) which describe the imperfections of the recycling cavity (and are not independent of the carrier power at the beamsplitter.)

A series of measurements are required to obtain these parameters. The carrier to sideband ratio at the dark port is determined by comparing the levels of the DC intensity to the intensity at twice the modulation frequency in a beam picked off from the dark port out-

put. The ratio of the power in the carrier to the power in one of the sidebands is then calculated to be

$$CSB_{dp} = \sqrt{2} \frac{I_{DC}}{I_{2f}} - 2 = 2.7(1) \quad (5.2)$$

where I_{DC} is the DC intensity and I_{2f} is the rms intensity at twice the modulation frequency.

The power at the beamsplitter can be determined two different ways. The most direct measurement involves finding the sum of the power in the two Michelson arms. Before the experiment was put under vacuum, the transmission of the two Michelson arm mirrors were measured to be 7.22(7) ppm for the on-axis mirror and 7.52(8) ppm for the off-axis mirror. One of these beams was directed into an optical spectrum analyzer to measure the carrier to sideband ratio of the light at the beamsplitter. By measuring the power transmitted by the two Michelson mirrors, one calculates that the carrier power incident on the beamsplitter is

$$P_{0,BS} = \left(\frac{T_1}{7.22(8) \times 10^{-6}} + \frac{T_2}{7.52(8) \times 10^{-6}} \right) \frac{CSB_{BS}}{CSB_{BS} + 2} = 67(3) \text{ Watts}, \quad (5.3)$$

where T_1 is the power transmitted by the on-axis mirror and T_2 is the power transmitted by the off-axis mirror.

If the performance of the recycling cavity is well characterized, then the power incident on the beamsplitter can be predicted by measuring the input power, P_{in} , the input carrier to sideband ratio, CSB_{in} , the mode matching parameter, M , and the recycling gain, RG . The predicted carrier power at the beamsplitter is

$$P_{0,BS} = P_{in} \cdot RG \cdot M \cdot \frac{CSB_{in}}{CSB_{in} + 2}, \quad (5.4)$$

where the recycling gain (from eqn. 2.35) is

$$RG = \frac{4T_{RM}}{(T_{RM} + L)^2}. \quad (5.5)$$

The measurement of the cavity loss, L , and the mode matching parameter, M , are accomplished by measuring the intensity of the carrier and the sidebands reflected from the recycling cavity when the cavity is moved in and out of lock.

The reflectivity of a Fabry-Perot cavity in resonance can be expressed as

$$R_0 = (1 - M) + M \left(\frac{L - T_{RM}}{L + T_{RM}} \right)^2, \quad (5.6)$$

where L is the cavity loss (excluding the transmission of the input mirror), T_{RM} is the power transmission of the input coupler (the recycling mirror). The sidebands see an additional cavity loss introduced by the asymmetry, so the cavity reflectivity for the sidebands is

$$R_{\pm} = (1 - M) + M \left(\frac{L + \sin^2(2k_{SB}A) - T_{RM}}{L + \sin^2(2k_{SB}A) + T_{RM}} \right)^2. \quad (5.7)$$

By comparing the reflectivity of the recycling cavity to the carrier and the sidebands, we can solve for L and M .

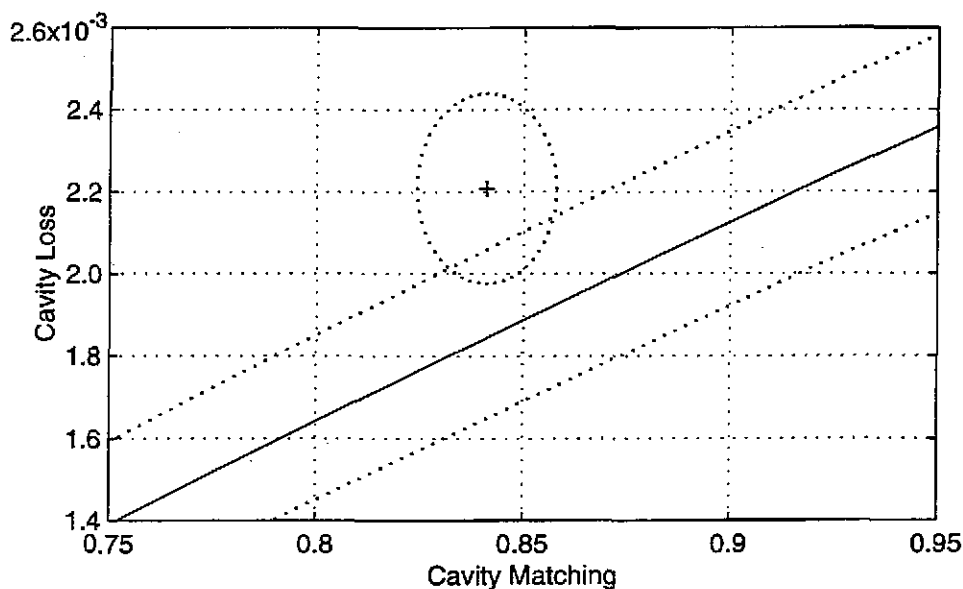


Figure 5.3: Cavity Loss (L) and Cavity Matching parameter (M) calculation.

The circle is the result of comparing the cavity reflectivity of the carrier and sidebands (eqn. 5.6 and 5.7), the error circle assumes 5% error for the carrier ratio and 10% error for the sideband ratio. The solid line is the prediction based on ratio of the carrier ratio at the input and the beamsplitter (eqn. 5.4) with 5% error on the ratio.

Based on the data shown in figure 5.3, we assign the cavity loss, L , to be 2×10^{-3} and the cavity matching, M , to be 0.85.

We can attempt to make an accounting of the losses which contribute to L , which are dominated by the reflectivity of the antireflective coating on the back side of the beam-

splitter, and by the contrast loss from thermal lensing of the beamsplitter. These losses (with 70W incident on the beamsplitter) are:

$$\text{AR loss: } 2 \cdot T_{\text{BS}} \cdot R_{\text{ARcoating}} = 2 \cdot 0.44 \cdot 1.47 \times 10^{-3} = 1.29 \times 10^{-3}$$

$$\text{Contrast loss: } 2.6 \times 10^{-4}$$

$$\text{Bulk Absorption: } 1.1 \times 10^{-4}$$

However, this leaves a loss of $\sim 3.4 \times 10^{-4}$ (or 17%) unaccounted for, which is most likely scattering from the mirror surfaces and extra loss at the AR coating.

We have the values $h\nu = 1.87 \times 10^{-21}$ Joule, $\eta = 0.85(3)$, $P_{0, \text{BS}} = 67(3)$ Watts, $CSB_{\text{dp}} = 2.7(1)$, $L_C = 2.6(2) \times 10^{-4}$, and $\sin^2(2k_{\text{SB}}A) = 7.31 \times 10^{-3}$. Putting these into expression 2.68 for the shot noise,

$$\Delta\tilde{\phi}(f) = \sqrt{\frac{h\nu}{\eta P_{0, \text{BS}}}} \sqrt{3 + CSB_{\text{dp}}} \sqrt{1 + \frac{L_C}{\sin^2(2k_{\text{SB}}A)}}$$

we see that the predicted sensitivity limit is

$$\Delta\tilde{\phi}(f) = 1.36(5) \times 10^{-10} \text{ rad}/\sqrt{\text{Hz}} \quad (5.8)$$

The measured sensitivity is $\Delta\tilde{\phi}(f) = 1.21(4) \times 10^{-10} \text{ rad}/\sqrt{\text{Hz}}$ measured in regions between the features in the spectrum. The uncertainty of 3% comes from the uncertainty in the amplitude of the calibration peak. We see that the error bars do not quite overlap, which is probably due to a systematic overestimate of the carrier to sideband ratio at the output, or a systematic overestimate of the amplitude of the calibration peak. However, the measured value of the sensitivity is only 11%, or 0.9dB away from the value predicted by theory.

5.3 Spectral Features

There are a variety of physical processes which produce features in the interferometer spectrum. This section provides a catalog and brief description of most of the narrow spectral features evidenced in the spectrum shown in figure 5.4.

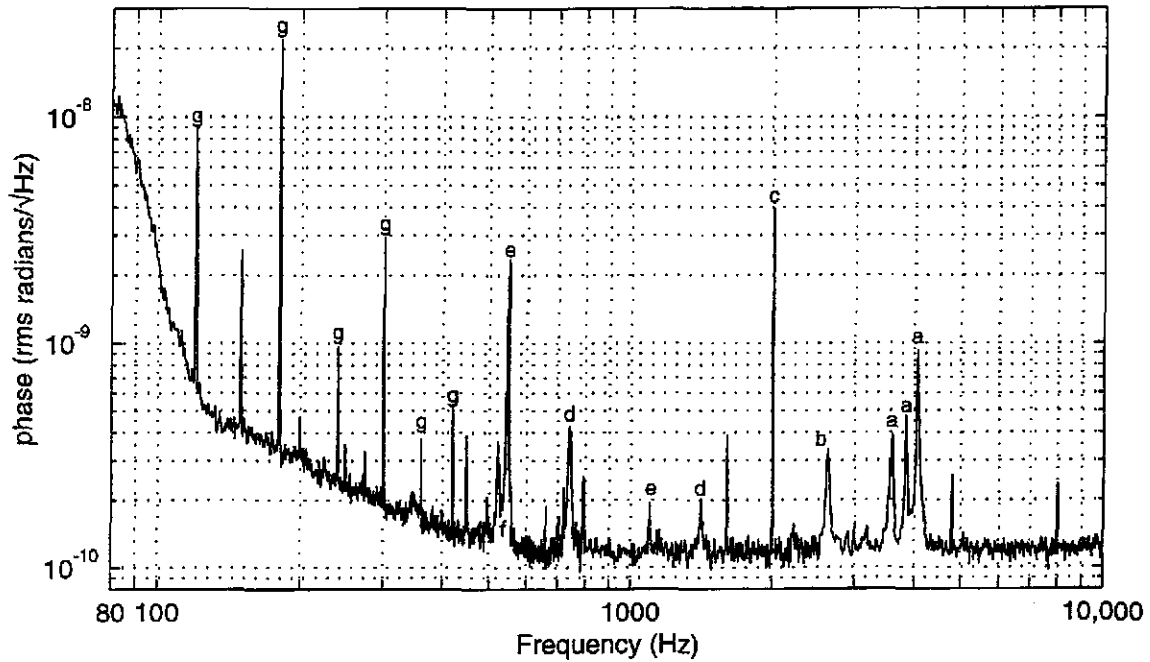


Figure 5.4: Narrow spectral features.

| Peak | Frequency | Description |
|------|-----------------------|---|
| A | 3.58, 3.84, & 4.06kHz | Thermal motion of magnet-fin assemblies |
| B | 2.504kHz | Motion of 25MHz phase modulator on input table |
| C | 2.000kHz | Calibration peak |
| D | 740Hz, 1.40kHz | Motion of faraday rotator on input optics table |
| E | 550Hz & harmonics | Violin modes of suspension wires |
| F | 540 Hz | motion of steering mirror on input optics table |
| G | 60 Hz & harmonics | power line noise |

Table 5.1: Narrow Spectral Features

5.3.1 Thermal Motion of Magnetic Actuator Fins.

The set of three peaks around 4kHz are the resonances of the fin - magnet - standoff assemblies which are glued to the interferometer optics for control and local sensing, as shown in figure 5.5 (see also figure 3.15). These resonances are driven by thermal motion. (They make a very reliable indicator of machine performance, since their amplitude was constant, although not independently calibrated.)

The impact of thermal noise is discussed in more detail in section 5.4.2, where we discuss the amplitude of both the resonant and off-resonant motion caused by thermal fluctuations.

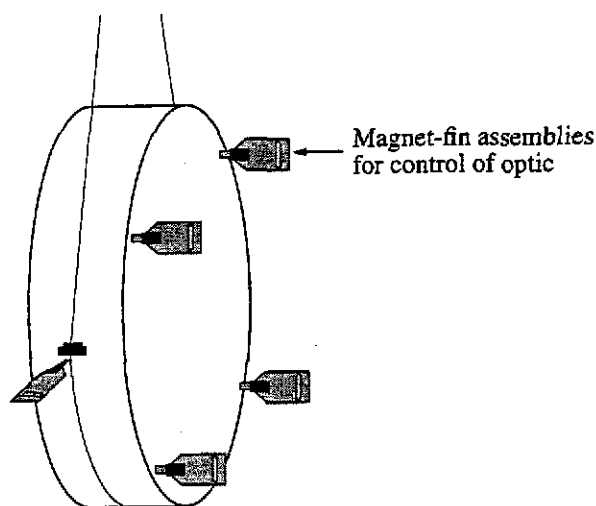


Figure 5.5: Drawing of an interferometer optic, showing the magnet-fin assemblies.

5.3.2 Calibration peak at 2kHz

The line at 2.00kHz is the calibration peak, which is produced by driving one of the Michelson arm mirrors with a calibrated test signal. The force is applied to the optic with the magnet coils in the OSEMs. The calibrated motion of the optic at 2kHz was used to calibrate the entire measurement.

5.3.3 Motion of Optics on Input Table

Several of the peaks in figure 5.4 were caused by mechanical vibration of components on the input table. These were identified by driving various optical components and noting how the interferometer output and the input beam angle monitor responded.

The largest peaks were caused by motion of the Faraday rotator, the polarization rotation component of the Faraday Isolator on the input table which separated the incident light on the interferometer from the reflected light (see figure 3.7) used to lock the recycling cavity length and improve the laser frequency stability. The rotator gave peaks at 740Hz and 1.40kHz.

The broad peak at 540Hz, which sits below the suspension wire violin mode peaks, came from one of the 2" steering mirror mounts used to direct the beam into the cavity. The performance of this mount was suboptimal because the adjustment screws had been replaced by heavier PZT drivers used for beam jitter measurements described in section 5.4.

The peak at 2.50kHz was caused by motion of the 25.556MHz phase modulator.

5.3.4 Violin Modes of Suspension Wires

The first three violin modes of the suspension wires can also be seen. The fundamental modes are around 550Hz, and seem to be excited primarily by seismic noise. The amplitude of the fundamental peaks was seen to vary, although the amplitude in figure 5.4 was not much higher than the excitation from thermal noise. The resonant and off-resonant thermal noise predictions are discussed in section 5.4.2.

5.3.5 Power Line Noise

Effort was taken to reduce the impact of the 60Hz harmonics on this instrument. The greatest improvement came from moving from the Argon Ion plasma laser to a solid state Nd:YAG device. Further improvements were made by moving the large DC supplies away from the instrument racks to reduce the magnetic field coupling from the power supply transformers. The remaining noise is dominated by the long wires which feed the mirror control signals from the instrument rack to the mirror controllers, which were located at the far end of the interferometer. Due to power requirements, these controllers were on a different power circuit from the instrument racks, which introduced ground loops, evidenced by the change in the mirror coil-drive monitor when the angular control input was disconnected.

5.4 Low Frequency Noise

The noise from 100Hz to 500Hz in the final spectrum has not been definitively identified. There are several noise sources which contribute, the two largest sources are electronic noise from the length controller, and noise induced by beam jitter.

5.4.1 Electronic Noise

Electronic noise is a concern for this type of measurement. The high light levels and RF readout scheme enable the electronic noise at the readout to be a factor of 6.2 below

the shot noise (causing a noise contribution of 1.3%). The control electronics are more problematic, however, since they operate at the base band. Noise from the control feeds into the measurement by adding noise to the driver of the optics. Current noise from the controllers feeds into the OSEM controllers, which move the optic. The pendulum suspension filters this noise by $(1/f)^2$, which eases the problem at higher frequencies. The typical noise in each of the OSEM drivers falls quickly between 22Hz and around 90Hz, due to 6 pole active Butterworth filters. At 90Hz, the driver noise levels off at about $30\text{nV}/\sqrt{\text{Hz}}$. The impact of 12 independent drivers, with $2\text{k}\Omega$ loads, and a current to force conversion of 0.04N/A , is shown in figure 5.6. The coil driver noise is not enough to completely explain the low frequency noise.

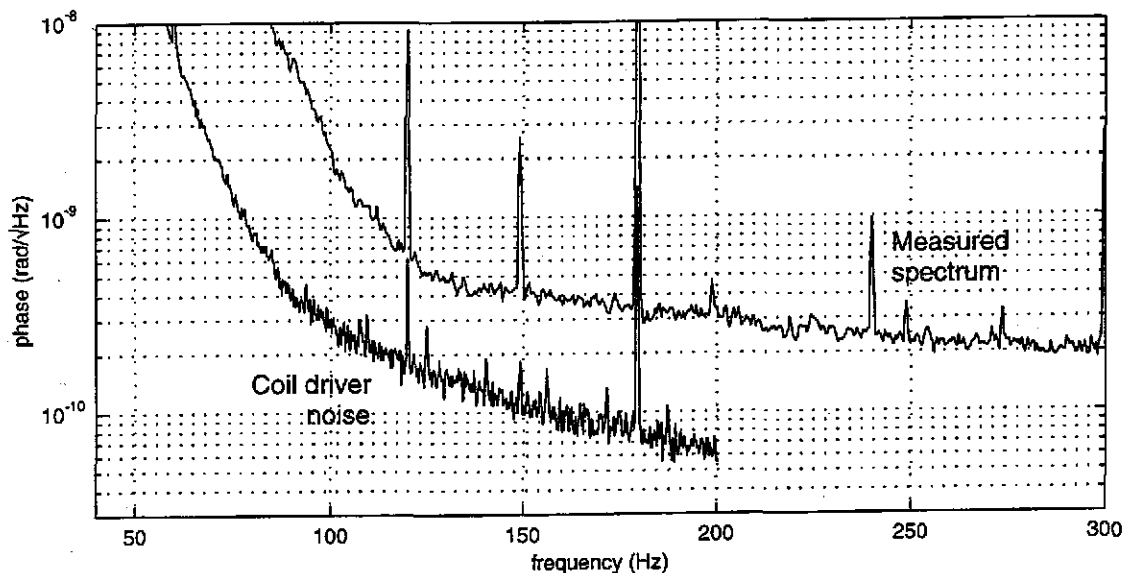


Figure 5.6: Impact of coil driver noise on the spectrum.

The coil driver noise curve is derived from the measured coil driver voltage noise, assuming 12 independent drivers. The voltage noise above 200Hz is flat (except for line spikes) so its phase noise contribution will continue to fall as f^{-2} .

There is also drive noise from the Michelson feedback controller, which drives one of the Michelson arm mirrors through a $10\text{ k}\Omega$ drive resistor. The phase contribution of the Michelson driver noise is shown in figure 5.7.

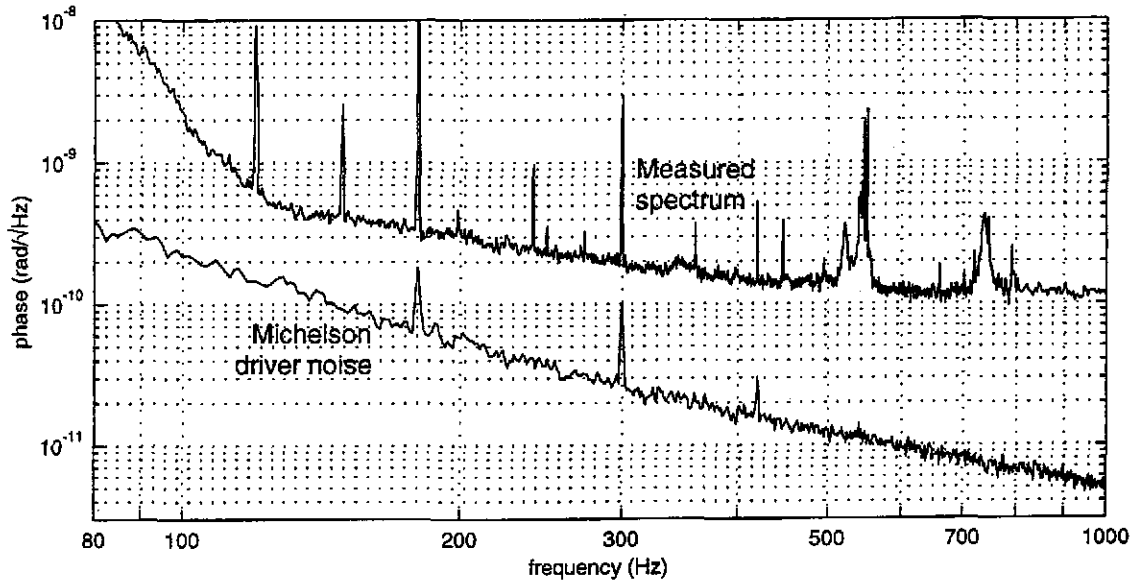


Figure 5.7: Impact of Michelson controller noise on the spectrum.

If you add the Michelson driver noise in quadrature with the OSEM driver noise, you get the total noise from the drive electronics. That sum is shown in figure 5.8. That noise is somewhat less than the measured spectrum, but not negligible.

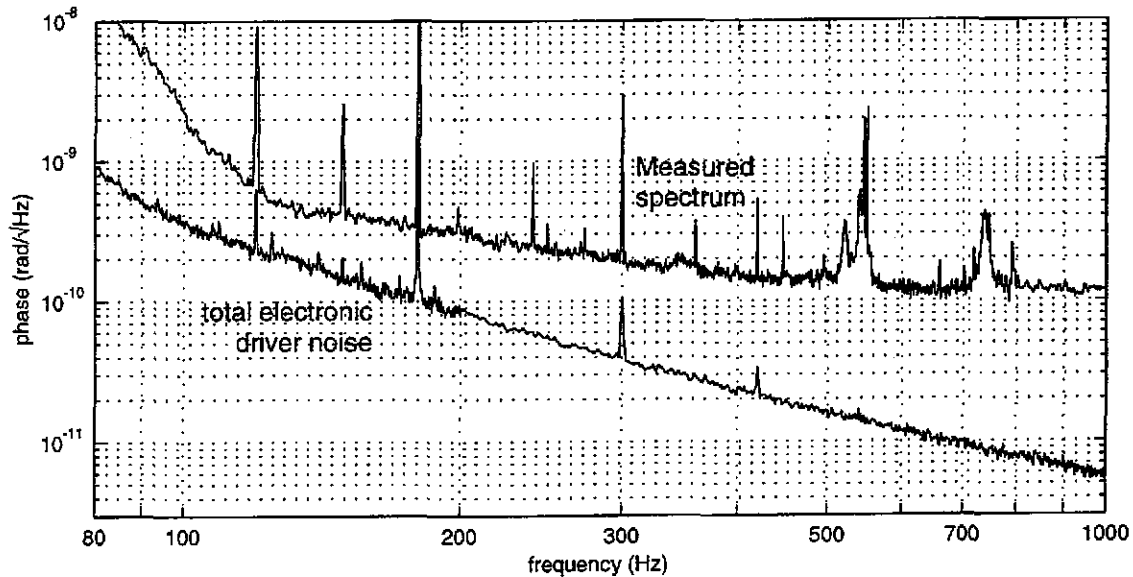


Figure 5.8: Total electronic noise.

This is the quadrature sum the Michelson driver noise and the OSEM driver noise. The OSEM driver noise from 200Hz to 1kHz was extrapolated from the noise below 200Hz assuming a f^2 rolloff due to flat voltage noise and the pendulum suspension of the mirror.

5.4.2 Thermal Noise

Internal Thermal Noise

The PNI has sufficient displacement sensitivity that thermally induced motion of the Michelson optics is a concern. The equipartition theorem states that there will be $\frac{1}{2}k_B T$ of energy per vibrational degree of freedom in the optic [see, for example, Reif '65], and the fluctuation - dissipation theorem [Callen '52] describes how the losses of the system affect the frequency distribution of that vibrational energy. To minimize the random motion of LIGO's interferometer optics in the instrument's measurement band, the Q of the internal vibrational modes optics will be in the millions, accumulating more of the vibrational energy at the resonant frequency, and thereby decreasing the off-resonance thermal motion. In an object with a reasonable Q factor which is structurally damped (unlike the viscous damping described by a dash-pot, for example) the motion of a point mass m on a spring with a resonant frequency ω_0 can be described [Saulson '90] as

$$\bar{x}^2(f) = \frac{4k_B T}{\omega m} \frac{\omega_0^2 / Q}{(\omega_0^2 - \omega^2)^2 + \omega_0^4 / Q^2}, \quad (5.9)$$

where Q is the mechanical quality factor of the oscillator, k_B is the Boltzmann constant, and T is the temperature of the oscillator's heat bath.

To properly apply this model to the motion of a mirror as seen by a laser beam, the finite size and shape of the optic and the laser spot must be considered. One way to do this is by summing over the various vibrational normal modes of the optic, weighing each of the vibrational modes by the average interaction of the moving surface with the laser spot intensity distribution [Gillespie '95]. A computer program by A. Gillespie to calculate the modal decomposition for a 3 inch diameter, 1 inch thick optic, summed over the first 60 relevant vibrational modes, yielded an weighted mirror surface motion below the first resonance (27.8 kHz) of

$$\bar{x}(f) = 4.6 \times 10^{-18} \left(\frac{4000}{Q} \right)^{\frac{1}{2}} \left(\frac{100}{f} \right)^{\frac{1}{2}} \frac{\text{meters}}{\sqrt{\text{Hz}}}. \quad (5.10)$$

Interestingly, the result of a simple analytical model proposed by [Levin '98] which treats the optic as a semi-infinite slab of material yields a similar result of

$$\tilde{x}(f) = 6.0 \times 10^{-18} \left(\frac{4000}{Q} \right)^{\frac{1}{2}} \left(\frac{100}{f} \right)^{\frac{1}{2}} \frac{\text{meters}}{\sqrt{\text{Hz}}} \quad (5.11)$$

An estimate of the Q of the internal modes of the optic was made by driving the coil drives of the OSEMs with white noise around the frequency of the fundamental vibrational mode of the optic at 27.8 kHz. The motion of the optic was measured with the interferometer, and the Q was measured from the width of the response curve. Several unexpected peaks arose around the frequency of the fundamental vibrational mode of the optic, which were assumed to result from the coupled vibrational modes of the various control elements glued to the optic. Since parasitic oscillators contribute to the loss primarily at their resonant frequencies, most of these resonance peaks were ignored. The Q 's measured for the Michelson optics were 3900.

Figure 5.10 shows the calculated noise level for a Michelson interferometer with 3 optics having Q 's of 3900 independently driven by thermal noise of $T = 300$. The off-resonance thermal motion does not account for the low frequency noise in the spectrum, but it is not far away.

Fin Motion

The internal modes of the optic are not the only thermally driven vibrational motions of interest to this type of instrument. The thermally driven resonance motion of the magnet-fin assemblies glued onto the optic are clearly visible in the spectrum around 4kHz. A detail of the spectrum is shown in figure 5.9. A simple model of the fin uses the aluminum spacer as a spring, the magnet and fin as a point mass, m , of 720 mg., and the mirror mass, M , to be 250 grams. Assuming the motion is thermally driven, the rms motion of the mirror surface should be

$$x_{\text{mirror}} \approx \frac{m}{M} \frac{1}{2\pi f_0} \sqrt{\frac{k_B T}{m}} \quad (5.12)$$

where f_0 is the resonant frequency. A single oscillator at room temperature should cause the mirror to move by 2.7×10^{-16} meters, or 3.2×10^{-9} radians. Assuming there are 12 independent oscillators changing the Michelson interferometer length, (4 on the back of each of 3 optics), the motion should be $\sqrt{12} \cdot 3.2 \times 10^{-9} = 1.1 \times 10^{-8}$ radians. If we sum the motion visible in the spectrum around the peak at 4060Hz (between the two vertical

lines in figure 5.9, subtracting the shot noise background), the rms motion is measured to be 7.1×10^{-9} radians, which is good, considering the simplicity of the model.

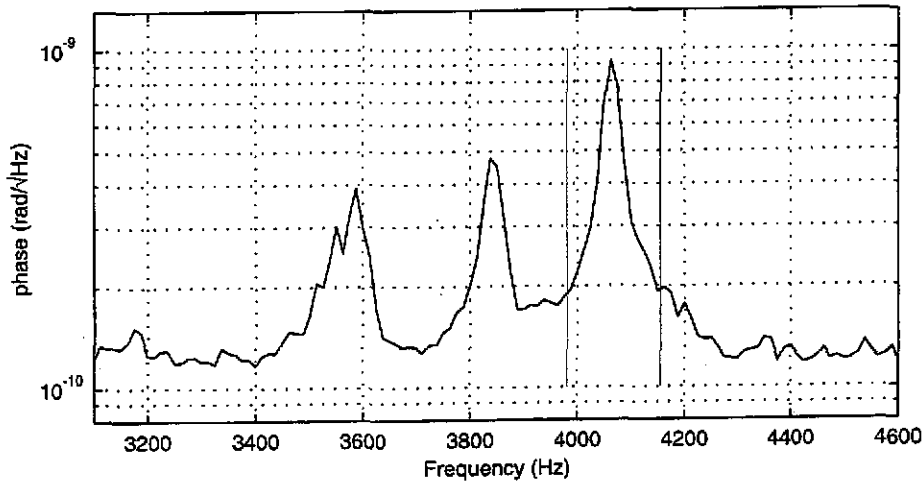


Figure 5.9: Detail of spectrum showing the 3 peaks associated with fin resonances. The two solid lines indicate the portion of the spectrum used to calculate the rms motion of the 4kHz peak.

A set of resonance curves predicting thermal noise of the type described by equation 5.9 were fitted to the data shown in figure 5.9. The fitted Q factor was about 150, and the predicted off-resonance thermal motion is shown in figure 5.10. The thermal motion predicted by the resonant measurements is below the sensitivity of the interferometer, and does not account for the low frequency noise.

Wire motion

The Michelson optics are also driven by the recoil of the violin modes of the steel wires from which the optics are suspended. Although the wire motion seen in our spectrum was predominantly driven by ground noise, the predicted thermal noise at resonance is of a similar amplitude. The thermal noise of the test mass is predicted by equation 5.9, with the mass term, m , replaced by

$$m \rightarrow \frac{1}{2} m_p \left(\frac{f_n}{f_p} \right)^2, \quad (5.13)$$

where f_p is the pendulum resonant frequency (1Hz), f_n is the n^{th} violin mode frequency ($\sim n \cdot 550\text{Hz}$), and m_p is the pendulum mass, following [Gillespie '94]. Using the FFT of a long timeseries, we determined that the Q of the first wire mode was at least 13,000.

Gonzalez and Saulson have derived the loss function of the wire assuming the loss occurs in the material of the wire [Gonzalez '94]. The Q for the n^{th} violin mode is

$$\frac{1}{Q} \approx \frac{2}{l\sqrt{t}} \sqrt{\frac{EI}{t}} \left(1 + \frac{1}{2l\sqrt{t}} \sqrt{\frac{EI}{t}} (n\pi)^2 \right) \varphi_0 \approx \frac{2}{l\sqrt{t}} \sqrt{\frac{EI}{t}} \varphi_0 \text{ for the first few modes.} \quad (5.14)$$

Here, l , E , I , t , and φ_0 are the pendulum length, Young's modulus of the wire, the area moment of inertia of the wire, the wire tension, and the loss function of the material.

| | |
|------------------------------|---|
| wire diameter | 50 microns |
| l , wire length | 30 cm |
| E , Young's Modulus | 2×10^{11} Newtons/meter ² |
| I , area moment of inertia | 3.3×10^{-19} m ⁴ |
| t , wire tension | 1.2 Newtons |

Table 5.2: Wire parameters

Using equation 5.14 and the parameters given in table 5.2, a Q of 13,000 corresponds to a loss function at 550Hz of 5×10^{-3} . This is somewhat higher than Gillespie and Raab's measurement of 5×10^{-4} for a larger diameter wire [Gillespie '93].

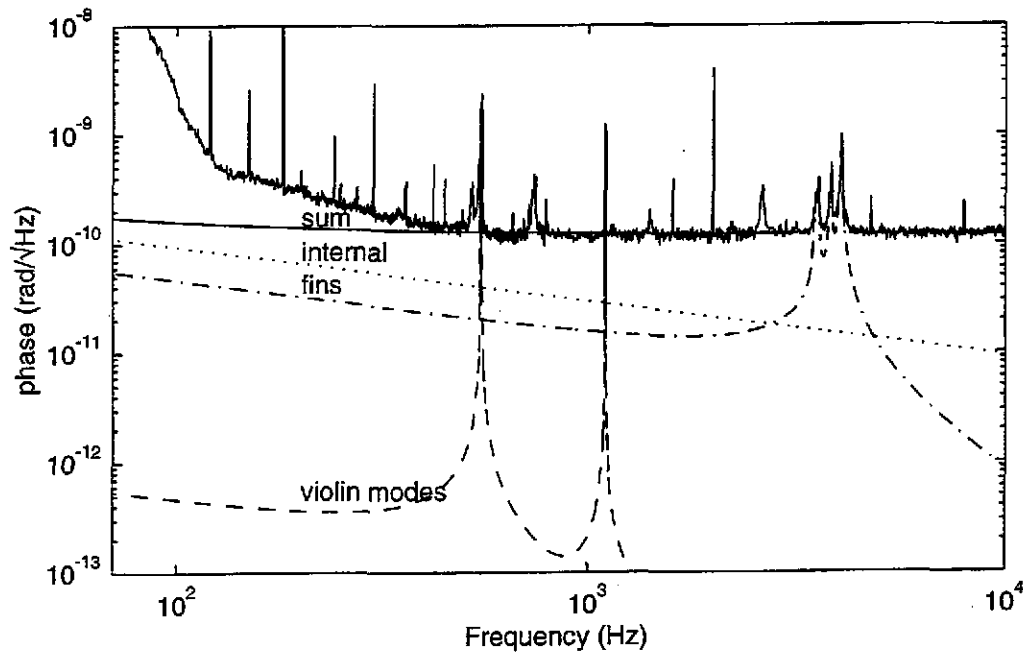


Figure 5.10: Impact of Thermal Motion on Spectrum.

The sum curve is the quadrature sum of the three sources of thermal noise shown plus the shot noise level of 1.2×10^{-10} . The low Qs measured for the optics imply that the thermal noise ought to be visible above shot noise at 100Hz, but will not impact our spectrum, as other noise sources dominate our measurement at 100Hz.

Figure 5.10 shows the impact of the off resonance thermal noise of the vibrational modes of the wires. It is clear that the off resonance thermal noise of these coupled modes does not contribute to the phase sensitivity spectrum.

Figure 5.11 shows a detail of the spectrum around the first wire resonances. Also shown is the predicted thermal noise of the wire, given the measured resonance frequencies and Q's. The predicted motion has been rebinned, to allow a reasonable comparison with the measured spectrum.

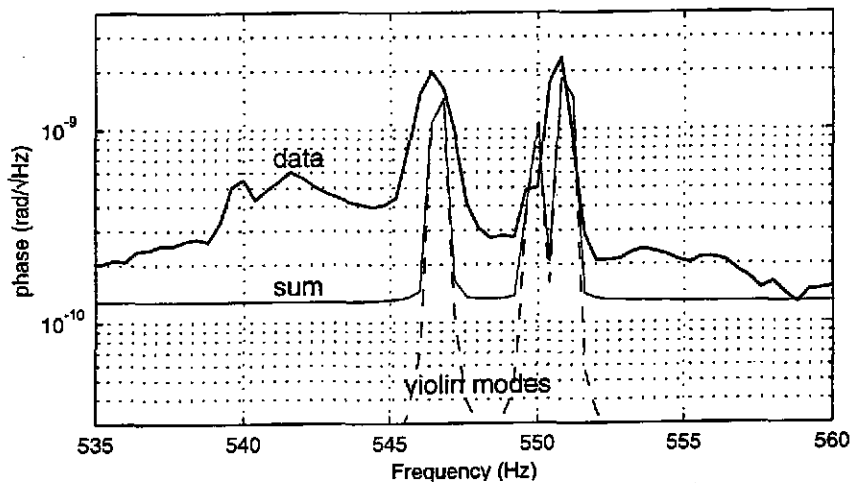


Figure 5.11: Detail of figure 5.10, showing impact of thermal motion of violin modes. The data is the same spectral data shown in all the noise curves, and the predicted thermal motion of the violin modes has been distributed into the same frequency bins as the data. The sum curve represents the sum of the predicted thermal motion and a shot noise of 1.2×10^{-10} rad/ $\sqrt{\text{Hz}}$.

We see that the predicted motion of the optic driven by the thermal noise of the wire violin modes is approximately the same as the measured motion. However, occasional increases in the amplitude of the violin mode peaks indicate that, while the baseline of these peaks is probably thermal noise, there is some coupling to ground excitation, most likely through the low frequency bounce and roll modes of the optic which stretch the wires. The off-resonant thermal motion from the suspension wires is clearly not a concern for this experiment.

5.4.3 Beam Jitter

Angular misalignments of the beams in the Michelson portion of the interferometer also contribute to the interferometer spectrum because the differential length of the paths which the beams in the Michelson arms trace is a function of the beams' direction.

For a complete treatment of misalignments, see [Saha '97]. We quote from that treatment here. In this treatment, we define the position of the beamsplitter to be the fixed reference against which all the other quantities are measured. Figure 5.12 shows the various misalignments which concern this treatment. In the perfectly aligned case, the input laser beam would propagate along the x-axis (shown as a dashed line), until it reached the beamsplitter, at which point the reflected light would go up along the y-axis to the off-axis mirror, and be retro-reflected back the beamsplitter.

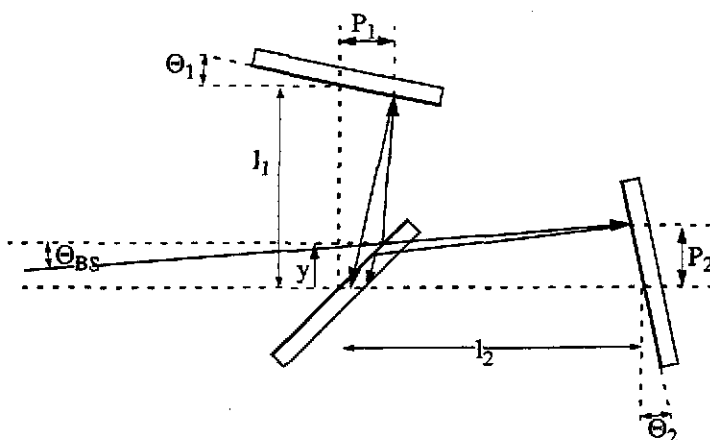


Figure 5.12: Optical lengths and misalignments in the Michelson interferometer

When the interferometer becomes misaligned, the input beam propagated in from the left, and makes an angle Θ_{BS} with the x-axis. The input beam is incident on the beamsplitter at a distance y above the x-axis. The two arm mirrors are twisted from perfect alignment by an angle Θ_1 for the off-axis mirror and Θ_2 for the on-axis mirror. Distances l_1 and l_2 are the distances from the beamsplitter to each of the respective arm mirrors, as described in chapter 2. Knowing these quantities enables one to calculate the distances P_1 and P_2 between the point where the beam hits the mirror and the x or y axis. Knowing P_1 and P_2 , we can then calculate the total path of the light and find the path length difference which is caused by misalignments.

The distance P_1 is found to be

$$P_1 = \frac{(l_1 - y) \tan \Theta_{BS} + y}{1 + \tan \Theta_{BS} \tan \Theta_1} \quad (5.15)$$

The light path from the beamsplitter to the off-axis mirror is

$$\text{path 1a} = \frac{l_1 - y - P_1 \tan \Theta_1}{\cos \Theta_{\text{BS}}} . \quad (5.16)$$

The path length from the off-axis mirror back to the x-axis is

$$\text{path 1b} = \frac{l_1 - P_1 \tan \Theta_1}{\cos(\Theta_{\text{BS}} - 2\Theta_1)} . \quad (5.17)$$

The path lengths for the on-axis mirror are the same, except that the relevant quantities are l_2, P_2 and Θ_2 , instead of l_1, P_1 and Θ_1 .

Since all the misalignments are small, it is reasonable to let $\cos \theta = 1 - \theta^2/2$ and $\tan \theta = \theta$. The path length along arm 1 is then

$$\begin{aligned} \text{path 1} &\approx 2l_1 - y + 2l_1\Theta_1^2 + l_1\Theta_{\text{BS}}^2 - 2l_1\Theta_1\Theta_{\text{BS}} - 2P_1\Theta_1, \\ \text{path 2} &\approx 2l_2 - y + 2l_2\Theta_2^2 + l_2\Theta_{\text{BS}}^2 - 2l_2\Theta_2\Theta_{\text{BS}} - 2P_2\Theta_2. \end{aligned} \quad (5.18)$$

Furthermore, it is reasonable to approximate the distances P_1 and P_2 as:

$$\begin{aligned} P_1 &\approx l_1\Theta_{\text{BS}} + y, \\ P_2 &\approx l_2\Theta_{\text{BS}} + y. \end{aligned} \quad (5.19)$$

We rewrite the arm lengths in terms of the average arm length and the asymmetry.

$$c = \frac{l_1 + l_2}{2} \quad A = \frac{l_1 - l_2}{2} . \quad (5.20)$$

We find that the change in the differential path length caused by misalignments is

$$\begin{aligned} \delta &= (\Theta_2 - \Theta_1)(2y + 2c\Theta_{\text{BS}}) \\ &\quad - 2A\Theta_{\text{BS}}(\Theta_2 + \Theta_1) \\ &\quad + 2c(\Theta_1^2 - \Theta_2^2) \\ &\quad + 2A(\Theta_1^2 + \Theta_2^2 + \Theta_{\text{in}}^2). \end{aligned} \quad (5.21)$$

The impact of misalignments on the interferometer are ameliorated by two effects. The first is the obvious point that each term in the path length fluctuation is either bilinear or quadratic in small lengths (y) or angles (Θ_1, Θ_2 , or Θ_{in}). The second mitigating factor is the recycling cavity. The recycling cavity acts as a spatial filter for the input light, so misalignments of the input beam (y and Θ_{in}), which predominantly excite the TEM_{01} and TEM_{10} modes of the cavity, appear mainly as power fluctuations. The g-factor of the

recycling cavity is 0.4, which means that angles and displacements of the input beams are reduced by approximately the recycling gain

However, the impact of misalignments can not be completely ignored. Measurements were taken to assess the impact of beam jitter on the interferometer. These measurements were taken by driving the input beam angle at 150Hz while driving the angle of the off-axis Michelson arm mirror at 40Hz. By measuring the input angles and examining the output phase noise signal at the sum and difference frequencies, one can measure the coupling from angle to phase for the products in $\Theta_{BS} \cdot \Theta_2$, and compare that coupling to the coupling we expect from equation 5.21. One then convolves the undriven spectra of differential mirror motion (as measured by the wavefront sensor) and the input beam jitter (measured with a quadrant photodiode on the input table) and calculates the predicted impact on the phase through the measured coupling constant.

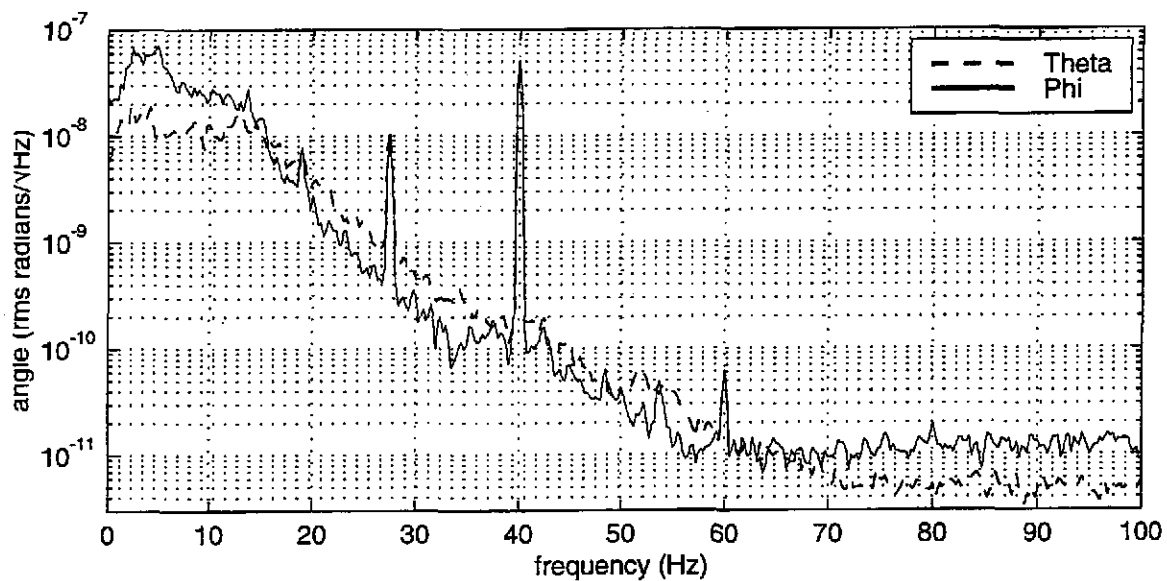


Figure 5.13: Residual differential misalignment of the Michelson arm mirrors

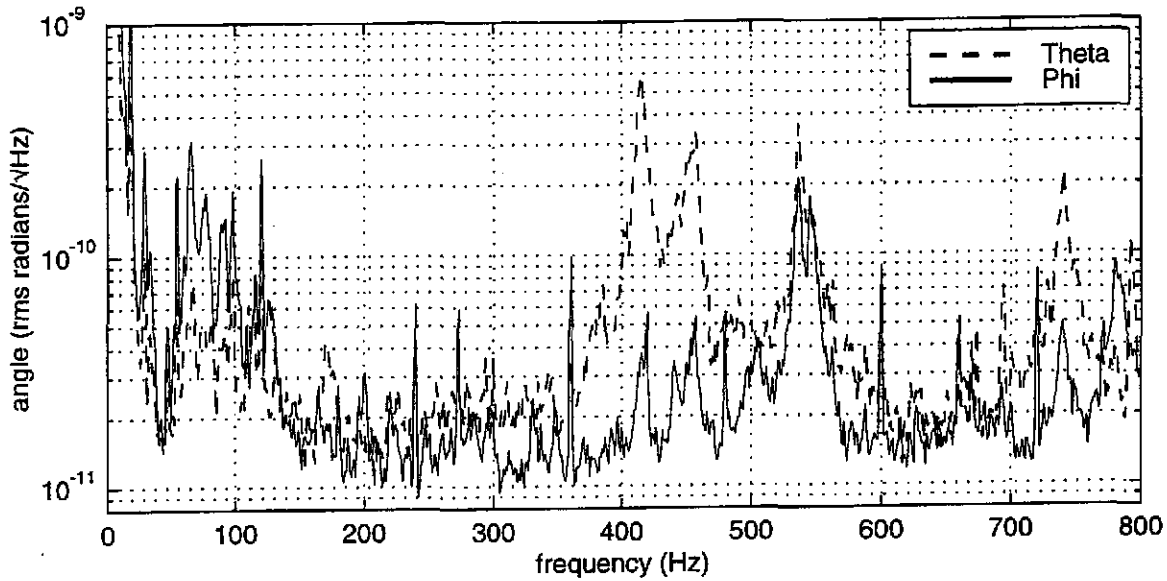


Figure 5.14: Angular motion of input beam measured on the input optics table. The peaks at 410Hz and 450Hz are introduced by a beam steering mirror in front of the quadrant photodetector, and are not present in the light incident on the interferometer.

The coupling constant between the angle product $\Theta_{BS} \cdot \Theta_2$ and the phase output is predicted by equation 5.21 to be

$$\delta\phi = \frac{2\pi}{\lambda} \Theta_2 (2\Theta_{BS} L_2 + 2y). \quad (5.22)$$

Using spatial mode decomposition calculations described by [Hefetz '97], we can relate the angle of the beam within the recycling cavity to the angle of the beam incident on the recycling mirror by comparing the relative electric field transmission of the cavity to TEM_{00} and TEM_{01} modes.

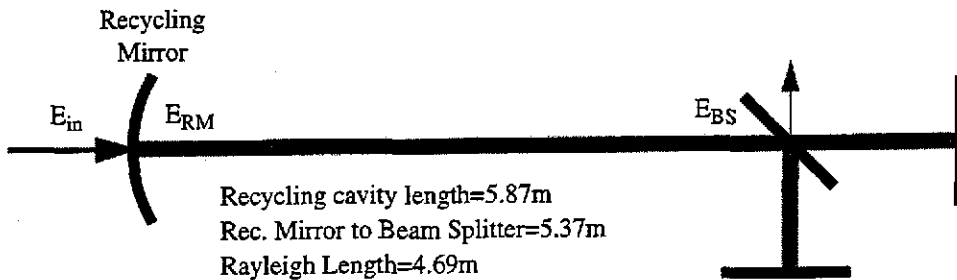


Figure 5.15: Geometry of the recycling cavity.

The electric field transmission of the recycling mirror to the TEM_{00} mode, when the cavity is locked onto that mode is

$$t_{00} = \frac{t_{\text{RM}}}{1 - r_{\text{RM}}r_{\text{MM}}} = \sqrt{\text{Recycling Gain}} \approx 19.1. \quad (5.23)$$

The transmission of the recycling mirror to the TEM_{01} mode has a similar form, except for the additional Guoy phase shift which the higher order mode experiences.

$$t_{01} = \frac{t_{\text{RM}}}{1 - r_{\text{RM}}r_{\text{MM}}e^{2i\zeta}} \quad (5.24)$$

$$|t_{01}| \approx 5.10 \times 10^{-2}.$$

Here, t_{00} and t_{01} are the field transmissions of the Fabry-Perot cavity input mirror (the recycling cavity mirror), for the TEM_{00} and TEM_{01} spatial modes when the cavity is locked. The quantities t_{RM} and r_{RM} are the field transmission and reflection of the recycling mirror alone, and r_{MM} is the field reflectivity of the "Michelson mirror." The phase shift is captured by ζ , which is

$$\zeta = \tan^{-1}\left(\frac{\text{cavity length}}{\text{Rayleigh range}}\right) = 0.897 \text{ radians}. \quad (5.25)$$

When the deviations are small, by which we mean that the displacement y_{RM} is much less than the spot size on the recycling mirror ($\omega_{\text{RM}} \approx 2\text{mm}$) and the angular deviations are much less than the normalized rotation angle for the beam at the mirror $\Theta_{\text{norm}} = \frac{\lambda}{\pi\omega(z)} \approx 1.7 \times 10^{-4}$ radians, we can treat tilts and shifts as excitations of the TEM_{01} spatial mode. The angles and shifts on the inside of the recycling mirror are reduced by the ratio of the transmission coefficients. Since the recycling cavity input mirror transmission is much smaller for the TEM_{01} than for the fundamental mode, the cavity acts as a spatial filter for the beam. For this cavity, the filter coefficient is approximately:

$$\Theta_{\text{BS}} = \Theta_{\text{RM}} = \frac{\Theta_{\text{in}}}{1.03 \cdot \text{Recycling Gain}} = 2.7 \times 10^{-3} \cdot \Theta_{\text{in}}. \quad (5.26)$$

Displacements at the beamsplitter can be related back to displacements at the recycling mirror by

$$y = \frac{y_{\text{in}}}{1.03 \cdot \text{Recycling Gain}} + 5.37\Theta_{\text{RM}} = 2.7 \times 10^{-3} \cdot y_{\text{in}} + 1.4 \times 10^{-2}\Theta_{\text{in}}. \quad (5.27)$$

If we drive the input angle with a source 4 meters from the recycling mirror, then y becomes $y = 2.5 \times 10^{-2}\Theta_{\text{drive}}$ and the measured phase is

$$\begin{aligned}\delta\phi &= \frac{2\pi}{\lambda}\Theta_2(2\Theta_{BS}l_2 + 2y) \\ &= \frac{2\pi}{\lambda} \cdot 5.7 \times 10^{-2} \cdot \Theta_2 \Theta_{drive}.\end{aligned}\tag{5.28}$$

In fact, the value measured by examining the beat note of two angular drives is $\frac{2\pi}{\lambda} \cdot 4 \times 10^{-1}$. Figure 5.16 shows the result of applying the measured coupling constant to the convolution of the angular spectra shown in figures 5.13 and 5.14. We see that the impact of beam jitter is within a factor of 2 of the low frequency noise in the spectrum between 100Hz and 200Hz.

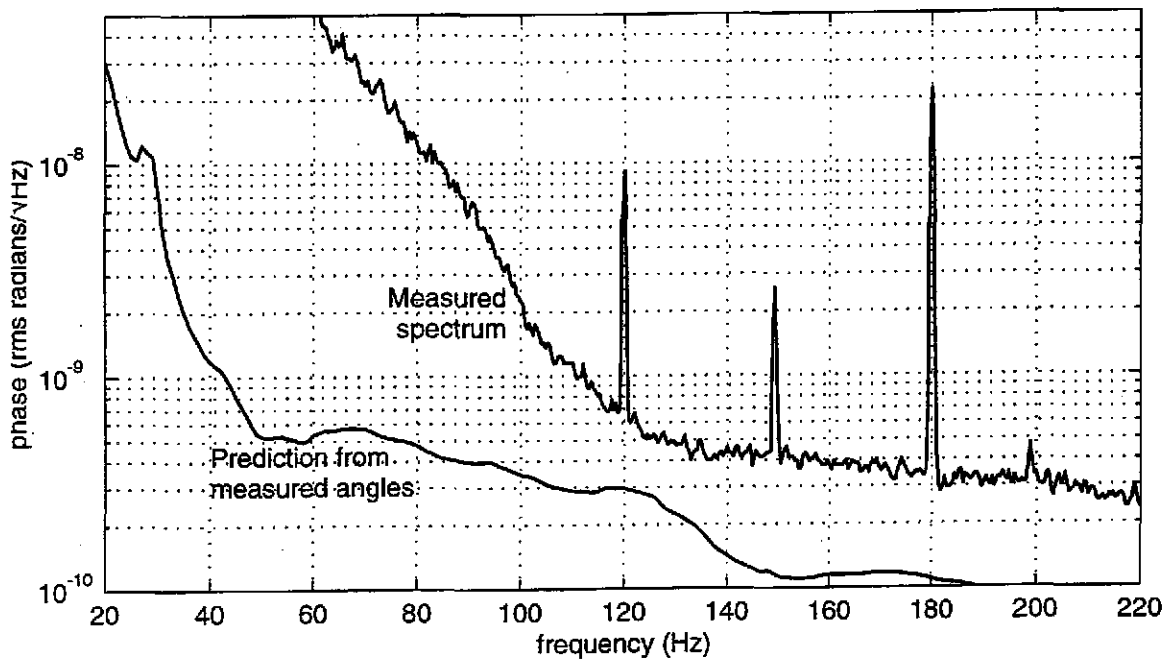


Figure 5.16: Impact of misalignments on phase noise spectrum.

In this treatment, we have ignored the impact of the misalignments on the sidebands. Although the sidebands have a smaller recycling gain than the carrier, and therefore less filtering of the higher order spatial modes, they still do not make a significant contribution. This can be seen by examining equation 2.32 which describes the power on the detector at the modulation frequency, the basis of the signal sensitivity. The signal level on the detector is proportional to $\bar{t}_0 t_+$, the product of the carrier field transmission and the sideband field transmission.

From eqn. 2.22, the carrier transmission is

$$t_0 \approx \frac{2it_{\text{RM}} \cdot 2k_0\delta \cdot e^{-ik_0(l+2c)}}{T_{\text{RM}} + L} \quad (5.29)$$

$$|t_0| \approx \frac{\sqrt{RG}}{2} (\phi_{\text{off}} + \delta\phi_{\text{carrier}}).$$

Here, $4k_0\delta$ is the phase difference of the interferometer, which is decomposed into two parts, the low frequency phase difference ϕ_{off} and the fluctuating component of the spectrum, $\delta\phi$. Equation 2.25 describes the transmission of the sidebands as

$$t_+ \approx \frac{2t_{\text{RM}} \cdot ie^{-i(k_0+k_{\text{SB}})(2c+l)} (2k_0\delta CA + SA)}{T_{\text{RM}} + L + (SA^2 + 4k_0\delta SA)} \quad (5.30)$$

$$|t_+| \approx \sqrt{RG_+} \frac{SA (1 + 2k_0\delta)}{1 + \frac{4k_0\delta SA}{T_{\text{RM}} + L + SA^2}} \quad (5.31)$$

For the values we measure for the loss and asymmetry of our cavity, $T_{\text{RM}} + L + SA^2 = 2.14 SA^2$, therefore $|t_+|$ becomes

$$\begin{aligned} |t_+| &\approx \sqrt{RG_+} SA \left(1 + \frac{2k_0\delta}{SA}\right) \left(1 - \frac{1.87k_0\delta}{SA}\right) \\ &\approx \sqrt{RG_+} SA (1 + 1.5k_0\delta) \\ &\approx \sqrt{RG_+} SA (1 + 0.38 \delta\phi_{\text{sideband}}). \end{aligned} \quad (5.32)$$

The transmission of the sidebands is almost independent of the phase fluctuations to first order because the sidebands are almost optimally coupled through the instrument.

The phase fluctuations caused by beam jitter are $\delta\phi = \frac{2\pi}{\lambda} \Theta_2 (2\Theta_{\text{BS}} l_2 + 2y)$, where Θ_{BS} and y can be related to the motion of the input beam by equations 5.26 and 5.27,

$$\Theta_{\text{BS}} = \frac{\Theta_{\text{in}}}{1.03 \cdot \text{Recycling Gain}}, \quad y = \frac{y_{\text{in}} + 5.37 \Theta_{\text{in}}}{1.03 \cdot \text{Recycling Gain}}.$$

Since the recycling cavity losses are higher for the sidebands, the recycling gain for the sidebands is a factor of 3.52 smaller than the recycling gain for the carrier. This means the spatial fluctuations on the input sidebands are not as well filtered as the fluctuations on the

carrier, and the phase fluctuations caused by input beam motion will be 3.52 times larger for the sidebands as for the carrier, i.e.

$$\delta\phi_{\text{sideband}}(\Theta_{\text{in}}, y_{\text{in}}) = 3.52 \cdot \delta\phi_{\text{carrier}}(\Theta_{\text{in}}, y_{\text{in}}). \quad (5.33)$$

We now combine the expressions for the carrier and sideband transmission, and see that the interferometer output signal is proportional to

$$\begin{aligned} |t_0 t_+| &\propto \frac{\sqrt{RG}}{2} (\phi_{\text{off}} + \delta\phi_{\text{carrier}}) \cdot \sqrt{RG_+} SA (1 + 0.38 \delta\phi_{\text{sideband}}) \\ &\approx \frac{\sqrt{RG} \sqrt{RG_+} SA}{2} (\delta\phi_{\text{carrier}} + \phi_{\text{off}} 0.38 \delta\phi_{\text{sideband}}). \end{aligned} \quad (5.34)$$

The second term in this expression is the signal due to input beam jitter which appears at the output through the spatial fluctuations of the sidebands. We show in the next section that $\phi_{\text{off}} \approx 3 \times 10^{-6}$ radians, so the component of the signal is only about $3 \times 10^{-6} \cdot 0.38 \cdot 3.52 = 4 \times 10^{-6}$ of the main signal, and can be safely ignored.

5.4.4 Input Power Fluctuations

Power fluctuations of the input laser are the classic example of bilinear coupling for interferometers operating at the dark fringe. As we saw in equation 2.33, the output signal of the interferometer is

$$P_{\text{mod}} = P_{\text{in,carrier}} \cdot RG \cdot 2 \sqrt{CSB_{\text{BS}}} \sin(2k_{\text{SB}}A) \cdot \phi, \quad (5.35)$$

where P_{mod} is the output power at the modulation frequency, RG is the recycling gain of the cavity, CSB_{BS} is the carrier to sideband ratio at the beamsplitter, k_{SB} is the wavenumber of the sideband frequency, A is the nominal asymmetry of 8cm, and ϕ is the differential phase we are trying to measure. Nominally, the phase difference ϕ is servoed to 0, so that fluctuations in the input power do not appear at the output. However, if the servo is not perfect, and the interferometer is set to a phase offset of ϕ_{off} , then input power fluctuations will couple to the output signal as

$$P_{\text{mod}} \propto \overline{P_{\text{in,carrier}}} (1 + \Delta_P) \cdot (\phi_{\text{off}} + \phi), \quad (5.36)$$

so the relative power fluctuations will be important if $\Delta_P \cdot \phi_{\text{off}}$ is comparable with ϕ . We tried to measure ϕ_{off} in two different ways. First, by measuring the rms value of the low frequency excitations (dominated by 2.5Hz and 10Hz) with the loop running, we measured the residual rms motion to be $\phi_{\text{off}} \approx 1.5 \times 10^{-6}$ radians rms.

We also measured ϕ_{off} by modulating the amplitude of the RF modulation sidebands on the light, and measuring the effect of that AM on the phase noise spectrum. One can predict this coupling by examining equation 5.35, and varying the carrier to sideband ratio. Since the modulation depth is relatively small, the sideband intensity at the input is approximately

$$P_{+/-, \text{in}} \approx P_{0, \text{in}} \frac{\Gamma^2}{4}, \quad (5.37)$$

where Γ is the modulation index. If we let $\Gamma = \Gamma_0(1 + \Delta_\Gamma)$, then we see that the interferometer output signal becomes

$$P_{\text{mod}} \propto \frac{1}{\Gamma_0} (1 - \Delta_\Gamma) \cdot (\phi_{\text{off}} + \phi). \quad (5.38)$$

If we drive the modulation strongly enough, then, at the drive frequency, the interferometer output will be $\phi_{\text{measured}} \approx \phi_{\text{off}} \cdot \Delta_\Gamma$ so that

$$\phi_{\text{off}} \approx \frac{\phi_{\text{measured}}}{\Delta_\Gamma}. \quad (5.39)$$

By applying a 1% modulation level at 990Hz, we measured the offset to be $\phi_{\text{off}} \approx 4 \times 10^{-6}$ radians, so it is reasonable to say

$$\phi_{\text{off}} \approx 3(1) \times 10^{-6} \text{ radians}. \quad (5.40)$$

To achieve a phase sensitivity of $1.2 \times 10^{-10} \text{ rad}/\sqrt{\text{Hz}}$, the measured rms offset implies that the power fluctuations need to be less than $4 \times 10^{-5}/\sqrt{\text{Hz}}$ of the average power. The power in the recycling cavity was measured by examining the 7.2ppm transmission of the Michelson arm mirrors, and found to be about a factor of 10 better. The result is shown in figure 5.17.

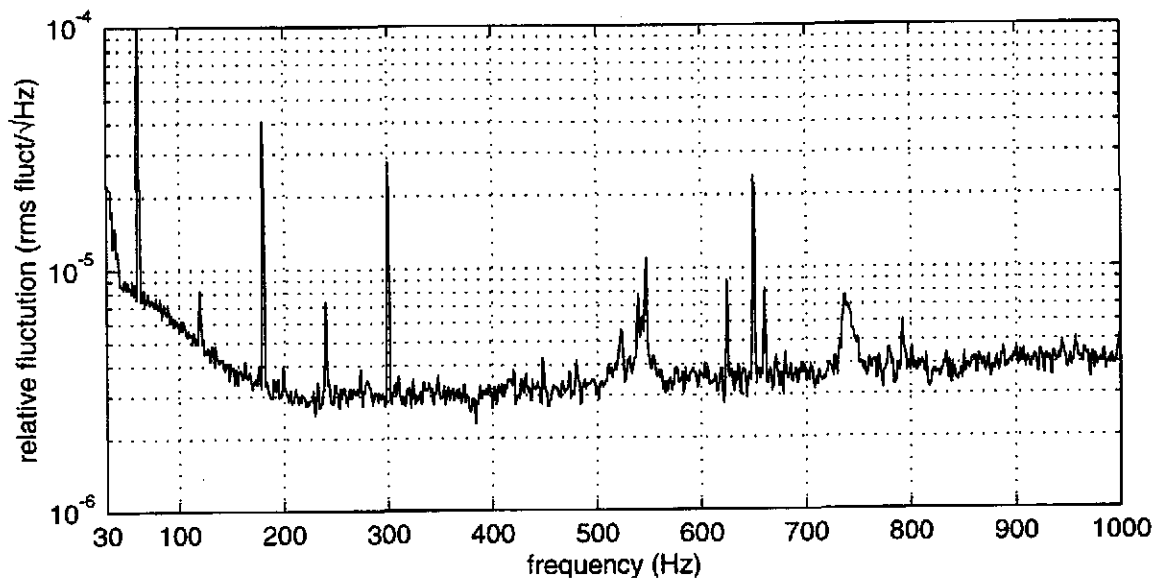


Figure 5.17: Relative fluctuations of the power in the recycling cavity

The amount of phase fluctuation resulting from this level of power variation is shown in figure 5.18. The power fluctuations measured do not impact the spectrum.

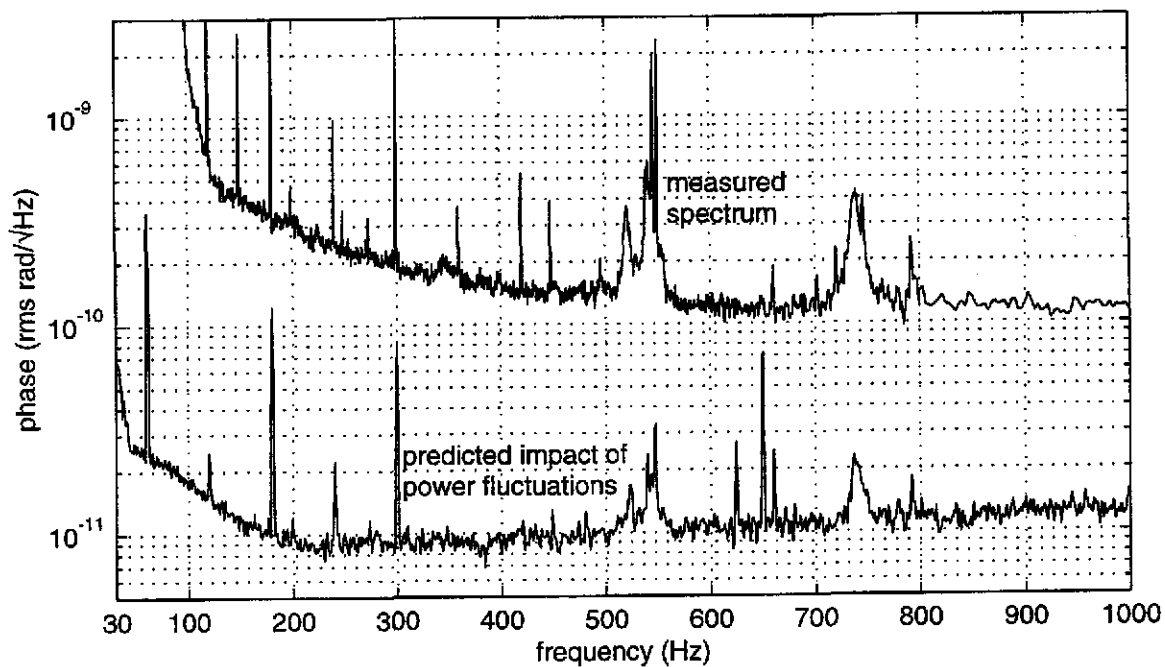


Figure 5.18: Impact of power fluctuations on phase noise spectrum.

Chapter 6

Conclusions

6.1 Improvements in Optical Phase Measurements

The precision of optical phase detection has improved dramatically during the last 30 years, buoyed by improvements in laser technology, optical materials, seismic isolation, and interferometer configuration and readout schemes. A few steps of that progress are shown below in Figure 6.1.

Figure 6.1 compares our spectrum with three other interferometric optical phase measurements. The point at the top right is the shot noise limited phase sensitivity of an experiment by Blum and Weiss in 1967 [Blum '67]. That test set limits on the interaction of optical light with microwave fields, ruling out certain theories which explain the cosmological red shift as interaction between starlight and the cosmic microwave background.

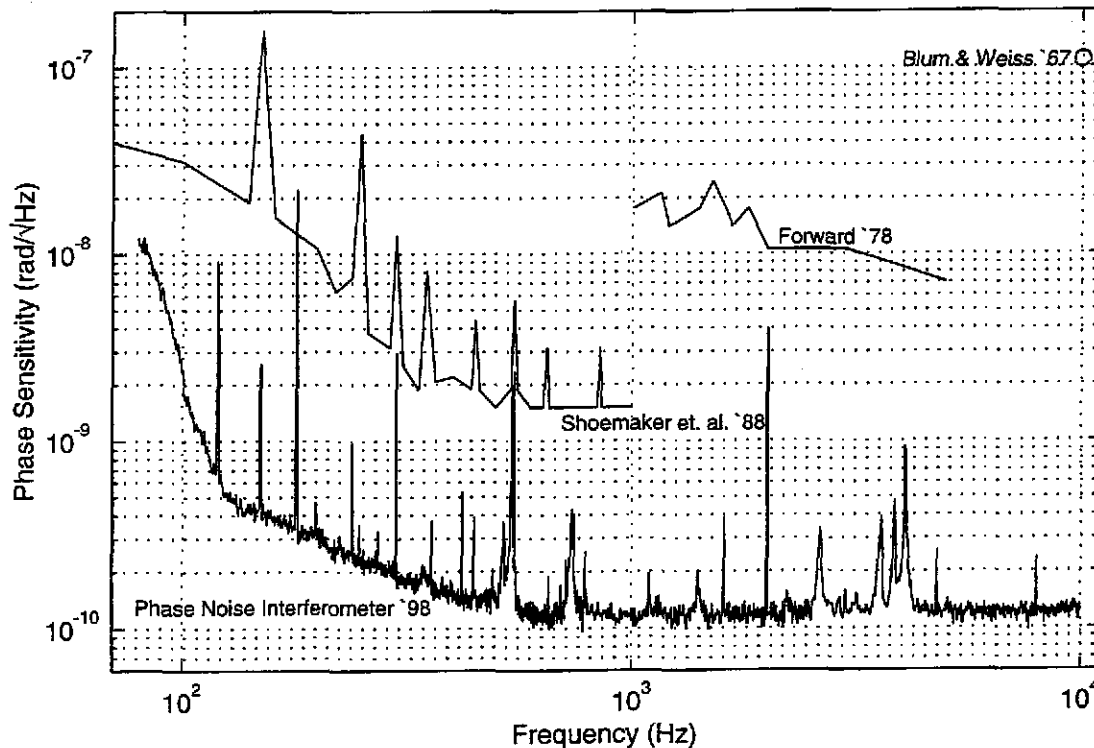


Figure 6.1: Evolution of optical phase measurements.

The data from [Blum '67], [Forward '78], and [Shoemaker '88] are rough interpolations of the data published in those papers. Although the curves above are reasonably accurate, many of the details of the spectra have not been included.

The second curve is the phase sensitivity of an early prototype gravitational wave interferometer [Forward '78] built by Robert Forward et al. in the early 1970's. That machine was a 4.25 meter Michelson interferometer with an unmodulated, balanced detection scheme. The third curve [Shoemaker '88] is taken from the results of the German gravitational wave detection effort. These results are from a 30 cm. Michelson interferometer with a RF modulation readout scheme.

Two features stand out in the comparison of these four curves. First, the overall phase detection limit is improving (thanks to more powerful lasers and power recycling). Second, the detections are moving to progressively lower frequencies, as various technical hurdles are overcome (e.g. improved readout schemes, better laser noise control, and more complete seismic isolation).

The results of this prototype are close to the final LIGO phase sensitivity requirements. Figure 6.2 shows the LIGO phase sensitivity requirement, the phase sensitivity spectrum from this experiment, and the phase sensitivity limit reached by the precursor experiment to this work. The precursor experiment was conducted in our lab with a similar interferometer, illuminated by an argon-ion laser [Saha '97], [Fritschel '98].

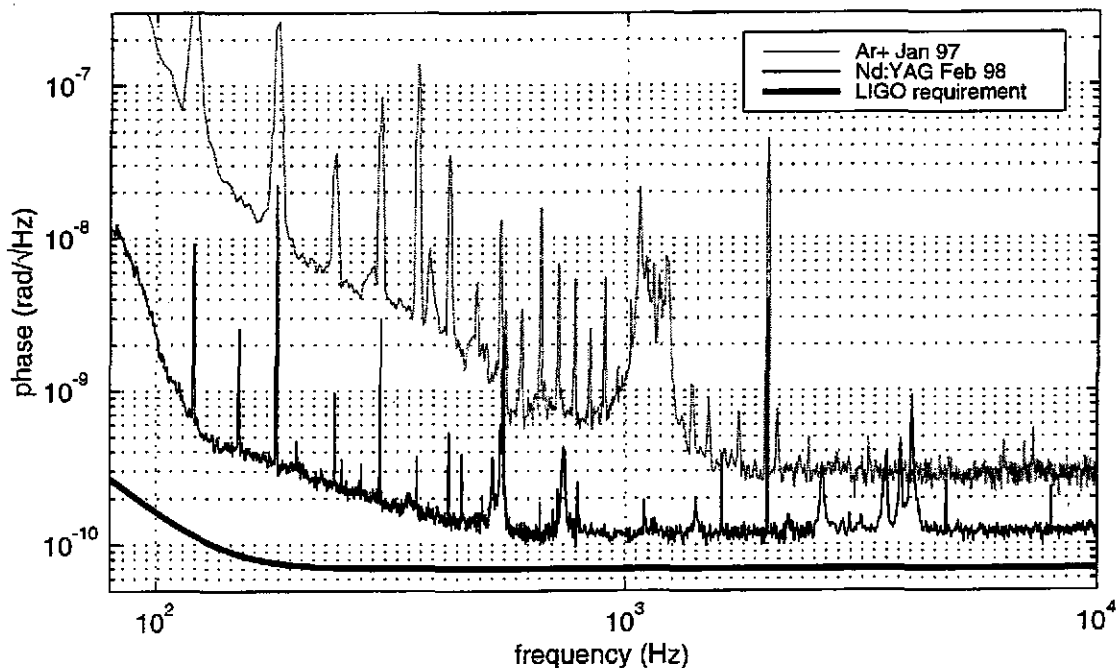


Figure 6.2: Comparison of the phase noise spectra with the LIGO requirement.

The progress made in the last two years is evident in figure 6.2. It is also evident that further progress must be made to reach the LIGO requirement.

6.2 Improvements from the Spectrum of the Argon Laser Experiment

The new spectrum is uniformly better than the results of the argon laser experiment. The shot noise limited performance has improved from $2.9 \times 10^{-10} \text{ rad}/\sqrt{\text{Hz}}$, to $1.2 \times 10^{-10} \text{ rad}/\sqrt{\text{Hz}}$. (Note that the length sensitivity has only improved slightly, since the Nd:YAG wavelength, 1.064 μm , is about twice as long as the argon wavelength, 0.514 μm .) The improvement comes primarily from the increased photon arrival rate at the beamsplitter. The most significant improvement is the improved sensitivity at the lower frequencies.

The shot noise limited regime has been extended from 1.5kHz down to 600Hz. Two major changes to the experiment were responsible for this improvement. The laser frequency noise, which was responsible for the noise of the argon laser experiment between 150Hz and 800Hz, was dramatically reduced. The noise reduction was made possible by the new laser, which had lower free-running frequency noise, and by the new frequency control scheme, which successfully reduced the laser frequency noise to an acceptable level. The control of the laser frequency noise is an important result of this work, and gives us confidence in the LIGO scheme. It is also clear that moving from the gas-plasma laser to a diode pumped laser and taking care in designing the electronics resulted in a dramatic reduction of the 60Hz line harmonics.

The large feature in the argon laser experiment spectrum between 800Hz and 1.5kHz is the thermal recoil motion of the OSEM control fins. The magnet-fin assemblies were redesigned for this work. By stiffening the aluminum standoff and reducing the weight of the fin, we raised the resonant frequencies and transformed the large structure in the old spectrum into the set of three peaks around 4kHz. These peaks should not be a problem for LIGO, since the LIGO magnet assemblies have a much higher resonant frequency (the fins will be removed entirely, leaving just the standoff and magnet), and the LIGO mirrors have 40 times the mass of our optics.

6.3 Limiting Noise for this Experiment

The sensitivity of this experiment was limited by shot noise between 600Hz and 10kHz at $1.2 \times 10^{-10} \text{ rad}/\sqrt{\text{Hz}}$. This is the best broadband optical phase sensitivity ever demonstrated. However, the shot noise limit was higher than the $7 \times 10^{-11} \text{ rad}/\sqrt{\text{Hz}}$ level

set by the LIGO science requirements document. The thermal lensing at the beamsplitter was the limiting factor for the performance of this instrument. Thermal lensing is a significant problem for LIGO, since there is approximately 10 kilowatts of power incident on the LIGO test masses. However, we have confidence that the thermal lensing can be held to an acceptable level. Although there are 10 kilowatts of power circulating in the arm cavities, only 300 watts of that power is transmitted through the optics, so the combination of high quality optical coatings and new, low bulk-absorption optical substrates will be enough to control the thermal lensing. In addition, several schemes are being considered to compensate for the thermal lensing.

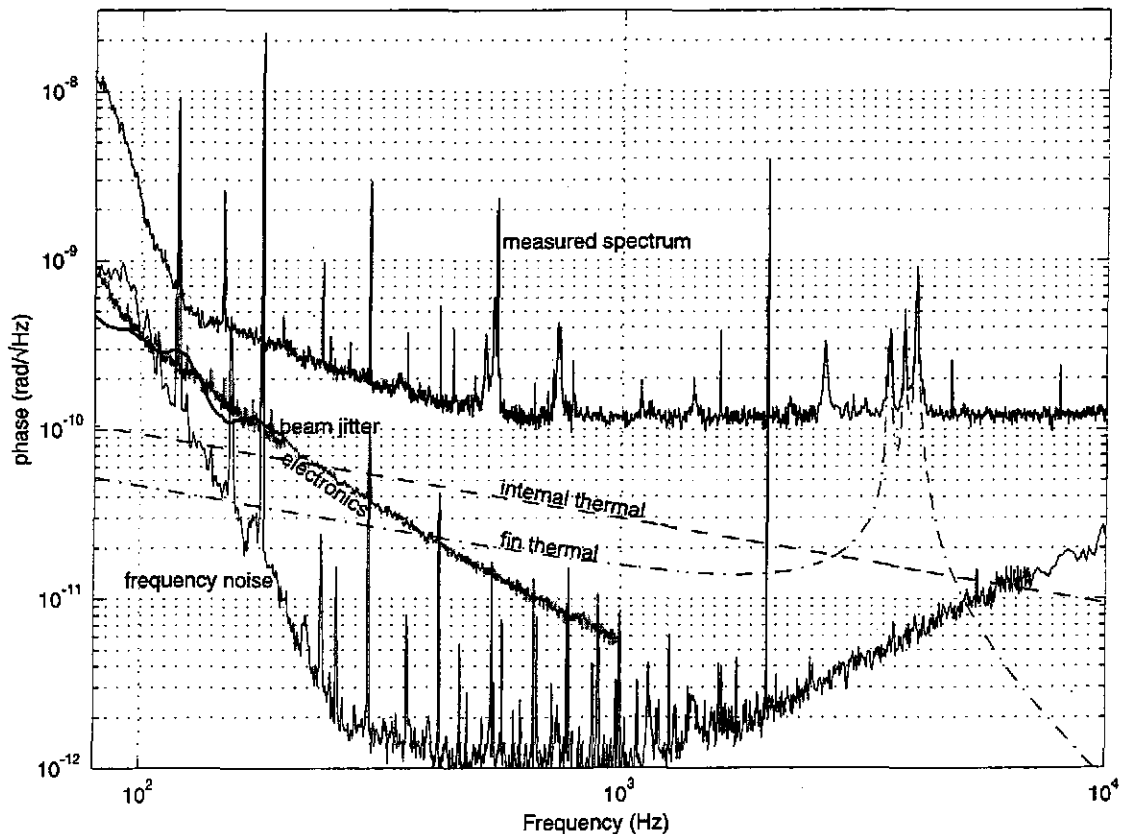


Figure 6.3: Major noise sources in the measurement.

Figure 6.3 shows the major broadband noise contributors to this experiment. (The narrow features are enumerated in section 5.3.) Above 1kHz, the broadband contributions of the various sources of noise are far enough below the shot noise level that they do not significantly impact the sensitivity limit of the instrument. However, the LIGO interferometers will be up to 30 times more sensitive to mirror motion than this experiment, due to the Fabry-Perot cavities in the Michelson arms, so the thermal noise motion of the optics seen

in this prototype will not be acceptable in the full scale instrument. This is addressed by improving the internal loss of the LIGO test masses, and decreasing the impact of the thermal recoil of the magnetic actuators, as described above.

Below 1kHz, the noise spectrum becomes more complicated. There are five broad-band noise sources which have a non-negligible impact on the spectrum. The most obvious source is shot noise, but thermal noise, laser frequency noise, electronics noise and beam jitter noise are also important. The low frequency spectra from these sources are shown in detail in Figure 6.4. The measurements of beam jitter and electronics noise above 200Hz include extrapolations of the measured data. The beam jitter curve has been extended assuming a rolloff of $(1/f)^2$.

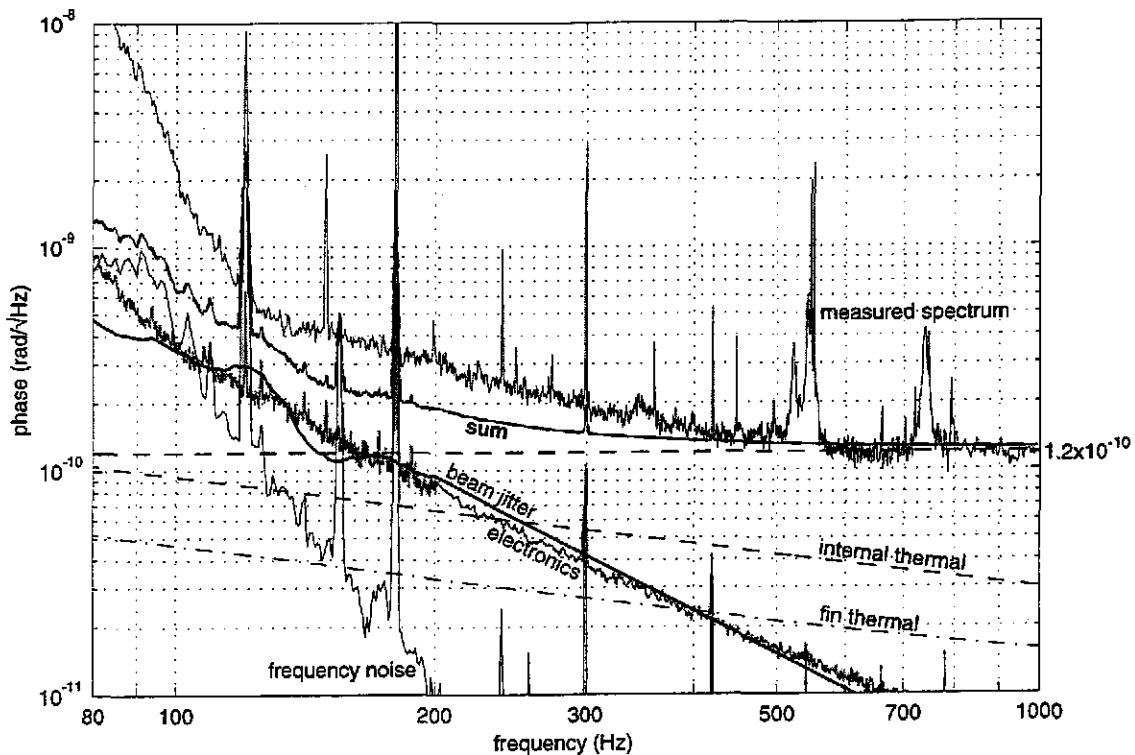


Figure 6.4: Major noise sources at low frequencies. The sum curve is the quadrature sum of the noise sources shown, including the shot noise level of 1.2×10^{-10} rad/ $\sqrt{\text{Hz}}$.

Figure 6.4 also includes the spectrum predicted by the quadrature sum of all these noise sources. The sum curve is within 50% of the measured curve everywhere above 150Hz. The residual, which is the noise which must be added in quadrature to the “sum” curve to reach the measured spectrum, is shown in figure 6.5. The close proximity of the various noise sources to one another means that all of these sources must be addressed before sig-

nificant improvements will be seen in the spectrum. It also points to a limit of one of our diagnostic techniques, which was to monitor the coherence between various noise monitors and the spectrum.

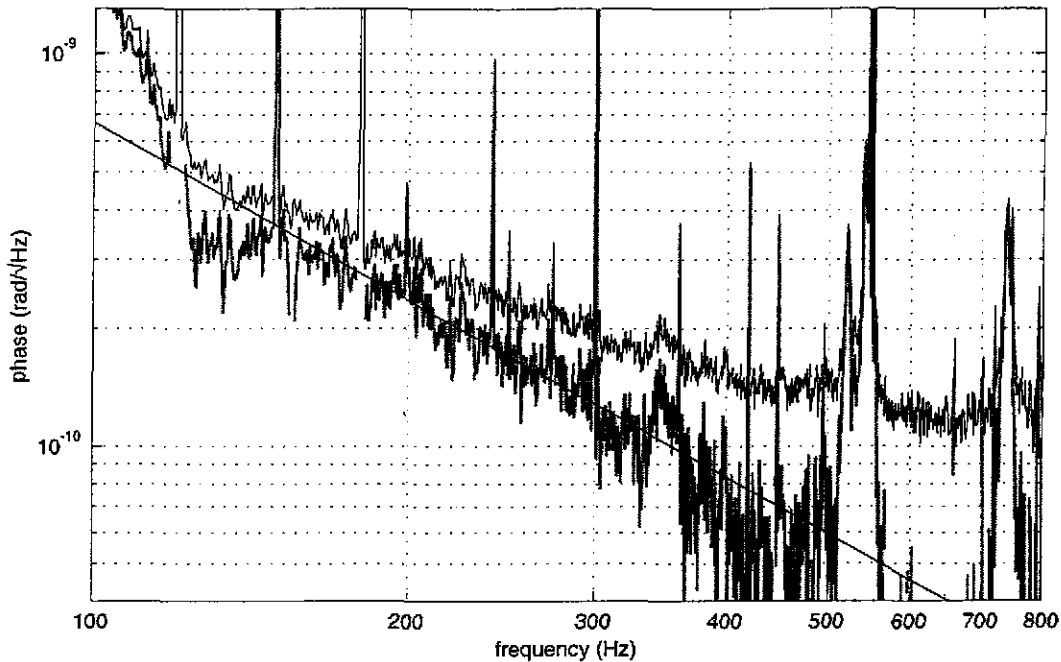


Figure 6.5: The residual phase noise in this measurement.

The grey curve is the noise which must be added in quadrature to the “sum” curve shown in figure 6.4 to reach the measured spectrum (shown here in black). The straight line is the best fit power law to the residual between 150Hz and 400Hz. The slope of the fitted line is $(1/f)^{1.5}$.

LIGO is addressing each of these noise sources shown in figure 6.4 in a different way. Improvements in the shot noise and the thermal noise were discussed above. The frequency noise at 100Hz is limited only by loop gain, as described in section 3.3.3. Tailoring the loop shape to meet LIGO requirements is a matter of good design, and should be manageable. In addition, the common-mode length of the 4 kilometer LIGO arm cavities will be used as a final stage of frequency reference, further improving the frequency control.

The beam jitter is controlled by spatially filtering the input beam with resonant cavities and by reducing the interferometer test mass motion with improved seismic isolation. Two resonant cavities are used to attenuate input beam motion. The first cavity, the pre-mode cleaner, is a small triangular mode cleaner immediately after the laser. The second cavity, the suspended mode cleaner, will be placed in the LIGO vacuum enclosure. This mode cleaner is a suspended triangular mode cleaner, which will further attenuate beam motion by rejection of higher order spatial modes. The motion of the suspended interfer-

ometer optics will be smaller, since the ground noise at the sites is much smaller than the ground motion at MIT.

Mirror motion caused by electronics noise is easy to understand, but tricky to solve. The problem for the LIGO interferometer is compounded by the increased length sensitivity of that instrument over the Phase Noise Interferometer. One way to improve the sensitivity limit is to reduce the electronics noise. This is certainly important, but as shown in section 5.4.1, the electronics noise in this work is approximately equal to the Johnson noise of the $2\text{k}\Omega$ resistors in the drive circuit for the local control of the optics, which leaves little room for improvement. The place where improvements can be made is the coupling of electronic noise into mirror motion. By reducing the final actuator authority, it is simple to reduce the mirror motion caused by electronic noise. This can be done by using smaller magnets, larger test masses, or lower pendulum frequencies. However, this option has the obvious disadvantage of reduced interferometer control. This area remains a topic of active interest. There is currently particular interest in interferometer lock acquisition, which typically requires greater bandwidth and dynamic range than normal operation; improved seismic isolation, both active and passive, to reduce the necessary actuator authority; and control reallocation techniques, which employ cascaded actuators permitting the noise of high dynamic range controllers to be attenuated by various intermediate stages.

6.4 Concluding Remarks

We have operated a system with a phase detection scheme which is similar to the LIGO interferometer, and used it to set a new record for broad-band optical phase sensitivity. Furthermore, we believe this experiment shows that the LIGO requirements can be met.

The phase sensitivity limit we reached is shot noise limited between 600Hz and 10kHz, at a level of $1.2 \times 10^{-10} \text{ rad}/\sqrt{\text{Hz}}$. The limit for this detection was set by thermal lensing. By using better quality optics, we believe the thermal lensing of LIGO can be controlled so that the requirement of $7 \times 10^{-11} \text{ rad}/\sqrt{\text{Hz}}$ can be achieved. The phase sensing limit between 150Hz and 600Hz was set by a variety of sources, including beam jitter, frequency noise, and length changes induced by electronics noise in the mirror drives.

Each of these sources is well understood, and is being considered in the design of the LIGO interferometers so that they will not compromise the results of that instrument. Additional noise sources, such as parasitic interferometry from scattered light, were finally eliminated from our spectrum entirely.

References

- [Abramovici '92] A. Abramovici, W. E. Althouse, R. W. P. Drever, Y. Gürsel, S. Kawamura, F. J. Raab, D. Shoemaker, L. Sievers, R. E. Spiro, K. S. Thorne, R. E. Vogt, R. Weiss, S. E. Whitcomb, and M. E. Zucker, "LIGO-The Laser Interferometer Gravitational-wave Observatory," *Science*, **256**, (1992) pp. 325-333.
- [Anderson '84] D.Z. Anderson, "Alignment of Resonant Optical Cavities," *Appl. Opt.*, **23**, (1984) pp. 2944-2949.
- [Andersson '98] N. Andersson, K. Kokkotas, N. Stergioulas, "On the relevance of the r-mode instability for accreting neutron stars and white dwarfs," in preparation, available at the LANL server¹, astro-ph/9806089.
- [Barish '97] Barry Barish, "LIGO: Status and Prospects," *Proc. of Conference on Gravitational Wave Detection, Tokyo*, eds. K. Tsubono, M. K. Fujimoto, K. Kuroda, Universal Academy Press Inc., Tokyo (1997) pp. 163-173.
- [Bethe '98] H. Bethe and G. E. Brown, "Contribution of high-mass black holes to mergers of compact binaries," in preparation, available at the LANL server¹, astro-ph/9805355.
- [Bildsten '98] Lars Bildsten, "Gravitational Radiation and Rotation of Accreting Neutron Stars," *Astrophysical Journal*, **501**, (1998), pp. L89-L93
- [Blair '97] D.G. Blair, M. Notcutt, L. Ju, M. Tobar, Y.M. Yang, E. Wang, C. Taylor, J. Winterflood, J.F. Liu, M. Taniwaki, C.N. Zhao, D.E. McClelland, C.C. Harb, M.B. Gray, E.H. Huntington, T.C. Ralph, H.-A. Bachor, R.J. Sandeman, D. Mudge, D. Ottaway, M.W. Hamilton, J. Munch, and P.J. Veitch, "Progress in the development of technology for advanced LIGW detectors," in **Gravitational Wave Detection**, K. Tsubono, M.-K. Fujimoto and K. Kuroda, Universal Academic Press Inc., 75 (1997).
- [Blum '67] Gerald Blum and Rainer Weiss, "Experimental Test of the Freundlick Red-Shift Hypothesis," *Physical Review*, **155**, (1967) pp.1412-1413.
- [Caves '80] Carlton Caves, "Quantum-Mechanical Radiation-Pressure Fluctuation in an Interferometer," *Phys. Rev. Letters*, **45**, (1980) pp. 75-79.
- [Caves '81] Carlton Caves, "Quantum-mechanical noise in an interferometer," *Phys. Rev. D*, **23**, (1981) pp. 1693-1708.
- [Csatorday '98] P. Csatorday, A. Marin, P. Fritschel, M. Zucker, "Photodiodes for Initial LIGO," presented at The Second Eastern Gravity Meeting, March 1998, LIGO document G980048-00-R.
- [Drever '82] R. W. P. Drever, "Interferometric detectors of gravitational radiation," in *Gravitational Radiation*, ed. by N. Deruelle and T. Piran, North-Holland Publishing Co. 1983, pp. 321-338.

1. <http://xxx.lanl.gov/abs/astro-ph>

- [Drever '83] R. W. P. Drever, J. L. Hall, F. V. Kowalski, J. Hough, G. M. Ford, A. J. Munley, and H. Ward, "Laser Phase and Frequency Stabilization Using an Optical Resonator," *Appl. Phys. B*, **31**, (1983) pp. 97-105.
- [Einstein '16] A. Einstein, "Naherungsweise Integration der Feldgleichungen der Gravitation," *Sitzungsberichte der Koniglich Preussischen Akademie der Wissenschaften, Sitzung der physikalisch-mathematischen Klasse*, (1916) pp. 688.
- [Einstein '18] A. Einstein, "Uber Gravitationswellen," *Sitzungsberichte der Koniglich Preussischen Akademie der Wissenschaften, Sitzung der physikalisch-mathematischen Klasse*, (1918) pp. 154.
- [Fritschel '92] Peter Fritschel, "Techniques for Laser Interferometer Gravitational Wave Detectors", Ph.D. Thesis, Massachusetts Institute of Technology, 1992.
- [Fritschel '98] P. Fritschel, G. Gonzalez, B. Lantz, P. Saha, and M. Zucker, "High power interferometric phase measurement limited by quantum noise and application to detection of gravitational waves," *Phys. Rev. Letters*, **80**, (1998) pp. 3181-3184.
- [Folker '98] *Laser Interferometer Space Observatory*, editor William M. Folker, AIP Conference Proceedings 456, July 1998.
- [Forward '78] Robert Forward, "Wideband laser-interferometer gravitational-radiation experiment," *Phys. Rev. D*, **17**, (1978) pp. 379-390.
- [Hefetz '97] Yaron Hefetz, Nergis Mavalvala, and Daniel Sigg, "Principles of calculating alignment signals in complex resonant optical interferometers," *J. Opt. Soc. Am. B*, **14**, (1997) pp. 1597-1605.
- [Giaime '95] Joseph Giaime, "Studies of Laser Interferometer Design and a Vibration Isolation System for Interferometric Gravitational Wave Detectors," Ph. D. Thesis, Massachusetts Institute of Technology (1995).
- [Giaime '96] J. Giaime, P. Saha, D. Shoemaker, and L. Sievers, "A passive vibration isolation stack for LIGO: Design, modeling, and testing," *Rev. Sci. Instrum.*, **67**, (1996) pp. 208-214.
- [Gillespie '93] A. Gillespie and F. Raab, "Thermal noise in the test mass suspensions of a laser interferometer gravitational-wave detector prototype," *Phys. Lett. A*, **179**, (1993) pp. 357-363.
- [Gillespie '94] A. Gillespie and F. Raab, "Suspension losses in the pendula of laser interferometer gravitational-wave detectors," *Phys. Lett. A*, **190**, (1994) pp. 213-220.
- [Gillespie I '95] A. Gillespie and F. Raab, "Thermally excited vibrations of the mirrors of laser interferometer gravitational-wave detectors," *Phys. Rev. D*, **52**, (1995) pp. 577-585.
- [Gillespie II '95] Aaron D. Gillespie, "Thermal Noise in the Initial LIGO Interferometers," Ph. D. Thesis, California Institute of Technology (1995).
- [Gonzalez '94] G. Gonzalez and P. Saulson, "Brownian-motion of a mass suspended by an anelastic wire," *J. Acoust. Soc. Am.*, **96**, (1994) pp. 207-212.

- [Gonzalez '97] Gabriela Gonzalez, "Shot Noise in the Ar PNI," 1997, LIGO document which develops the phase sensitivity of the Schnupp modulated, recycled Michelson.
- [Hello '93] P. Hello and J. Y. Vinet, "Simulation of thermal effects in interferometric gravitation-wave detectors," *Phys. Lett. A*, **178**, (1993) pp. 351-356.
- [Hello '98] P. Hello, "Optical aspects of interferometric gravitational-wave detectors," in *Progress in Optics*, Vol. 38, ed. by E. Wolf, Elsevier Science B. V., (1998) pp. 85-164.
- [Hough '97] Jim Hough et al, "GEO 600: Current Status and some aspects of the design," *Proc. of Conference on Gravitational Wave Detection, Tokyo*, eds. K. Tsubono, M. K. Fujimoto, K. Kuroda, Universal Academy Press Inc., Tokyo (1997) pp.175-182.
- [Hulse '75] R. Hulse and J. Taylor, "Discovery of a pulsar in a binary system," *Astrophysical Journal*, **195**, (1975) L51-L53.
- [Levin '98] Yu. Levin, "Internal thermal noise in the LIGO test masses: A direct approach," *Phys. Rev. D*, **57**, (1998) pp. 659-663.
- [LIGO SRD '95] *LIGO Science Requirements Document*, Specification LIGO-E950018 (LIGO Project, California Institute of Technology and Massachusetts Institute of Technology, 1995).
- [Loudon '83] Rodney Loudon, *The Quantum Theory of Light, 2nd Edition*, Oxford Science Publications, (1983).
- [Mavalvala '97] Nergis Mavalvala, "Alignment Issues in Laser Interferometric Gravitational-Wave Detectors," Ph. D. Thesis, Massachusetts Institute of Technology, 1997.
- [Michelson 1887] Albert Michelson and Edward Morley, "On the Relative Motion of the Earth and the Luminiferous Ether," *American Journal of Science*, **34**, (1887) pp. 333-345.
- [Morrison I '94] E. Morrison, B.J. Meers, D. I. Robertson, and H. Ward, "Experimental Demonstration of an Automatic Alignment System for Optical Cavities," *Appl. Opt.*, **33**, (1994) pp. 5037-5040.
- [Morrison II '94] E. Morrison, B. J. Meers, D. I. Robertson, and H. Ward, "Automatic alignment of optical interferometers," *Appl. Opt.*, **33**, (1994) pp. 5041-5049.
- [Narayan '91] R. Narayan, T. Piran, and A. Shemi, "Neutron-star and black-hole binaries in the galaxy," *Astrophysics Journal*, **379**, (1991) L17-L20.
- [Niebauer '91] T. M. Niebauer, R. Schilling, K. Danzmann, A. Rüdiger, W. Winkler, "Nonstationary shot noise and its effect on the sensitivity of interferometers," *Phys. Rev. A*, **43**, (1991) pp. 5022-5029.
- [Oliver '72] F. W. J. Oliver, "Bessel Functions of Integral Order" chapter 9 of *Handbook of Mathematical Functions* (ed. Milton Abramowitz and Irene Stegun), Dover Publications, 1972.

- [Owen '98] B. Owen, L. Lindblom, C. Cutler, B. Schutz, A. Vecchio, and N. Andersson, "Gravitational Waves from Hot Young Rapidly Rotating Neutron Stars," submitted to *Phys. Rev. D*.
- [Phinney '91] E. S. Phinney, "The rate of neutron-star binary mergers in the universe - Minimal predictions for gravity-wave detectors," *Astrophysical Journal*, **380** (1991) L17-L21.
- [Regehr I '95] M. Regehr, F. J. Raab, and S. E. Whitcomb, "Demonstration of a power-recycled Michelson interferometer with Fabry-Perot arms by frontal modulation," *Optics Letters*, **20**, (1995) pp. 1507-1509.
- [Regehr II '95] Martin Regehr, "Signal Extraction and Control for an Interferometric Gravitational Wave Detector," Ph. D. Thesis, California Institute of Technology (1995). Contains a good description of the largely unpublished history of Schnupp modulation.
- [Reif '65] F. Reif, *Fundamentals of Statistical and Thermal Physics*, McGraw-Hill, Inc. 1965.
- [Saha '97] Partha Saha, "Noise Analysis of a Suspended High Power Michelson Interferometer," Ph. D. Thesis, Massachusetts Institute of Technology, (1997).
- [Sakurai '85] J. J. Sakurai, *Modern Quantum Mechanics*, Addison-Wesley Publishing Company, 1985.
- [Sampas '90] N. Sampas and D. Z. Anderson, "Stabilization of laser beam alignment to an optical resonator by heterodyne detection of off-axis modes," *Appl. Opt.*, **29**, (1990) pp. 394-403.
- [Saulson '90] Peter Saulson, "Thermal noise in mechanical experiments," *Phys. Rev. D*, **42**, (1990) pp. 2437-2445.
- [Saulson '94] Peter Saulson, *Fundamentals of Interferometric Gravitational Wave Detectors*, World Scientific, 1994.
- [Schnupp '86] L. Schnupp, 1986 (unpublished) Private Communication.
- [Schnupp '89] L. Schnupp, 1989, private communication. Gives a time domain description of the noise resulting from modulation.
- [Schutz '90] Bernard Schutz, *A First Course in General Relativity*, Cambridge University Press, 1990.
- [Shoemaker '88] D. Shoemaker, R. Schilling, L. Schnupp, W. Winkler, K. Maischberger, and A. Rüdiger, "Noise behavior of the Garching 30-meter prototype gravitational-wave detector," *Phys. Rev. D*, **38**, (1988) pp. 423-432.
- [Siegman '86] A. E. Siegman, *Lasers*, University Science Books, 1986.
- [Strain '94] K. A. Strain, K. Danzmann, J. Mizuno, P. G. Nelson, A. Rüdiger, R. Schilling, W. Winkler, "Thermal lensing in recycling interferometric gravitational wave detectors," *Phys. Lett. A*, **194**, (1994) pp. 124-132.

- [Taylor '84] J. Taylor and J. Weisberg, "Observations of post-newtonian timing effects in the binary pulsar PSR1913+16," *Phys. Rev. Letters*, **52**, (1984) pp. 1348-1350.
- [Taylor '89] J. Taylor and J. Weisberg, "Further experimental tests of relativistic gravity using the binary pulsar PSR 1913+16," *Astrophysical Journal*, **345**, (1989) pp. 434-450.
- [Thorne '89] Kip Thorne, "Light scattering and Proposed Baffle Configuration for the LIGO," January 1989, internal LIGO document.
- [Tsubono '97] K. Tsubono and the TAMA collaboration, "TAMA Project," *Proc. of Conference on Gravitational Wave Detection, Tokyo*, eds. K. Tsubono, M. K. Fujimoto, K. Kuroda, Universal Academy Press Inc., Tokyo (1997) pp.183-191.
- [Vinet '97] J.-Y. Vinet et al, *Proc. of Gravitation and Cosmology*, ICGC-95 Conference, Pune, India 13-19 Dec. 1995, Astrophysics and Space Library, Kluwer Academic Publishers **211**, (1997) pp. 89-93.
- [Winkler '91] W. Winkler, K. Danzmann, A. Rüdiger, and R. Schilling, "Heating by optical absorption and the performance of interferometric gravitational-wave detectors," *Phys. Rev. A*, **44**, (1991) pp. 7022-7036.
- [Yariv '91] Amnon Yariv, *Optical Electronics*, 4th ed., Saunders College Publishing, 1991.